CHEMICAL REVIEWS

pubs.acs.org/CR

Review

Theoretical Modeling of Electrochemical Proton-Coupled Electron Transfer

Robert E. Warburton, Alexander V. Soudackov, and Sharon Hammes-Schiffer*

Cite This: https://doi.org/10.1021/acs.chemrev.1c00929

Read Online

ACCESS | Metrics & More | Article Recommendations

ABSTRACT: Proton-coupled electron transfer (PCET) plays an essential role in a wide range of electrocatalytic processes. A vast array of theoretical and computational methods have been developed to study electrochemical PCET. These methods can be used to calculate redox potentials and pK_a values for molecular electrocatalysts, proton-coupled redox potentials and bond dissociation free energies for PCET at metal and semiconductor interfaces, and reorganization energies associated with electrochemical PCET. Periodic density functional theory can also be used to compute PCET activation energies and perform molecular dynamics simulations of electrochemical interfaces. Various approaches for maintaining a constant electrode potential in electronic structure calculations and modeling complex interactions in the electric double layer (EDL) have been developed. Theoretical formulations for both homogeneous and heterogeneous electrochemical PCET spanning the adiabatic, nonadiabatic, and solvent-controlled regimes have been developed and provide analytical expressions for the rate constants and current densities as functions of applied potential. The quantum mechanical treatment of the proton and inclusion of excited vibronic states have been shown to be critical for describing experimental data, such as Tafel slopes and potential-dependent kinetic isotope effects. The calculated rate constants can be used as input to microkinetic models and voltammogram simulations to elucidate complex electrocatalytic processes.

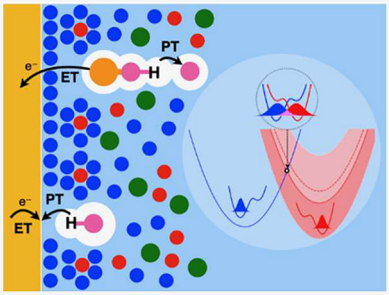

CONTENTS

Special Issue: Computational Electrochemistry

Received: November 3, 2021

1. INTRODUCTION

Proton-coupled electron transfer (PCET) is a critical step in a wide range of important electrocatalytic processes, including hydrogen oxidation and production, carbon dioxide reduction, nitrogen reduction, and oxygen reduction.[1−15] At the most basic level, PCET is defined as any process that entails the combined movement of at least one electron and one proton.[16] The electron and proton could move in the same direction or in opposite or orthogonal directions. They could transfer between distinct or identical donors and acceptors. The mechanism could be sequential, with initial electron transfer (ET) or proton transfer (PT) producing a thermodynamically stable intermediate, or concerted, without such an intermediate. In general, an electrocatalyst facilitates an electrochemical reaction that occurs at an electrode interface without being consumed. Many electrocatalytic reaction mechanisms require multiple electron and proton transfers, which could be coupled to each other and to other chemical steps.

Under this broad umbrella, electrochemical PCET denotes the subset of these reactions in which an electrode participates in ET. Electrochemical PCET can be further divided into two main categories (Figure 1). In homogeneous electrochemical PCET, the electrode serves as a reservoir for electrons but does not participate in the chemical reaction. In this case, electrons are transferred between the electrode and a redox molecule in solution, but PT occurs within the redox molecule or between the redox molecule and another molecule such as a solvent or buffer. Typically, the redox molecule does not chemisorb onto the surface but instead remains solvated at the electrode−solution interface, and the electronic coupling between the redox molecule and the electrode is relatively weak. A wide range of molecular electrocatalysts undergo homogeneous electrochemical PCET.

In heterogeneous electrochemical PCET, the electrode participates in chemical bond breaking and forming, as well as serving as a reservoir for electrons. In this case, the proton is transferred to or from the electrode surface, which is broadly defined as the combined electrode and chemisorbed species. The simplest heterogeneous electrochemical PCET reaction is proton transfer from a proton donor in solution to a metal electrode surface, also called the Volmer reaction.[17] In aqueous solution, the proton donor is typically a water molecule or hydronium ion, and in nonaqueous solution, it is usually a solvated acid. When the proton is transferred to the metal electrode, an electron is transferred from the electrode to form a metal−hydrogen bond. More complex electrocatalytic reactions involve proton transfer between a chemisorbed species and the electrode or between a chemisorbed species and a solvent molecule, a solvated species, or another chemisorbed species. Because of this complexity, heterogeneous electrochemical PCET reactions may span the strong and weak electronic coupling regimes. Furthermore, heterogeneous electrochemical PCET reactions can also occur at semiconductor interfaces.[18] In the literature, homogeneous and heterogeneous electrochemical PCET reactions are often related to outer-sphere and inner-sphere ET, respectively; however, this equivalence is not strictly held across all systems.

Given the importance and pervasiveness of electrochemical PCET, a wide range of theoretical and computational methods have been developed to study these reactions. This review will summarize the main approaches developed to study electrochemical PCET, along with illustrative examples. The first part of this review will focus on the computational methods developed to study the thermodynamics of electrochemical PCET. For homogeneous electrochemical PCET, methods have been developed to compute redox potentials and pK_a values for molecular electrocatalysts, typically using density functional theory (DFT). For heterogeneous electrochemical PCET, periodic DFT methods have been developed to compute proton-coupled redox potentials or bond dissociation free energies for removing a hydrogen atom from a surface. Various computational methods have been developed to maintain a constant potential on the electrode during these types of calculations to mimic experimental conditions. The computed proton-coupled redox potentials can be compared to experimental voltammetry measurements to benchmark theoretical calculations. These methods can be used to generate Pourbaix diagrams, which identify the most stable species as a function of pH and applied potential. Moreover, a variety of computational methods have been developed to compute the inner-sphere solute and outer-sphere solvent reorganization energies of electrochemical PCET reactions.

The next part of this review will describe the computational methods used to generate potential energy surfaces and free energy surfaces for electrochemical PCET reactions. A combination of geometry optimizations and molecular dynamics in conjunction with periodic DFT has been used to characterize the potential energy surfaces. Enhanced sampling methods such as umbrella sampling have been used to generate free energy surfaces for PCET. Analysis of these surfaces provides insight into the stable intermediates and possible reaction mechanisms for electrocatalytic reactions. The computed activation energies or free energy barriers can be

https://doi.org/10.1021/acs.chemrev.1c00929
Chem. Rev. XXXX, XXX, XXX−XXX

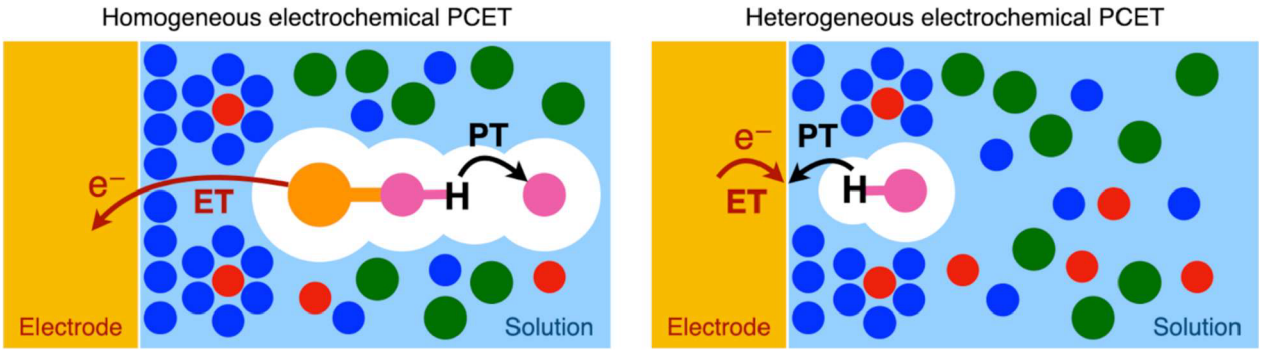

Figure 1. Schematic depictions of homogeneous (left) and heterogeneous (right) electrochemical PCET. In homogeneous electrochemical PCET, the electrode provides or accepts electrons for reduction or oxidation of the redox molecule but does not participate directly in the proton transfer reaction, which typically occurs within the redox molecule or between the redox molecule and another molecule. In heterogeneous electrochemical PCET, the electrode provides or accepts electrons and also participates directly in the chemical bond breaking and forming associated with the proton transfer reaction. The specific example shown here is proton discharge on the electrode surface (i.e., the Volmer reaction), where the proton is transferred from a proton donor to the electrode, and an electron is provided by the electrode to form a metal−hydrogen bond. Heterogeneous electrochemical PCET could also involve chemisorbed species in both the electron and proton transfer steps.

used in conjunction with transition state theory to estimate rate constants. However, such approaches assume that the reaction occurs on the ground electronic state and typically neglect hydrogen tunneling effects.

Because PCET reactions typically involve charged species, they are strongly influenced by the electrostatic potentials and electric fields at the electrode−solution interface. This review will briefly summarize the computational methods developed to model and simulate the electric double layer (EDL), which is composed of the solvent and ions at this interface. The ability to compute the electrostatic potential in the EDL is important for the calculation of rate constants for electrochemical PCET reactions. At the simplest level, multilayer dielectric continuum models have been used to describe the EDL and provide an estimate of the electrostatic potential as a function of the distance from the electrode. However, the electrostatic potentials have been shown to exhibit spatial heterogeneity in the EDL, and therefore an atomic-level description is often warranted. Simulations of the EDL with explicit solvent and ions have been performed with first-principles methods and molecular mechanical force fields. To further characterize the EDL, computational methods have been used to predict spectroscopic properties such as the vibrational frequency shifts of nitrile probes as a function of the applied electrode potential. Comparison of computational results to experimental measurements has provided detailed information about the structure and dynamics of the EDL.

This review will then focus on theoretical formulations of homogeneous electrochemical PCET that treat the transferring proton(s) quantum mechanically to include hydrogen tunneling effects. These PCET theories are related to Marcus theory for electron transfer[19−23] in that the PCET reaction occurs along a collective solvent coordinate. The description of concerted PCET in terms of electron−proton vibronic states[24−27] enables the treatment of both adiabatic and nonadiabatic mechanisms, as well as the intermediate regime. In this context, vibronically nonadiabatic refers to the regime in which the vibronic coupling is much smaller than the thermal energy. Within the vibronically nonadiabatic regime, electronically adiabatic refers to the limit in which the electrons respond instantaneously to the proton motion, whereas electronically nonadiabatic refers to the opposite limit.[16,27−29] A series of analytical vibronically nonadiabatic rate constant expressions have been derived,[26,30,31] and computational methods have been developed to compute the input quantities. These quantities include the inner-sphere solute and outer-sphere solvent reorganization energies, the proton potential energy curves and associated vibrational wave functions and energy levels, and the electronic coupling. Applications to nickel-based electrocatalysts with pendant amines for hydrogen production,[32] benzimidazole-phenol molecules designed for use in artificial photosynthetic systems,[33] and ionic liquids at gold or platinum electrodes for oxygen reduction[34] will be presented.

The next section of the review will discuss related theoretical formulations developed for heterogeneous electrochemical PCET. Many of these theories have been developed in the context of the proton discharge or Volmer reaction. Both adiabatic and nonadiabatic models, as well as approaches that interpolate between these two regimes, have been developed to describe this fundamental heterogeneous PCET reaction.[35−43] A more recently developed general theory[44] of heterogeneous electrochemical PCET in the diabatic vibronic representation inherently spans both of these limits. All of these approaches can be extended to include the solvent-controlled regime through interpolation schemes. This section will end with a brief description of the grand canonical formulation of electrochemical rate theory.[45]

The final topics covered in this review are microkinetic modeling strategies and voltammogram simulations for electrochemical PCET. Given the breadth of this review, some topics will be covered only briefly, but references to more comprehensive treatments will be provided. Moreover, only the aspects of computational electrochemistry that are directly relevant to PCET will be addressed. This review will end with a discussion of the remaining challenges and future directions in the field of theoretical and computational electrochemical PCET. Although much progress has been made, there are many unanswered questions and technical challenges to overcome.

2. THERMODYNAMICS OF ELECTROCHEMICAL PCET

This section will discuss computational methods for calculating thermodynamic properties of electrochemical PCET reactions. The first topic will be the calculation of redox potentials and pK_a values for molecular systems that participate in homogeneous electrochemical PCET reactions. The description of heteroge-

https://doi.org/10.1021/acs.chemrev.1c00929
Chem. Rev. XXXX, XXX, XXX−XXX

neous electrochemical PCET reactions requires a suitable reference, which is often chosen to be the computational hydrogen electrode. The next topic covered will be the calculation of proton-coupled redox potentials or bond dissociation free energies for heterogeneous electrochemical PCET reactions. Such calculations benefit from constant potential methods that properly describe charging effects and electric fields at the electrochemical interface. All of these methods can be combined in various ways to generate Pourbaix diagrams for PCET reactions. The last topic that will be covered in this section is the calculation of reorganization energies for PCET processes.

2.1. Calculating Redox Potentials and pK_a Values for Molecular Electrocatalysts

In molecular homogeneous catalysis, the electrode is not directly involved in bond making or breaking during redox processes. Outer-sphere PCET reactions in homogeneous electrocatalysis can occur by sequential ET and PT steps, concerted PCET steps (EPT), or a combination of sequential and concerted steps.[2,6,12,46,47] Computational studies typically consider reaction intermediates associated with the ET and PT constituents of PCET reactions to determine the thermodynamically favorable mechanism, although as described later in this review, the kinetics of these PCET processes is also very important.

The reaction free energies for ET and PT are related to the redox potentials and pK_a values, respectively, which are properties of the catalyst. The redox potential E° associated with an ET reaction is $E^\circ = -\Delta G^\circ_{red}/nF$, where ΔG°_{red} is the reaction free energy for the reduction reaction in solution, n is the number of electrons transferred, and F is the Faraday constant. The treatment of reference values for the redox potentials will be discussed below. The pK_a of an acid AH is defined as $pK_a = \Delta G^\circ_{pK_a}/[RT\ \ln(10)]$, where $\Delta G^\circ_{pK_a}$ is the reaction free energy for the removal of a proton in solution, and R and T are the ideal gas constant and temperature, respectively.

These reaction free energies can be computed through geometry optimizations and subsequent normal-mode analyses in dielectric continuum solvent using, for example, density functional theory (DFT) with the polarizable continuum model (PCM). In this case, the enthalpic, zero-point energy, entropic, and solvation free energy contributions are all computed directly in the solution phase. Historically, these free energies have been computed using Born−Haber cycles to allow for the calculation of the enthalpic, zero-point energy, and entropic contributions to the free energy in the gas phase, followed by computation of the solvation free energies for these gas phase optimized geometries.[48] However, most quantum chemistry codes enable reliable geometry optimizations and normal-mode analyses in dielectric continuum solvent. When the optimized geometries are similar in the gas phase and solution phase, these two approaches produce similar results. When these geometries differ significantly, the solvated geometry is most likely the more relevant geometry.

The absolute magnitudes of ET and PT reaction free energies are generally not expected to be quantitatively accurate using standard quantum chemistry methods.[49−53] Instead, computing relative redox potentials and pK_a values can benefit from error cancellation and enable more reliable predictions. This procedure has been discussed in terms of "isodesmic reactions" in the literature, with the general forms used to calculate redox potentials and pK_a values given in Scheme 1. Typically, the redox potential or pK_a of the reference reaction is obtained from

Scheme 1. Calculation of Redox Potentials and pK_a Values using Isodesmic Reference Reactions

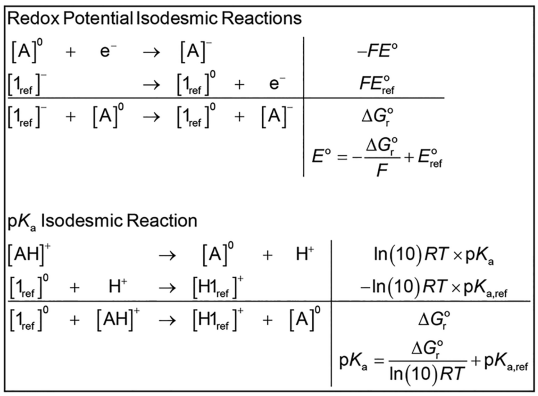

experimental data. Thus, this approach is equivalent to adding a correction to each computed redox potential or pK_a value that is the difference between the experimental value and the computed value for the reference reaction. The main advantage of this approach is that the free energy associated with the solvated electron and the reference electrode potential do not need to be computed for redox potentials, and the free energy associated with the solvated proton does not need to be computed for pK_a calculations. Another advantage is the cancellation of errors inherent to DFT and the solvation models. These types of isodesmic reactions have been used in computational studies of solution-phase hydride transfer,[52] proton transfer,[54] and PCET.[47,55−57]

2.2. Computational Hydrogen Electrode

Potential-dependent PCET reaction free energies in heterogeneous electrocatalysis commonly employ the reference reaction for H_2 oxidation through the computational hydrogen electrode (CHE) model.[58] At the standard hydrogen electrode (SHE), the rates of H_2 oxidation and H_2 evolution are equal, and the reactants and products in the following equation are in equilibrium:

$$H_2 \rightleftharpoons 2(H^+ + e^-) \tag{1}$$

In other words, the SHE corresponds to standard conditions (T = 298 K, P = 1 bar, pH = 0) when the reaction in eq 1 is at equilibrium, with an electrochemical potential equivalent to E_{SHE}:

$$\begin{aligned}\Delta G_{H_2 \rightarrow 2(H^+ + e^-)}\ [0\ \text{V vs SHE}] &= 2(\tilde{\mu}_{H^+(\text{pH }0)} + \tilde{\mu}_{e^-}) - \mu^\circ_{H_2} \\ &= 2(\tilde{\mu}_{H^+(\text{pH }0)} - eE_{SHE}) - \mu^\circ_{H_2} \\ &= 0\end{aligned} \tag{2}$$

where $\tilde{\mu}_{H^+(\text{pH }0)}$ is the electrochemical potential of a solvated proton at pH = 0, $\tilde{\mu}_{e^-} = -eE_{SHE}$ is the electrochemical potential of an electron at the SHE, and $\mu^\circ_{H_2}$ is the chemical potential of H_2 gas under standard conditions.

In this treatment, the chemical potential reference of a proton−electron pair is related to charge-neutral H_2 gas, and potential and pH effects are included *a posteriori* according to

$$\begin{aligned}\tilde{\mu}_{H^+}(\text{pH}) + \tilde{\mu}_{e^-}(E) &= \mu_{H^+ + e^-}(\text{pH}, E) \\ &= \frac{1}{2}\mu^\circ_{H_2} - k_B T\ \ln(10) \times \text{pH} - eE\end{aligned} \tag{3}$$

https://doi.org/10.1021/acs.chemrev.1c00929
Chem. Rev. XXXX, XXX, XXX−XXX

In eq 3, E is the electrode potential relative to SHE; i.e., E_{SHE} is chosen as the reference potential. Moreover, $\tilde{\mu}_{H^+}$ (pH) is the electrochemical potential of a proton at the specified pH, $\tilde{\mu}_{e^-}$ (E) is the electrochemical potential of an electron at potential E relative to SHE, and $\mu_{H^+ + e^-}$ (pH, E) is the chemical potential of a proton−electron pair at the specified pH and E. Because heterogeneous PCET reactions are often, although not always,[39,59−62] concerted, it is often convenient to combine the electrochemical potentials of the proton−electron pair, rather than evaluating them separately. The CHE model provides an efficient procedure that relates the chemical potential of H_2 gas to the electrochemical potential of a proton−electron pair. However, the CHE model does not directly account for surface charge effects on energetics or for the effect of pH on the surface structure.

Combined with calculated adsorption energies, the CHE model can be used to evaluate potential-dependent reaction thermodynamics without direct treatment of charged electrons and protons at the electrochemical interface. In particular, the thermodynamics of elementary PCET steps in a reaction mechanism can be computed using the CHE model to estimate the potential-limiting steps and reaction overpotentials. This procedure was demonstrated[58] for oxygen reduction (Figure 2A), where for potentials greater than the thermodynamic limiting potential of 0.78 V, PCET to adsorbed HO* to form solution-phase H_2O is uphill, and the oxygen reduction reaction (ORR) is thermodynamically unfavorable. Although catalytic activity depends on the kinetics of the PCET steps involved, these thermodynamic analyses have successfully described activity trends of catalysts for various electrocatalytic reactions such as hydrogen evolution,[63,64] oxygen reduction,[65−67] and CO_2 reduction.[68]

The computational electrode potential E can be determined from the work function Φ:[69]

$$\Phi = e\phi_{vac} - \varepsilon_F \quad (4)$$

Here, ϕ_{vac} is the electrostatic potential in vacuum, and ε_F is the Fermi energy, as depicted in Figure 3. The work function can be converted to an electrode potential E vs SHE by the relationship $E = (\Phi - \Phi_{SHE})/e$, where E_{SHE} is approximately −4.44 V relative to vacuum.[69,70] In calculations that use continuum solvation models, the electrostatic potential in bulk implicit solvent can be used in place of ϕ_{vac} and related to the SHE using calculated potential offsets.[71] However, E may also be determined using other valid definitions.[69,72]

The generalized CHE model enables the description of the interfacial thermodynamics as a function of pH and applied potential using the computational electrode potential.[74] For a given DFT calculation, Φ (and by proxy, E) is constant, and $\mu_{H^+ + e^-}$ depends on the pH according to the thermodynamic relation in eq 3. In this manner, the free energy is computed as a function of the applied potential and pH from a series of DFT calculations.[74,75] As an example, this relationship was used to compute potential- and pH-dependent adsorption free energies of ORR intermediates, lending theoretical insights into the ORR activity of Au(100) under alkaline conditions.[76]

2.3. Proton-Coupled Redox Potentials and Bond Dissociation Free Energies

An important property for heterogeneous electrochemical PCET reactions is the proton-coupled redox potential or bond dissociation free energy (BDFE) associated with removing an electron and a proton from a surface. In the context of

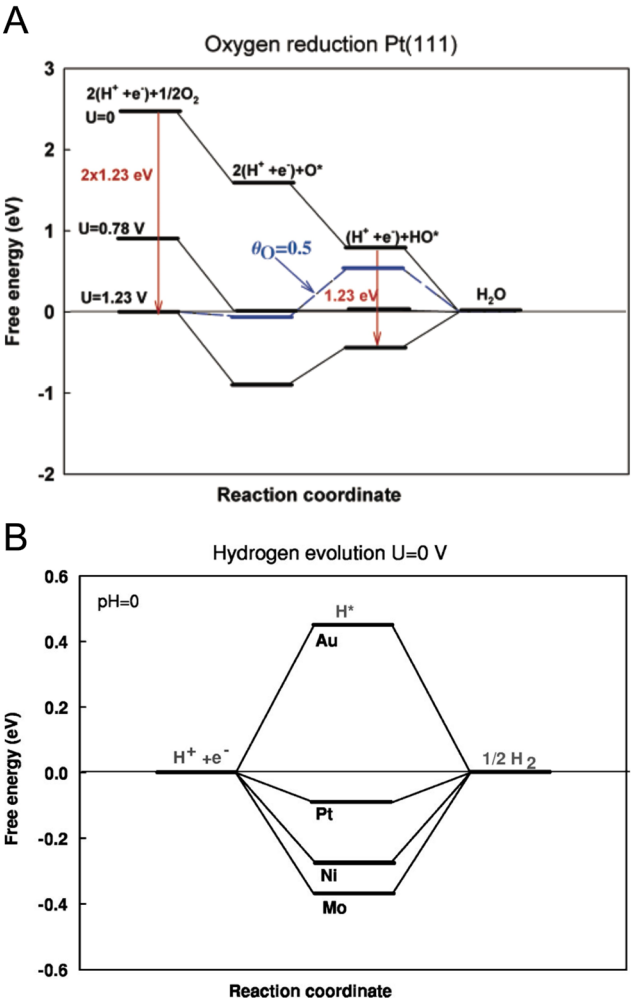

Figure 2. Potential-dependent PCET reaction free energies using the computational hydrogen electrode (CHE) model. (A) Free energy diagram for the oxygen reduction reaction on Pt(111) at three different applied potentials. At the equilibrium potential (1.23 V vs SHE), the reactants ($2H^+$, $2e^-$, $1/2O_2$) have the same free energy as the product (H_2O). At 0 V vs SHE, the reaction free energy is 2.46 eV because there are two proton−electron pairs in the reactants. The potential-dependent free energy of a proton−electron pair relative to the SHE is adjusted by an amount equivalent to the applied potential, according to eq 3. The blue calculation labeled θ_O = 0.5 corresponds to calculations at 1.23 V with an O atom surface coverage of 0.5 ML. Panel reproduced with permission from ref 58. Copyright 2004 from the American Chemical Society. (B) Free energy diagram for the hydrogen evolution reaction on close-packed metal (111) surfaces at the reaction equilibrium potential, 0 vs SHE. Panel reproduced with permission from ref 63. Copyright 2005 The Electrochemical Society.

electrochemical PCET, the proton-coupled redox potential is defined as the potential at which a proton adsorbs to or desorbs from an electrode surface, concurrently with an electron provided by or removed by the external circuit of the electrode. The BDFE is the free energy associated with removing an adsorbed H atom from the electrode surface to bulk solvent. The hydrogen binding free energy, which is related to these quantities, is of great interest for many electrocatalytic reactions with PCET elementary steps, especially for the hydrogen evolution reaction (HER), wherein it is commonly employed as a catalytic activity descriptor.[63,64,77−79] For example, the free energy diagram shown in Figure 2B suggests that the optimal

https://doi.org/10.1021/acs.chemrev.1c00929
Chem. Rev. XXXX, XXX, XXX−XXX

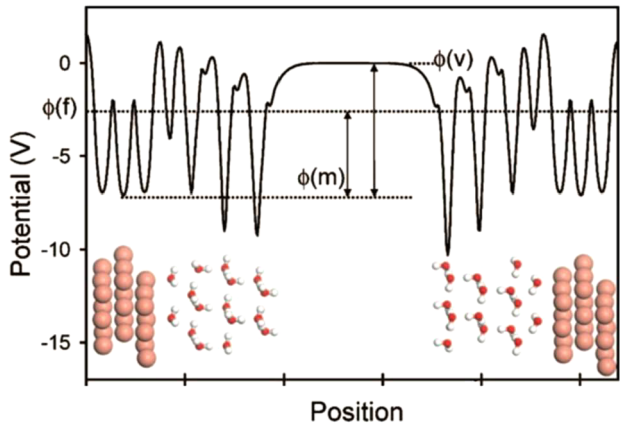

Figure 3. A schematic of the electrostatic potential profile across a periodic unit cell used to compute the work function and electrode potential. Here, explicit water layers are included on each side of a Cu(111) slab with a region of vacuum in between. The potentials ϕ(v), ϕ(m), and ϕ(f) denote the vacuum reference, bulk metal, and Fermi potentials. The vacuum reference and the Fermi energy $\varepsilon_F = \phi(f)/e$ can be used to compute the work function. Figure reproduced with permission from ref 73. Copyright 2006 American Physical Society.

catalyst for HER in acid is one where the hydrogen binding free energy is zero at 0 V vs SHE, as the reaction involves only a single adsorbed intermediate. In this figure, the metal that most closely aligns with these optimal conditions is Pt,[63] but within this model a surface that has a perfectly thermoneutral hydrogen binding free energy may further enhance the HER rate. Although the actual HER rate depends on other quantities, including the operating overpotential, coverage, and kinetics of elementary steps,[80−82] such BDFEs are nonetheless critical properties in electrocatalysis.

In general, trends in BDFEs and proton-coupled redox potentials determined from quantum chemical methods such as DFT are more reliable than absolute magnitudes of these properties. As a result, internal reference reactions are commonly used to evaluate such trends. For example, hybrid periodic DFT was used to calculate the proton-coupled redox potentials of NiFe oxyhydroxides, referencing all calculations to the experimentally determined $Ni^{2+/3+}$ redox potential for the undoped $NiOOH_x$ system (Figure 4A).[83] In an analysis of graphite-conjugated catalysts, proton-coupled redox potentials of the terminal organic acid sites, E^{acid}_{PCET}, were computed relative to those at the connecting phenazine bridge, E^{phen}_{PCET}, where $\Delta E_{PCET} = E^{acid}_{PCET} - E^{phen}_{PCET}$ (Figure 4B).[84] The calculated E^{phen}_{PCET} was used as a reference redox potential because it was shown experimentally to be consistent for different graphite-conjugated acids.[85,86] The ΔE_{PCET} predicted from DFT showed close agreement with experimental measurements and predicted the PCET thermochemistry of newly synthesized materials (Figure 4B).[84]

The BDFEs of X−H bonds can be determined (in kcal/mol) from calculated or electrochemically measured proton-coupled redox potentials, E°_{PCET} (at pH 0, vs SHE), by the expression[6,88]

$$\mathrm{BDFE(X-H)} = 23.06\, E^{\circ}_{PCET}(\mathrm{pH}=0) + C_{sol} \quad (5)$$

where C_{sol} is related to the ionization and solvation free energies of a hydrogen atom in the working solvent.[89] This relation was demonstrated in recent experiments by Wise and Mayer,[90] where BDFEs of surface O−H bonds on nickel oxide were determined using experimentally measured redox potentials (Figure 5A) and eq 5. In additional experiments, a solid $Ni^{III}O(OH)$ surface was oxidized with a series of different hydrogen atom transfer reagents, and the BDFE of the reagent associated with $Ni^{III}O(OH)$ and $Ni^{II}(OH)_2$ at equilibrium was similar to the BDFE measured electrochemically (Figure 5B).

Building off these experimental findings, hybrid functional periodic DFT was used to analyze BDFEs for O−H bonds on anatase TiO_2 surfaces.[92] In this study, the CHE model was used to calculate E°_{PCET} in the BDFE expression given in eq 5. This analysis demonstrated that geometrically similar O−H bonds have BDFEs that vary by ∼81 kcal/mol (3.50 eV) depending on whether the redox reaction (i.e., ET) involved proton-induced defects at the valence p- or conduction d-band edge.[92] By using a square scheme approach commonly employed in molecular catalysis, the proton-coupled redox potentials for the interfacial PCET reactions at TiO_2 surfaces (Figure 6A) were broken down into their constituent ET and PT reaction free energies (Figure 6B). In turn, the difference in the two types of BDFEs (ΔBDFE) was shown to be nearly equivalent to the difference in ET driving forces (Figure 6C), which were evaluated using a Marcus theory framework (Figure 6D) to calculate vertical energy gaps and inner-sphere reorganization energies. The interpretation of electrochemical PCET thermochemistry in terms of BDFEs

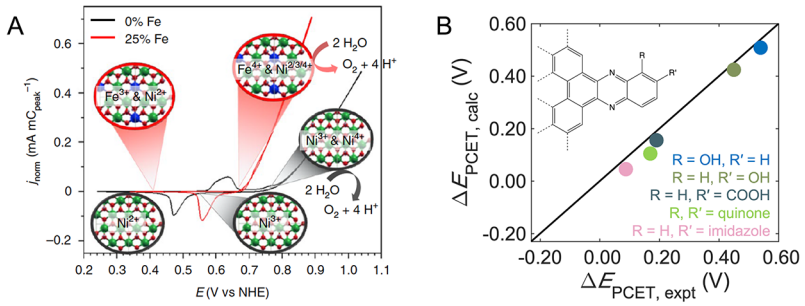

Figure 4. Example systems using internal PCET reference reactions to evaluate trends in proton-coupled redox potentials. (A) Predicted changes in Fe and Ni oxidation states coinciding with PCET reactions as a function of applied potential on $Ni_xFe_{1-x}OOH$ electrodes. Proton-coupled redox potentials are calculated relative to the computed $Ni^{2+/3+}$ potential of the Fe-free NiOOH system and compared with cyclic voltammetry measurements. Panel is reproduced with permission from ref 87. Copyright 2021 Springer Nature. (B) Parity plot between calculated and experimentally measured proton-coupled redox potentials for different graphite-conjugated organic acids. Here, $\Delta E_{PCET} = E^{acid}_{PCET} - E^{phen}_{PCET}$ is the difference between the proton-coupled redox potentials for protonation at the acid site (functionalized at the R and R′ positions shown in the inset) and the proton-coupled redox potential for the double protonation of the phenazine bridge. Panel reproduced with permission from ref 84. Copyright 2020 American Chemical Society.

https://doi.org/10.1021/acs.chemrev.1c00929
Chem. Rev. XXXX, XXX, XXX−XXX

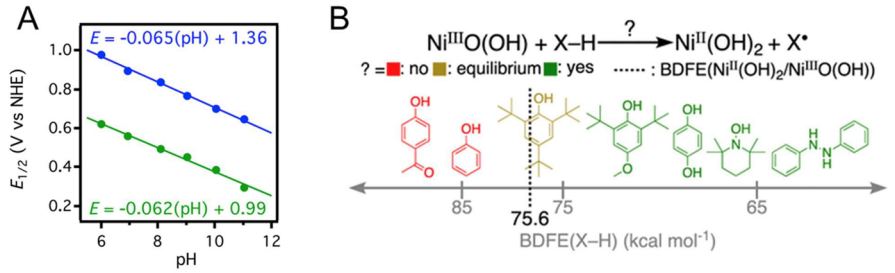

Figure 5. (A) Plot of $E_{1/2}$ for the Ni^{IV}/Ni^{III} (in blue) and Ni^{III}/Ni^{II} (in green) potentials determined from cyclic voltammograms of nickel oxide in aqueous solution, each with a roughly Nernstian dependence on pH. The redox potentials extrapolated to pH 0 are used to determine O−H bond dissociation free energies (BDFEs) of 75.6 and 84.2 kcal/mol for $Ni^{II}(OH)_2$ and $Ni^{III}O(OH)_2$, respectively, using eq 5. (B) Summary of reactivity at $Ni^{III}O(OH)$ with hydrogen atom transfer oxidants containing different X−H BDFEs. $Ni^{III}O(OH)$ and $Ni^{II}(OH)_2$ are in equilibrium when the BDFE of the molecule is approximately equal to the O−H BDFE of $Ni^{II}(OH)_2$ measured electrochemically. Panel A reproduced with permission from ref 90. Copyright 2019 American Chemical Society. Panel B reproduced with permission from ref 91. Copyright 2020 American Chemical Society.

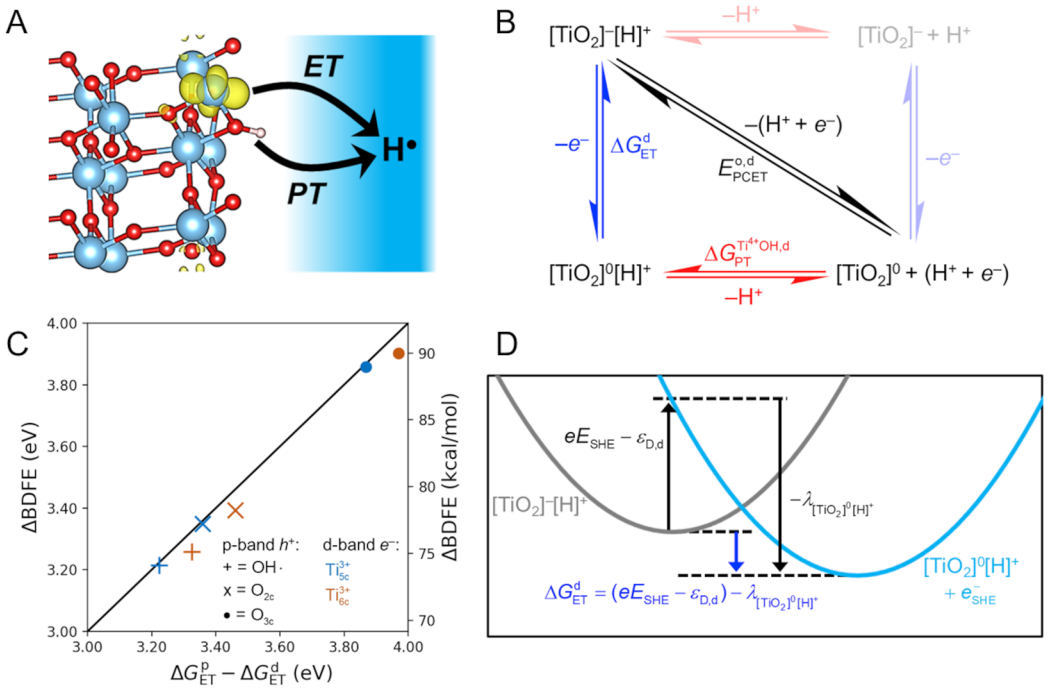

Figure 6. (A) Schematic of interfacial PCET at anatase $TiO_2(101)$ surface involving an electron in the conduction d-band, as shown by the yellow isosurface localized on a surface Ti^{3+} ion. (B) Square scheme for the PCET reaction shown in (A). (C) Parity plot between the difference in BDFEs and electron transfer driving forces for PCET reactions involving different combinations of p-band holes and d-band electrons for a set of model systems. (D) Marcus parabolas used to evaluate ET driving forces ΔG_{ET}, which are the difference between the vertical energy for ET from the defect in the conduction d-band (upward black arrow) and the reorganization energy λ associated with ET (downward black arrow). Figure reproduced with permission from ref 92. Copyright 2021 American Chemical Society.

provides a direct connection to *in situ* or *operando* experimental characterization.

2.4. Constant Potential Methods for Electrochemical PCET

Experimental measurements of electrochemical PCET thermodynamic properties typically occur at constant potential. Computational chemistry methods such as DFT are typically performed with the number of electrons N_e fixed. In electrochemical systems, however, N_e can fluctuate to maintain a constant electrochemical potential of electrons, $\tilde{\mu}_e$, which is related to the electrode potential E. The relevant thermodynamic quantity for electrochemistry is therefore the grand potential Ω. As mentioned in section 2.2, the effects of electrode potential are often applied *a posteriori* through eq 3. This treatment typically entails using charge-neutral model systems that do not enforce charge equilibrium criteria of the grand canonical ensemble corresponding to constant applied potential. Consequently, all PT reactions are explicitly modeled as concerted PCET, and all ion electrosorption valencies are limited to integer values. In some cases, the CHE model also may not capture potential-dependent geometries of reactants, products, or transition states in PCET processes. To address these limitations, constant potential methods have been developed and used to analyze PCET thermodynamics at constant potential.

Various computational approaches have been developed to model charged surfaces with periodic boundary conditions, enabling constant-potential quantum chemical calculations. At constant $\tilde{\mu}_e$ and variable N_e, the grand potentials of different structures can be calculated to evaluate relative thermodynamic stabilities.[93,94] Calculations of surfaces are generally performed

https://doi.org/10.1021/acs.chemrev.1c00929
Chem. Rev. XXXX, XXX, XXX−XXX

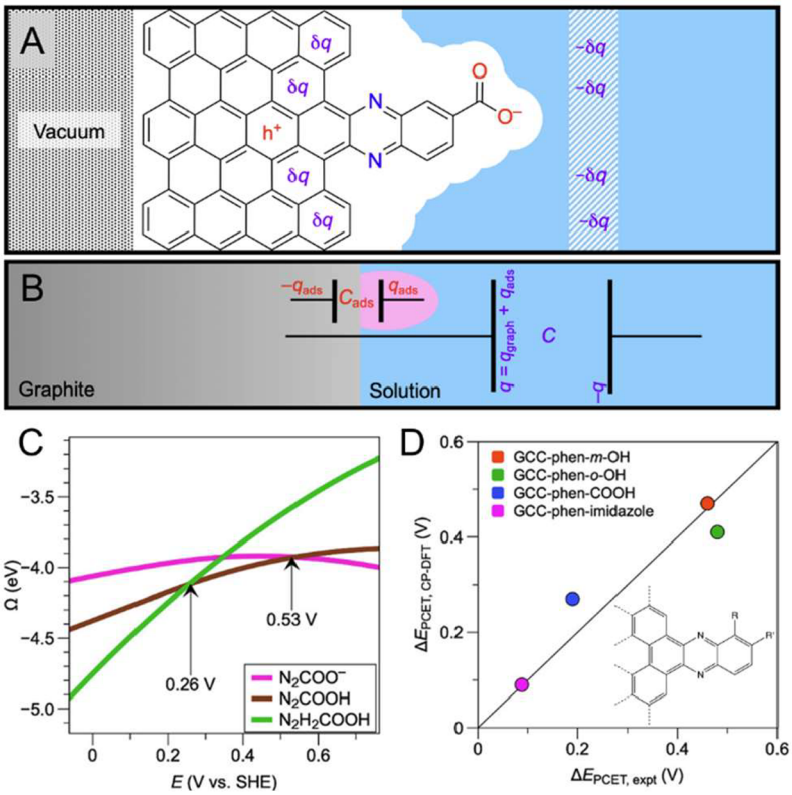

Figure 7. (A) Computational unit cell setup for the COO^- termination of the graphite-conjugated phenazine carboxylic acid, GCC-phen-COOH. The net charge q in the atomistic system (sum of δq on carbon surface) is compensated by the strip of countercharges in dielectric continuum solvent (purple $-\delta q$ on diagonal striped blue strip). The negatively charged carboxylate induces a positive hole, h^+, on the carbon surface. (B) A schematic of the two capacitors present within the computational model, with one capacitor (total system) of charge q and capacitance C and the other (charged adsorbate) of charge q_{ads} and capacitance C_{ads}. For these capacitors electrically connected in parallel, the total energy of the interface can be represented by a single effective capacitor related to the charge on the graphite surface of charge q_{graph} and capacitance C_{graph}. (C) PCET reactions at the acid and phenazine sites in the GCC-phen-COOH system. The grand potential Ω is computed as a function of applied potential E for the three different surface terminations. The curve intersections correspond to the proton-coupled redox potentials for PCET at the phenazine bridge (green−brown intersection at low potential) and the terminal carboxylic acid site (brown−pink intersection at higher potential). (D) Parity plot between calculated and experimentally measured proton-coupled redox potentials for different graphite-conjugated organic acids. Here $\Delta E_{PCET} = E^{acid}_{PCET} - E^{phen}_{PCET}$ is the difference between the proton-coupled redox potentials for protonation at the acid site (functionalized at the R and R′ positions shown in the inset) and the proton-coupled redox potential for the double protonation of the phenazine bridge. These calculations were performed with constant potential methods, which are independent of cell size, whereas the results in Figure 4B were performed with constant charge methods relying on unit cell-size extrapolation techniques and, in some cases, additional adsorbates. Figures reproduced with permission from ref 119. Copyright 2021 American Chemical Society.

on slab models that are periodic in all three directions, so charged atomistic systems must be compensated by countercharges within the unit cell to prevent the electrostatic potential and energy from diverging. Various charge compensation methods have been used in the analysis of electrochemical processes,[95] including a homogeneous background charge,[73,96−99] explicit counterions or a counterelectrode,[74,100−104] or a two-dimensional strip of countercharge (e.g., solvated jellium or fictitious charged particle methods).[45,105−113] An alternative approach entails utilization of real-space codes such as GPAW[113] that allow two-dimensional periodicity, circumventing such divergence issues and the need for charge compensation. Constant-potential PCET reaction free energies can be computed from a series of constant-charge calculations. The electrode potential E can be computed for each charge, enabling a subsequent grid-based mapping of the free energies as a function of E. These analyses can also be performed using constant-potential calculations, where the grand potential is variationally minimized by using Lagrange multipliers that enforce a target electron chemical potential constraint, rather than an electron number constraint. Such methods have been implemented in the JDFTx[114] and GPAW[113] codes.

PCET reaction free energies in the grand canonical ensemble can be calculated as the difference in the grand potentials of products (P) and reactants (R) at a given potential E:

$$\Delta\Omega = \Omega_P(E) - \Omega_R(E) \tag{6}$$

As the reaction free energies are determined at a given E, proton−electron transfer is not obligatorily concerted; i.e., the number of added/removed protons between reactants and products is not necessarily equal to the number of added/removed electrons. In contrast to the CHE model, the electrochemical potentials of protons and electrons are treated independently on absolute potential scales rather than referenced to the chemical potential of H_2 gas at SHE conditions, as in eq 3.[73,74,97,107,113,115]

The internal energy U of a charged interface as a function of charge tends to be roughly parabolic in charge q. This behavior has been noted in various computational studies,[108,110,116−118] including analyses of PCET systems, and can be understood by

https://doi.org/10.1021/acs.chemrev.1c00929
Chem. Rev. XXXX, XXX, XXX−XXX

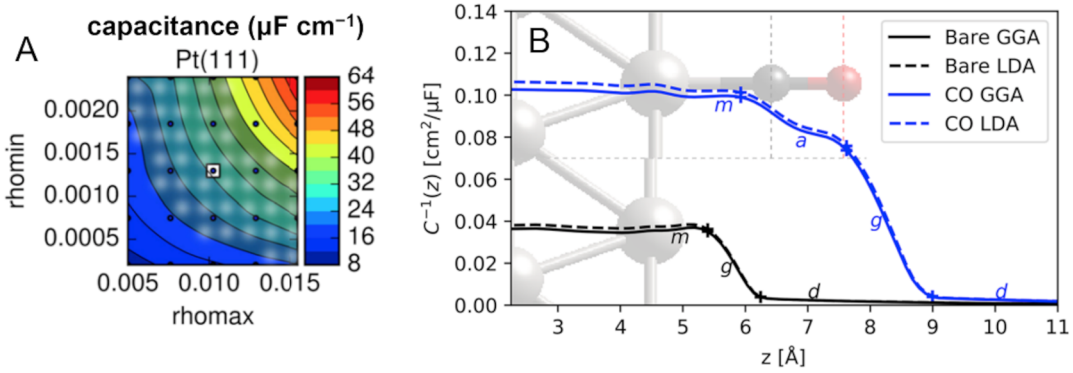

Figure 8. (A) Computed interfacial capacitance for Pt(111) in implicit water using different $\rho_{min/max}$ parameters of the density-dependent interface switching function. The boxed data point corresponds to the parameters chosen based on agreement with experimental measurement. Figure reproduced with permission from ref 107. Copyright 2019 American Institute of Physics. (B) Inverse capacitance, C^{-1}, of Pt(111) with (in blue) and without (in black) CO adsorbed on the surface. The inverse capacitance C^{-1} is defined in this figure as $C^{-1} = \partial \bar{\phi}(z)/\partial N$, where N is the number of electrons in the DFT calculation and $\bar{\phi}(z)$ is the planar-averaged electrostatic potential along the z-axis of the simulation cell. The different capacitors in series are m = metal, a = CO adlayer, g = gap, and d = diffuse capacitance. Figure reproduced with permission from ref 125. Copyright 2017 American Chemical Society.

expanding U about an uncharged interface, i.e., $q = 0$, in a Taylor series:

$$U \approx U_0 + q\left.\frac{\partial U}{\partial q}\right|_{q=0} + \frac{1}{2}q^2\left.\frac{\partial^2 U}{\partial q}\right|_{q=0} \tag{7}$$

Here the first derivative corresponds to the electrode potential of the uncharged interface, E_0, and the second derivative is the inverse of the capacitance, C, such that

$$\begin{aligned} U &\approx U_0 + qE_0 + \frac{q^2}{2C} \\ &= U_0 + qE_0 + \frac{q}{2}(E - E_0) \end{aligned} \tag{8}$$

where the second equality is obtained using the relation $q = C(E - E_0)$. This expansion can be generalized to include multiple charging components, such as explicit ions and surface adsorbates, in the form of a Taylor series expansion about multiple variables.[108,110]

A computational analysis of PCET reactions at the surface of graphite-conjugated organic acids showed that the energetics of interfaces containing adsorbates with constant charge are determined by the graphite electrode surface charge, q_{graph}.[119] In this case, the Taylor series expansion for an interface that is polarized by both counter-charges in the EDL, denoted q, and constantly charged adsorbates, q_{ads}, simplifies to a function of q_{graph} only (Figure 7A–B):

$$U = U_0 + q_{graph}E_0 + \frac{1}{2}q_{graph}(E - E_0) \tag{9}$$

where E_0 is the graphite electrode potential of zero free charge (PZFC). This result was consistent with earlier work, which demonstrated that constant-charge PCET reaction energetics are uniquely defined as a function of the effective surface charge.[110] The computational analysis of the graphite-conjugated organic acids showed that the internal energy $U[q_{graph}(E)]$ can be calculated using the DFT energy U_{DFT} and a shift associated with the capacitive contributions of the constantly charged surface adsorbate:[119]

$$U[q_{graph}(E)] = U_{DFT}[q_{graph}(E), q_{ads}] + \frac{1}{2}q_{ads}(E - E_0) \tag{10}$$

The energetic shift arises because the internal energy is a function of surface charge q_{graph}, whereas DFT calculations are performed at constant total (i.e., net) charge $q = q_{graph} + q_{ads}$. Note that the contributions of the adsorbate capacitor become small with increased unit cell size, and therefore the results obtained using this constant-potential approach are similar to those obtained using cell-size extrapolation techniques with constant-charge calculations.[84]

This multicapacitor formulation, which is depicted schematically in Figure 7A–B, was used to calculate proton-coupled redox potentials for graphite-conjugated organic acids within the grand canonical ensemble. In particular, eq 10 was used to compute the internal energy for grid points of varying charge q, which in turn were mapped onto grid points of varying computational electrode potential E. The grand potential Ω was calculated from

$$\begin{aligned} \Omega(E) = {} & U_{DFT}[q_{graph}(E), q_{ads}] + \frac{1}{2}q_{ads}(E - E_0) + \mathrm{ZPE} \\ & - TS - G_{ref} - N_{H^+}\left[\frac{1}{2}\mu_{H_2} - e(E - E_{SHE})\right] - qE \end{aligned} \tag{11}$$

where ZPE is the zero-point energy, T is the temperature, S is the entropy, N_{H^+} is the number of added protons, and G_{ref} is a reference Gibbs free energy. Using eq 11, the grand potential curves were computed as a function of E for different graphite conjugated catalyst (GCC) surface terminations (Figure 7C). Analysis of the intersections of different grand potential curves yielded proton-coupled redox potentials that were independent of unit cell size and in good agreement with both constant-charge calculations relying on cell-size extrapolation techniques and experimental measurements for various GCCs. This study highlighted the utility of grand canonical analyses of PCET thermochemistry, which can circumvent the need to perform unit-cell extrapolation calculations.[119]

In the context of constant-potential methods, these types of multicapacitor models are useful for studying electrochemical PCET reactions. However, many challenges arise in efforts

https://doi.org/10.1021/acs.chemrev.1c00929
Chem. Rev. XXXX, XXX, XXX–XXX

aimed at an accurate description of the interface capacitance. For example, computed capacitances are sensitive to the parameters of implicit solvent models,[107,109,110] including the electron density-dependent interface switching functions for the continuum dielectric (Figure 8A). Moreover, the contributions of specifically adsorbed molecules or molecular fragments can have a significant impact on the overall interfacial capacitance, especially when hydrophobic surface terminations or ordered low-dielectric solvent manifests in large gradients in the electrostatic potential (i.e., large interfacial electric fields) at the electrode−electrolyte interface (Figure 8B). Improved descriptions of interfacial electrostatics may be achieved through explicit simulation of solvent and ions,[103] tuning implicit solvent parameters to benchmark against experimentally measured capacitance,[107,110] or using classical DFT for a self-consistent determination of the interfacial dielectric environment based on nuclear densities of solvent molecules.[120−124]

Another compelling example of grand canonical DFT calculations is the investigation of H adsorption free energies on nitrogen-doped graphene and MoS_2.[126] The band structure of common two-dimensional materials was found to have a significant impact on the occupation of electronic states with applied potential. In particular, the associated changes in the surface charge of these materials significantly impact H adsorption free energies, i.e., PCET thermochemistry. This work demonstrated that charge-neutral approaches can fail to capture even qualitative conclusions, such as whether H adsorption is exothermic at a given applied potential (Figure 9).[126] Both models capture the expected result that H

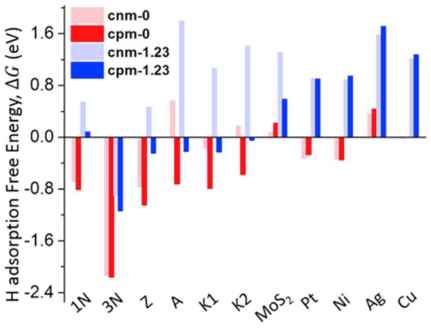

Figure 9. H atom (i.e., proton−electron pair) adsorption free energy ΔG at 0 and 1.23 V vs SHE computed using the charge-neutral CHE model (denoted "cnm") and constant potential methods (denoted "cpm"). Calculations were performed on pyridinic N-doped graphene at sites containing 1 N atom in the basal plane (1N), 3N atoms in the basal plane (3N), a N atom at the zigzag edge (Z), a N atom at the armchair edge (A), and a N atom at two different kink sites (K1 and K2). The results for these and 2D MoS_2 are compared to 3D metal(111) surfaces. Figure reproduced with permission from ref 126. Copyright 2018 American Chemical Society.

adsorption (proton reduction) becomes more exothermic with increasing potential because there is less negative charge density on the electrode surface under these conditions. However, H adsorption energies calculated using the CHE model at 0 V (cnm-0 in Figure 9) and 1.23 V (cnm-1.23) vary by 1.23 eV by construction. The constant potential approach accounts for deviations from this construction because the calculations are performed using different electrode surface charges corresponding to 0 V (cpm-0) and 1.23 V (cpm-1.23).

Grand canonical methods have also been shown to be essential for computing the pH dependence of proton electrosorption on Pt(111). The electrosorption potentials, denoted U_{RHE}^{sorp}, were calculated relative to the pH-corrected RHE scale (Figure 10A).[108] These potentials were calculated as a

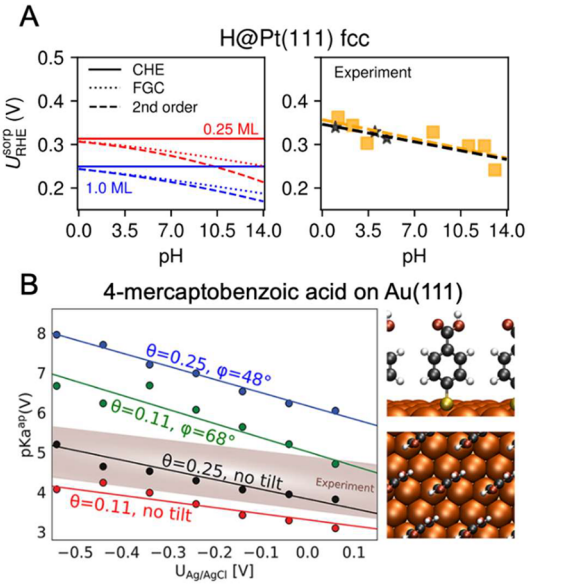

Figure 10. (A) Proton electrosorption potentials for Pt(111) computed at 0.25 ML (red) and 1.0 ML coverage of adsorbed H*. The calculations shown on the left used the charge-neutral CHE model, a fully grand canonical (FGC) model, and a second-order Taylor expansion of interface energies with respect to surface charge (second order). The experimental electrosorption potentials (right) were obtained from ref 129 (orange squares) and ref 130 (black stars). Panel reproduced with permission from ref 108. Copyright 2020 Hörmann, Marzari, and Reuter under CC BY 4.0 license https://creativecommons.org/licenses/by/4.0/. (B) The computed apparent pK_a versus applied potential for 4-mercaptobenzoic acid on Au(111). θ is the surface coverage of the molecule, and φ is the tilt angle. Panel reproduced with permission from ref 127. Copyright 2020 American Chemical Society.

function of pH at two different H surface coverages. Although the RHE scale is pH-independent using the CHE model, intrinsic pH dependencies were introduced using a second-order Taylor expansion of charge-neutral calculations (analogous to the expansion in eq 8) and using a variable charge "fully grand canonical" approach. By construction, U_{RHE}^{sorp} is independent of pH within the CHE model because protons and electrons are added in equal ratios (solid curves, left side of Figure 10A). However, both the second-order expansion and the fully grand canonical calculations were able to reproduce the experimentally observed (right side of Figure 10A) trends in U_{RHE}^{sorp}.[108]

A final representative example is the use of grand canonical DFT calculations to study the heterogeneous PCET reaction of 4-mercaptobenzoic acid adsorbed on Au(111).[127] In particular, the apparent pK_a values were computed as a function of the applied potential by decoupling the chemical potentials of electrons and protons in the thermodynamic model. The slopes of the calculated potential-dependent apparent pK_a values (Figure 10B) deviated from the expected Nernstian 59 mV/pH unit shift for concerted PCET. The theoretical calculations were supported by complementary experiments performed using 4-mercaptobenzoic acids adsorbed on polycrystalline Au thin films. The DFT calculations at 0.25 ML 4-mercaptobenzoic acid surface coverage and the accompanying experimental measure-

https://doi.org/10.1021/acs.chemrev.1c00929
Chem. Rev. XXXX, XXX, XXX−XXX

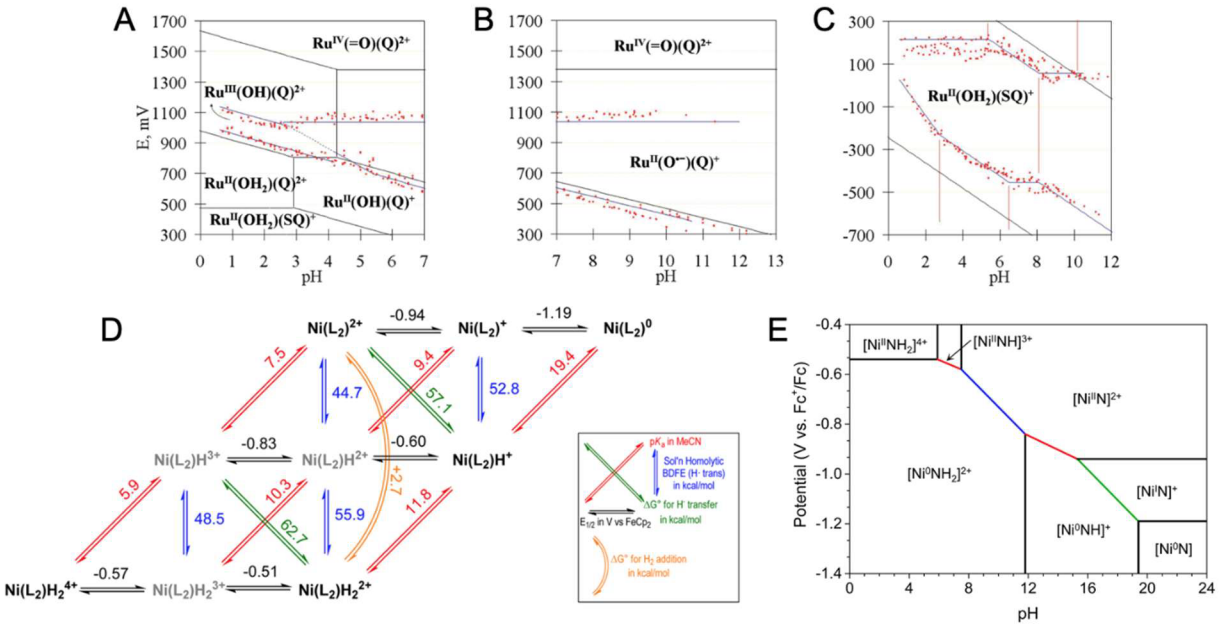

Figure 11. (A–C) Experimental and theoretical Pourbaix diagram of $Ru(OH_2)(Q)(tpy)^{2+}$ in the (A) low pH and high potential region, (B) high pH and high potential region, and (C) low potential region. The red dots are experimental measurements of E (relative to SCE) at various pH values, and the dashed red and solid blue lines are experimental pK_a values and redox potentials, respectively. The black lines are theoretical predictions. Panels A—C reproduced with permission from ref 53. Copyright 2009 American Chemical Society. (D) Experimental and computational data for the $Ni(P_2N_2)_2$ catalyst, where the P_2N_2 ligands are denoted "L", and therefore $Ni(P_2N_2)_2$ is denoted $Ni(L_2)$. The species in gray are not directly observed experimentally, and their thermodynamic stability relative to the other compounds is determined using DFT calculations. (E) Pourbaix diagram determined from the thermodynamic data in (D). The vertical and horizontal lines correspond to pK_a values and redox potentials, respectively. The red lines have a slope of ~29.5 mV/pH unit ($2e^-$, $1H^+$ transfer). The blue and green lines each have a slope of ~59 mV/pH unit, where the blue line is a $2e^-$, $2H^+$ transfer process, and the green line is a $1e^-$, $1H^+$ transfer process. Panels D and E are reproduced with permission from ref 132. Copyright 2013 American Chemical Society.

ments (Figure 10B) demonstrated a partial charge transfer of ~0.1 electrons per proton from the electrode to the adsorbed hydrogen atom. This result suggested that 90% of the potential drop occurs across the self-assembled monolayer.[127] These results and interpretations were subsequently augmented by additional experiments.[128]

2.5. Pourbaix Diagrams of PCET Systems

The thermodynamic approaches discussed in subsections 2.1–2.4 can be used to calculate *ab initio* Pourbaix diagrams for electrochemical PCET systems. In this context, Pourbaix diagrams are phase diagrams with applied potential E and pH as the independent variables.[131] From a more general thermodynamic perspective, the *ab initio* phase diagram approach entails representing the most stable phase (i.e., redox and protonation state for PCET) of a chemical system at a given set of conditions. In this subsection, we will briefly highlight some computational Pourbaix analyses pertaining to PCET processes in homogeneous and heterogeneous systems. These Pourbaix diagrams are plotted with pH and potential on the horizontal and vertical axes, respectively. Hence, the vertical, horizontal, and diagonal lines on these diagrams correspond to PT, ET, and concerted PCET, respectively.

As an example of such analyses applied to homogeneous PCET systems, theoretical calculations in combination with experimental studies were used to gain insights into the Pourbaix diagram of $Ru(OH_2)(Q)(tpy)^{2+}$ (Q = 3,5-di-*tert*-butyl-1,2-benzoquinone, tpy = 2,2′:6′,2″-terpyridine) molecular water oxidation catalysts.[53] To aid in characterizing the different redox states of the catalyst, complete active space self-consistent-field (CASSCF) calculations were used to analyze ferromagnetic and antiferromagnetic spin states, and time-dependent DFT (TDDFT) was used to compare calculated UV–vis spectra to experiment. These analyses at various levels of theory helped inform the phases that were included on the $Ru(OH_2)(Q)(tpy)^{2+}$ Pourbaix diagram (Figure 11A–C) and elucidated each of the many species involved in PT, ET, and PCET reactions.[53]

In another study of homogeneous electrochemical PCET, the Pourbaix diagram of the $Ni(P_2N_2)_2$ (where P_2N_2 is 1,5-dibenzyl-3,7-diphenyl-1,5-diaza-3,7-diphosphacyclooctane) hydrogen evolution molecular electrocatalysts was computed.[132] Figure 11D shows the various ET or PT reactions of the $Ni(P_2N_2)_2$ catalyst determined from a combination of experimental[133] and theoretical[132] data. These data were converted into the Pourbaix diagram in Figure 11E, which demonstrates the thermodynamically relevant PT, ET, and PCET processes involving $Ni(P_2N_2)_2$ compounds. This Pourbaix diagram elucidates PCET mechanisms involving one-electron/one-proton transfers (green diagonal with slope of ~59 mV/pH unit), two-electron/two-proton transfers (blue diagonal with slope of ~59 mV/pH unit) and two-electron/one-proton transfers (red diagonals with slope of ~30 mV/pH unit).

In heterogeneous PCET systems, Pourbaix diagrams derived from first-principles calculations have been used to study ORR mechanisms on Pt(111), Ag(111), and Ni(111) surfaces under relevant reaction conditions.[134] Using the surface structures derived from the Pourbaix diagrams, the CHE model was used to determine the highest applied potential at which all PCET steps in the ORR pathway were downhill. The results obtained using Pt(111) and Ag(111) surface structures self-consistent with the Pourbaix diagram were similar to those obtained for

https://doi.org/10.1021/acs.chemrev.1c00929
Chem. Rev. XXXX, XXX, XXX–XXX

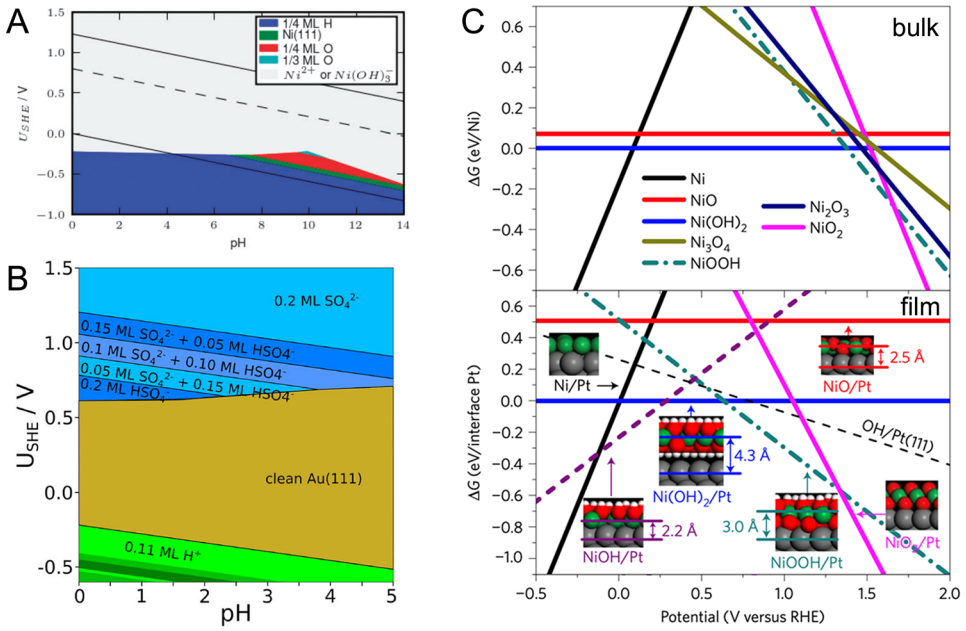

Figure 12. (A) Surface Pourbaix diagram for Ni(111), including acidic dissolution into Ni^{2+} and alkaline dissolution into $Ni(OH)_3^-$. The solid black lines correspond to thermodynamic equilibrium for water oxidation (higher potentials) and hydrogen evolution (lower potentials), and the dashed line represents a "good" ORR catalyst operating at 0.8 V vs RHE. Reproduced from ref 134 with permission from the PCCP Owner Societies Copyright 2008 Royal Society of Chemistry. (B) Surface Pourbaix diagram of adsorbed H^+, SO_4^{2-}, and HSO_4^- on Au(111). Reproduced with permission from ref 135. Copyright 2020 Gossenberger, Juarez, and Groβ under CC BY 4.0 license https://creativecommons.org/licenses/by/4.0/. (C) Electrochemical phase diagram for bulk Ni (top) and Ni films on Pt(111) (bottom) at pH 13. The Ni film phases corresponding to each data trace are shown as color-coded insets. The dashed black line corresponds to the energetics for OH^- adsorption on Pt(111). Reproduced with permission from ref 136. Copyright 2017 Springer Nature.

bare surfaces that did not contain spectator surface adsorbates. Because Ni(111) becomes partially oxidized under ORR conditions (red region in Figure 12A), however, the spectator O* adsorbates facilitate O_2 adsorption and reduction through PCET to form HOO*, which is predicted to be the rate-limiting step. In contrast, ORR modeling on the bare Ni(111) surface predicted an onset potential nearly 0.3 V lower because of facile dissociation of O_2 and strong binding energies of O* and HO*. This study demonstrated the importance of determining the relevant surface composition to gain even qualitative insights into electrocatalytic mechanisms involving multiple PCET steps.[134]

Pourbaix diagrams can also account for the explicit adsorption of electrolyte ions on electrode surfaces. For example, the explicit adsorption of sulfate (SO_4^{2-}) and bisulfate (HSO_4^-) electrolyte ions on metal surfaces were considered in Pourbaix diagrams calculated under electrochemical conditions (Figure 12B).[135] The electrochemical potentials of SO_4^{2-} and HSO_4^- were treated using tabulated redox potentials for SO_4^{2-}/SO_2 and HSO_4^-/SO_2 electrochemical half-reactions, enabling simultaneous consideration of H^+, SO_4^{2-}, and HSO_4^- binding adsorption thermodynamics as a function of applied potential and pH. These diagrams reproduced experimental voltammetric data indicating stable SO_4^{2-} and HSO_4^- formation on Pt(111) and Ag(111). This approach demonstrates the generalizability of computational Pourbaix diagrams to rigorously analyze electrode surface structure under conditions of electrochemical PCET reactions.[135,137]

Another example of the use of Pourbaix diagrams to investigate heterogeneous electrochemical PCET is an application to the HER at (hydroxy)oxide thin films supported on transition metal surfaces.[136] The electrochemical Pourbaix diagrams of different bulk metal and (hydroxy)oxide phases were computed (top, Figure 12C) and compared to analogous phases as thin-film monolayer films supported on metal substrates (bottom, Figure 12C). Interestingly, this analysis demonstrated that interactions with the metal substrate modified the stability of certain (hydroxy)oxide phases and was also used to identify phases with stoichiometries that are unstable as bulk materials. The most thermodynamically stable structures identified by the computational Pourbaix diagrams were supported by *in situ* crystal truncation rod and X-ray absorption near edge spectroscopic measurements, and they were used to elucidate PCET mechanisms during HER catalysis.[136]

Although the Pourbaix diagrams of the heterogeneous PCET systems shown in Figure 12 were calculated using the CHE model, they could also be constructed using constant potential or grand canonical methods (section 2.4). These methods could incorporate phenomena such as noninteger electrosorption valencies and non-Nernstian effects into computational Pourbaix diagrams. Given the availability of constant potential methods in various electronic structure codes, such Pourbaix diagrams could be constructed to elucidate the surface states of heterogeneous catalysts under electrochemical reaction conditions.

2.6. Reorganization Energies

In the context of Marcus theory for electron transfer[19−22] and the PCET theories[24−27] discussed below, reorganization energies are critical parameters that impact the rate constants of ET, PT, and PCET processes. The reorganization energy λ is the free energy associated with changes in the solute structure or solvent polarization upon charge transfer. It is often convenient

https://doi.org/10.1021/acs.chemrev.1c00929
Chem. Rev. XXXX, XXX, XXX−XXX

to separate the contributions of the solute and solvent into the inner-sphere (λ_i) and outer-sphere (λ_o) reorganization energies, respectively. Typically, the inner- and outer-sphere reorganization energies are assumed to be independent and are computed separately, although in principle they could be computed simultaneously. For example, constrained DFT formalisms[138,139] applied to atomistic simulations in explicit solvent can be used to simultaneously calculate inner- and outer-sphere reorganization energies.[140,141] This section describes some of the computational methods that have been developed to compute the inner- and outer-sphere reorganization energies. The use of these reorganization energies to calculate PCET rate constants will be described in section 5 and section 6.

2.6.1. Inner-Sphere Reorganization Energies. The inner-sphere reorganization energies for ET reactions can be determined using two different approaches. In the first approach, λ_i is estimated within the harmonic approximation as a sum of energies arising from bond length changes Δx_j between the oxidized and reduced states of the solute molecule. In this approach, λ_i is approximated as[23,142,143]

$$\lambda_i = \sum_j \frac{f_j^{(r)} f_j^{(p)}}{f_j^{(r)} + f_j^{(p)}} (\Delta x_j)^2 \tag{12}$$

where the summation is over the relevant inner-sphere vibrational modes, $f_j^{(r)}$ and $f_j^{(p)}$ are the force constants for the jth inner-sphere solute vibrational mode in the reactant and product states, respectively, and Δx_j is the difference between the equilibrium values in the reactant and product states for the coordinate corresponding to the jth vibrational mode. For ET reactions, the reactant and product states correspond to the oxidized and reduced states. This approximate expression has been applied directly to PCET reactions to include the inner-sphere reorganization energy associated with metal−ligand bonds (i.e., the changes in these bond lengths for the reactant and product PCET states).[144,145] In principle, it could also be used to include the inner-sphere reorganization energy associated with all of the solute vibrational normal modes, excluding contributions from the transferring proton.

In the second approach, λ_i is estimated using the four-point scheme, which requires the calculation of the energies of the oxidized and reduced states at both the oxidized and reduced equilibrium geometries. The equilibrium geometries of the oxidized and reduced states are denoted Q^{Ox} and Q^{Red}, respectively. The inner-sphere reorganization energy associated with the oxidized state, λ_i^{Ox}, is the difference between the energy of the oxidized state at the equilibrium geometry of the reduced state and the energy of the oxidized state at the equilibrium geometry of the oxidized state: $\lambda_i^{Ox} = E_{Ox}(Q^{Red}) - E_{Ox}(Q^{Ox})$. The inner-sphere reorganization energy associated with the reduced state, λ_i^{Red}, is defined analogously as $\lambda_i^{Red} = E_{Red}(Q^{Ox}) - E_{Red}(Q^{Red})$. The overall inner-sphere reorganization energy is computed as the average of these two quantities:[146,147]

$$\begin{aligned}\lambda_i &= \frac{1}{2}[\lambda_i^{Ox} + \lambda_i^{Red}] \\ &= \frac{1}{2}[E_{Ox}(Q^{Red}) - E_{Ox}(Q^{Ox}) + E_{Red}(Q^{Ox}) - E_{Red}(Q^{Red})]\end{aligned} \tag{13}$$

Typically, these energies are computed as electronic energies in the gas phase based on the assumptions that the zero-point energy and entropic contributions cancel, and solvent effects are included in the outer-sphere reorganization energy.

The four-point scheme[146] has been extended to compute the inner-sphere reorganization energies for PCET.[148] For PCET reactions, the electron and proton are defined to be on their donors for the reactant and on their acceptors for the product. The PCET inner-sphere reorganization energy must account for the solute energy changes upon simultaneous electron and proton transfer. To aid in the description of the four-point scheme for PCET, the oxidized and reduced states can be assigned as the reactant and product, respectively. In this case, the proton is on its donor for the equilibrium geometry of the oxidized state Q^{Ox}, and the proton is on its acceptor for the equilibrium geometry of the reduced state Q^{Red}. For the calculation of $E_{Ox}(Q^{Red})$, the proton must be optimized on its donor with all other nuclei fixed to Q^{Red}. For the calculation of $E_{Red}(Q^{Ox})$, the proton must be optimized on its acceptor with all other nuclei fixed to Q^{Ox}. This method has been applied to a wide range of homogeneous molecular electrocatalysts.[32,33,148]

2.6.2. Outer-Sphere Reorganization Energies. The outer-sphere reorganization energy λ_o is associated with the translation and reorientation of the solvent molecules occurring in conjunction with the ET or PCET process. The simplest approach for computing the outer-sphere reorganization energy for electrochemical ET or PCET is to represent the solute as a point charge at the center of a spherical cavity in dielectric continuum solvent and use the following analytical expression:[23,149]

$$\lambda_o = \frac{(\Delta q)^2}{2}\left(\frac{1}{\epsilon_\infty} - \frac{1}{\epsilon_0}\right)\left(\frac{1}{a} - \frac{1}{2d}\right) \tag{14}$$

Here Δq is the change in charge upon ET or PCET, ϵ_∞ is the optical dielectric constant, ϵ_0 is the static dielectric constant, a is the cavity radius of the solute, and d is the distance between the solute and the electrode surface. In practice, the cavity radius a can be computed by equating the volume of a sphere of radius a to the volume of the cavity obtained with a dielectric continuum method such as PCM in conjunction with a DFT calculation of the molecular solute.[147] A schematic of this point-charge model for determining λ_o is depicted in Figure 13. Equation 14 is related to the two-sphere donor−acceptor model for homogeneous ET originally derived by Marcus,[19] where the donor−acceptor distance is between the charged solute and its image charge in the electrode. According to eq 14, λ_o will decrease as the redox molecule moves closer to the electrode (i.e., as d decreases), as also observed experimentally.[150]

An approach has also been developed to calculate the outer-sphere reorganization energy for electrochemical ET and PCET using the integral equation formalism within the polarizable continuum model (IEF-PCM) framework.[147] This approach separates the electronic and inertial polarization response of the solvent and accounts for the detailed molecular charge redistribution. The solute−solvent boundary is treated explicitly by the molecular-shaped cavity within the framework of PCM, and the effects of the electrode−solvent boundary are included with an external Green's function (Figure 14A).[147] For relatively simple molecules, this quantum chemistry-based approach yields similar results as the point-charge model given by eq 14.[147] Moreover, λ_o was found to decrease as the molecule moves closer to the electrode,[147] as also observed experimentally.[150] This IEF-PCM method was extended to incorporate the effects of low-dielectric regions of self-assembled monolayers

https://doi.org/10.1021/acs.chemrev.1c00929
Chem. Rev. XXXX, XXX, XXX−XXX

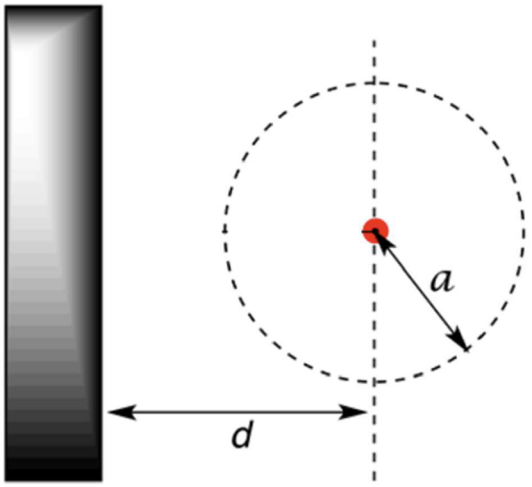

Figure 13. Schematic of the point-charge model for electrochemical outer-sphere reorganization energies. The point charge is shown by the filled red circle with a solute radius a at a distance d from the electrode (shown as the silver slab). Figure reproduced with permission from ref 147. Copyright 2014 American Chemical Society.

(SAMs) attached to electrodes (Figure 14B),[151] as well as the effects of the EDL and the ionic strength of the solvent[152] through the external Green's function. Moving beyond electrochemical ET, these methods were extended to electrochemical PCET and were shown to produce accurate total reorganization energies for two experimentally studied PCET systems (Figure 14C).[152]

The outer-sphere solvent reorganization energy for electrochemical ET and PCET has also been investigated using MD simulations with explicit solvent. Classical MD simulations were used to calculate free energy surfaces for outer-sphere ET reactions at electrodes to determine λ_o.[153−157] In another approach, constant-potential classical MD simulations were used to calculate λ_o based on the equilibrium statistics of the vertical energy gap of the reduced and oxidized states of the system.[158] The periodic model system, depicted in Figure 15, utilized a nondimensional Lennard-Jones unit system. In agreement with the point-charge model given by eq 14[23] and the IEF-PCM calculations,[147] these MD simulations also demonstrated attenuated λ_o values near electrode surfaces.

The effects of the temperature dependence of the outer-sphere reorganization energy and other thermodynamic parameters on the ET rates have been analyzed.[159−163] In the context of electrochemical PCET, however, these effects are not expected to be significant in the experimentally relevant temperature ranges.

3. ELECTROCHEMICAL PCET SURFACES AND BARRIERS

Computational studies of PCET kinetics using a method such as transition state theory require an estimate of the activation energies of PCET processes. These kinetic barriers are typically calculated using quantum chemical calculations of the minimum energy path (MEP) connecting the reactants and products of a PCET step. Combining transition state and reactant state electronic energies, zero-point energies, and entropies to compute the free energy barriers enables the estimation of PCET rate constants using transition state theory. In this section, we will focus on methods used to calculate activation energies for heterogeneous electrochemical PCET processes using potential energy surfaces derived from first-principles calculations. Special attention will be given to methodologies aimed at computing activation energies as a function of applied potential using constant-potential methods and deriving parameters relevant to the Butler−Volmer equation, such as electrochemical transfer coefficients. The last part of this section will describe the use of first-principles molecular dynamics simulations to compute free energy barriers and to investigate the dynamics of PCET reactions at electrochemical interfaces.

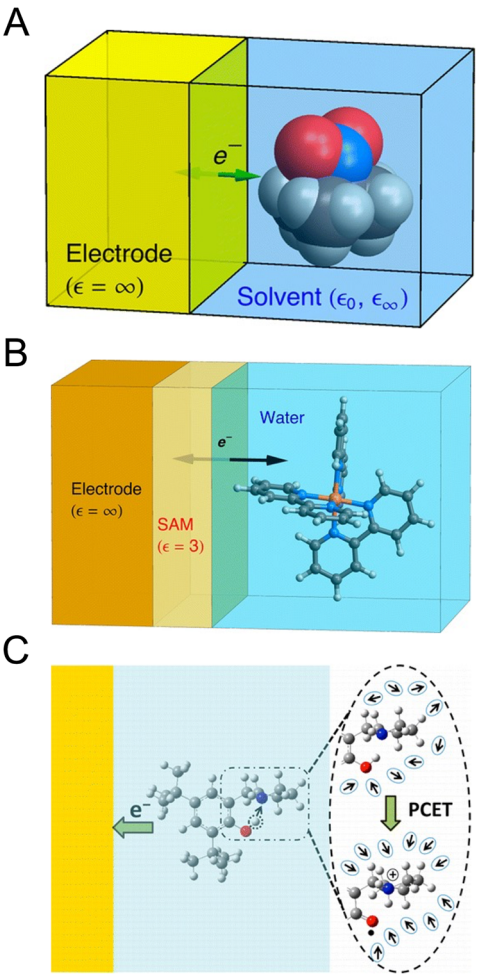

Figure 14. (A) Depiction of the IEF-PCM framework to calculate electrochemical solvent reorganization energies for outer-sphere ET reactions. Panel reproduced with permission from ref 147. Copyright 2014 American Chemical Society. (B) Schematic of framework to compute electrochemical solvent reorganization energies associated with redox molecules attached to or near a SAM-modified electrode, wherein the SAM region is modeled as an interfacial region of low dielectric constant. Panel reproduced with permission from ref 151. Copyright 2015 American Chemical Society. (C) Extension of the IEF-PCM framework to calculate electrochemical solvent reorganization energies for PCET systems. Panel reproduced with permission from ref 152. Copyright 2016 American Chemical Society.

3.1. First-Principles PCET Potential Energy Surfaces

Activation energies are typically calculated by identifying the first-order saddle point on the Born−Oppenheimer (i.e., electronically adiabatic) potential energy surface connecting the reactants and products.[164] One of the most common approaches is the nudged elastic band (NEB) method,[165−167]

https://doi.org/10.1021/acs.chemrev.1c00929
Chem. Rev. XXXX, XXX, XXX−XXX

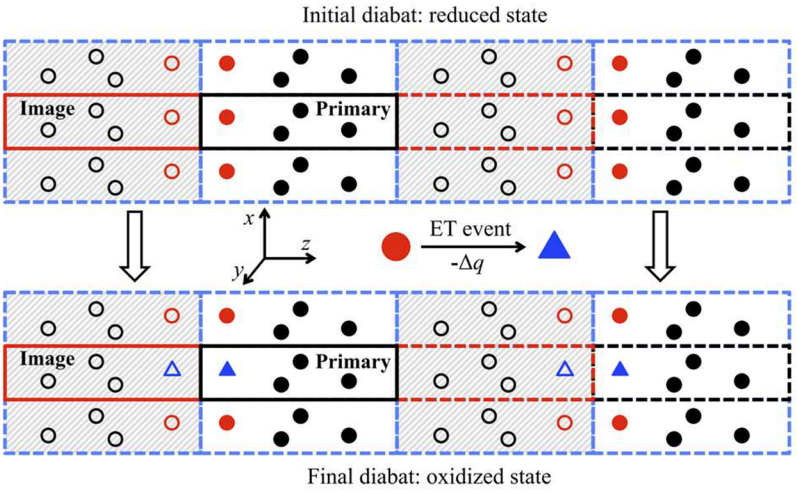

Figure 15. Schematic of computational unit cell in explicit simulations of outer-sphere reorganization energies using classical MD. The periodic boundary conditions are shown by dashed lines. The primary box contains the redox ion that is either in its reduced state (filled red circle in top panel) or oxidized state (filled blue triangle in bottom panel). Additional solvent molecules are shown as filled black circles. The reflections of all particles are in the image box and are depicted by open symbols. Figure reproduced with permission from ref 158. Copyright 2020 American Institute of Physics.

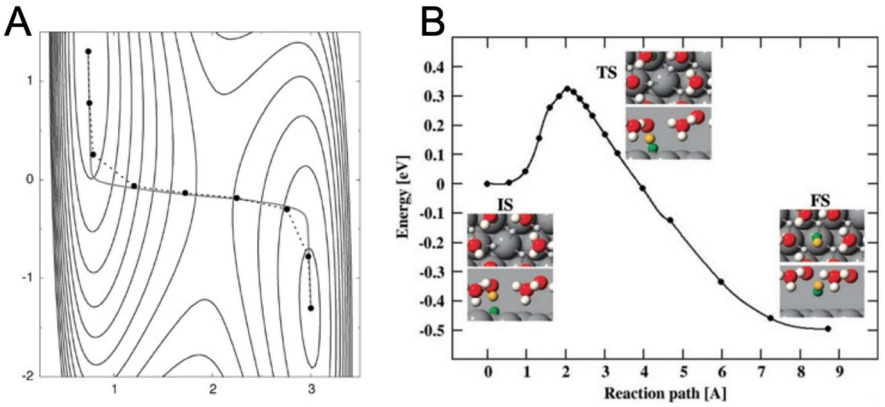

Figure 16. (A) Illustration of the nudged elastic band (NEB) method used to generate the minimum energy path (MEP) between two local minima of an adiabatic potential energy surface. The MEP computed using the NEB method is shown by the black dots, representing the images along the band, and the dashed lines connecting them. The actual MEP is shown by the solid black line. Reproduced with permission from ref 167. Copyright 2000 American Institute of Physics. (B) MEP calculated using the NEB method for the Heyrovsky PCET reaction ($H_{ads} + H^+ + e^- \rightarrow H_2$) on Pt(111). The initial state (IS), transition state (TS), and final state (FS) are shown along the reaction path. The solvated proton H^+ in the IS is shown in yellow, and the adsorbed H_{ads} is shown in green. Reproduced from ref 100 with permission from the PCCP Owner Societies. Copyright 2007 Royal Society of Chemistry.

which enforces harmonic interactions between adjacent configurations (i.e., images) connecting the initial and final states to mimic an elastic band that can be minimized to estimate the MEP (Figure 16A). The climbing image NEB method forces one of the images to the saddle point of the MEP, providing a direct estimate of the transition state geometry and energy. A more comprehensive review of these and related methods to locate transition states on adiabatic surfaces is provided elsewhere.[168]

Note that the NEB method and related methods are restricted to identifying saddle points and minima on Born−Oppenheimer potential energy surfaces. As such, these methods are only directly amenable to adiabatic PCET reactions that obey transition state theory, and they do not account for hydrogen tunneling or excited electron−proton vibronic states. However, a few computational studies in thermal heterogeneous catalysis have considered spin-crossover effects in hydrogen atom transfer reactions.[169−171] Theoretical approaches that include the effects of hydrogen tunneling and excited electron−proton vibronic states are described below in sections 5 and 6.

Calculations of adiabatic MEPs have found wide utility in various applications related to analysis of PCET steps in heterogeneous electrocatalysis. For example, the activation energies of different elementary PCET processes involved in the HER on Pt(111) were calculated using the NEB method.[100] This study represented the solvent as an ice-like layer of water and determined that the activation energies for proton adsorption through the Volmer reaction ($H^+ + e^- \rightarrow H_{ads}$) were computed to be quite low (<0.2 eV) at different levels of hydrogen surface coverage, supporting previous work suggesting that the Volmer reaction is fast on Pt(111). Additionally, these NEB methods were used to examine competition between the Tafel reaction ($2H_{ads} \rightarrow H_2$) and the Heyrovsky reaction ($H_{ads} + H^+ + e^- \rightarrow H_2$) for the hydrogen evolution step. The Tafel reaction does not involve electrons from the external circuit and therefore is not dependent upon the applied potential. However,

https://doi.org/10.1021/acs.chemrev.1c00929
Chem. Rev. XXXX, XXX, XXX−XXX

the Heyrovsky reaction is a potential-dependent PCET process wherein solvated protons in the EDL combine with electrons from the external circuit to react with adsorbed hydrogen, H_{ads}. Figure 16B shows the MEP computed for the Heyrovsky step and configurations corresponding to the initial state, transition state, and final state. Various intermediate images along the band are denoted by the filled black circles, and the maximum of the MEP is the estimate of the activation energy. This computational analysis indicated that the activation energies of the Tafel and Heyrovsky steps are similar, suggesting that both hydrogen evolution mechanisms could occur in parallel.

3.2. PCET Activation Energies at Constant Potential

Typically, constant-charge DFT calculations lead to a change in the electrode Fermi energy between the reactant and product of redox processes associated with PCET. This change in the Fermi energy is also related to the computational work function or electrode potential. In the example of the Heyrovsky PCET reaction on Pt(111) shown in Figure 17, the change in work

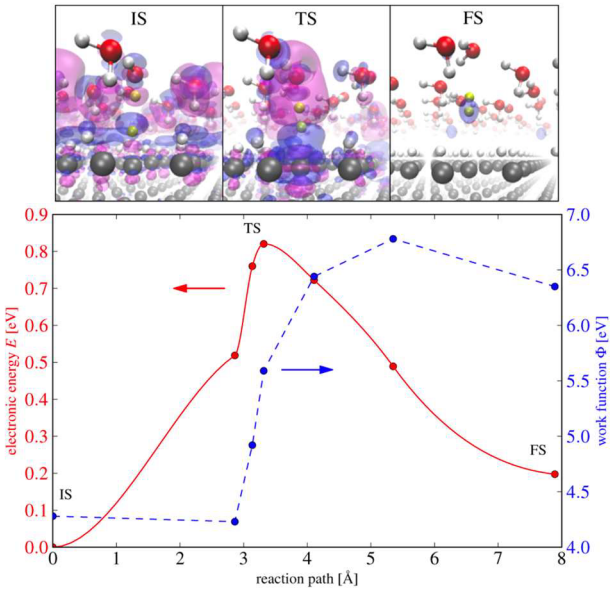

Figure 17. Constant charge calculation to determine the Heyrovsky reaction barrier on Pt(111) using a 3 × 4 unit cell. The top panel shows the charge density difference isosurfaces for the initial state (IS), transition state (TS), and final state (FS) of the reaction. The isosurfaces are referenced to the FS, where the magenta and blue surfaces correspond to negative charge accumulation and depletion, respectively. The bottom panel shows the electronic energy profile (in red) and the work function (in blue) for different images along the minimum energy path. Reproduced with permission from ref 172. Copyright 2015 American Chemical Society.

function can be on the order of several electron volts between reactants and products.[172] The sensitivity of calculated activation energies to the applied potential has been recognized in many computational heterogeneous electrocatalysis studies, and various computational methods have been developed to address this issue.

In the H-shuttling model,[173] the transition state of a water-assisted surface hydrogenation reaction is assumed to be similar to that of the analogous PCET reaction. This approach was introduced in the analysis of the kinetics of elementary steps in CO_2 electroreduction, as shown by the transition state geometries for CO* and CH_3O* reduction in Figure 18.[173]

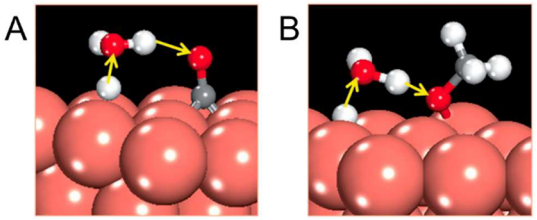

Figure 18. DFT calculations of C−H bond formation barriers in CO_2 electroreduction pathways on Cu(111) using a water-assisted H-shuttling model. Transition states for (A) CO* reduction to COH* and (B) CH_3O* reduction to CH_3OH*. The transition states identified for water-mediated hydrogenation reactions are hypothesized to be similar to those of electrochemical PCET steps. Figure reproduced with permission from ref 173. Copyright 2013 Wiley-VCH.

The main advantage of this approach is that by modeling PCET as a hydrogenation process that does not involve ET from the electrode, the change in work function between the reactants and the transition state is small, and the calculated activation energy is expected to be similar to that of a constant-potential PCET process. These methods were used to evaluate potential-dependent barriers for O−H and C−H bond forming PCET steps, as well as C−C bond coupling in CO_2 electroreduction on Cu(111).[173] This study demonstrated that analysis of the competing pathways in CO_2 reduction using reaction free energies can be deceptive. In particular, an analysis of the kinetics of the elementary steps revealed the importance of an adsorbed COH* intermediate in the selectivity-determining steps between methane and methanol. These H-shuttling methods have proved to be useful in identifying transition states for heterogeneous PCET processes on metal surfaces for NO reduction[174−176] as well as CO_2 reduction.[173,177,178]

Cell-size extrapolation techniques have also been used to compute activation barriers at constant potential. An analysis of the Heyrovsky reaction on Pt(111) elucidated the impact of finite unit cell size on calculated reaction free energies and activation energies.[104] Because the free energy of the electrochemical interface corresponds to the energy stored in a capacitor formed between the electrode and protons in the EDL (see subsection 2.4), the transition state energy is expected to depend on the size of the unit cell. Figure 19A shows linear scaling of activation energies with the change in the computational electrode potential between reactants and products for various unit cell sizes and hydrogen surface coverages. Note that the computational electrode potential can be determined from the computed work function given in eq 4. These results may be extrapolated to the limit where the electrode potential is constant (i.e., the same for reactants and products) to determine the electrochemical PCET barriers at constant potential.[104] Note that maintaining a constant transition state geometry at different unit cell sizes may not be accurate because the computational electrode potential is different in each calculation. However, reoptimization of transition state geometries at different unit cell sizes can significantly add to the computational expense of activation energy calculations.

The cell-extrapolation approach was also used to evaluate the relationship between computed reaction energies and activation energies for the Heyrovsky reaction on Pt(111).[100] The linear relationship between these two quantities, shown in Figure 20A, is representative of the typical dependence of the electrochemical PCET barrier on overpotential, which is related to the transfer coefficient β in Butler−Volmer kinetics.[17] While

https://doi.org/10.1021/acs.chemrev.1c00929
Chem. Rev. XXXX, XXX, XXX−XXX

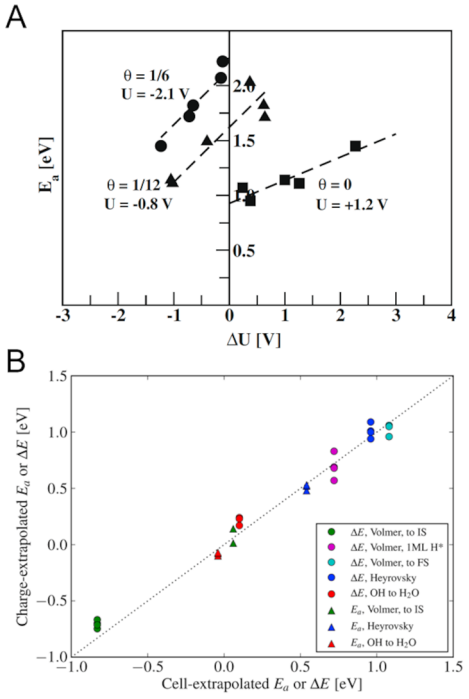

Figure 19. (A) Cell-extrapolated activation energies (E_a) as a function of the change in computational electrode potential (ΔU) between the reactants and products for the Heyrovsky reaction, $H^* + H^+ + e^- \rightarrow H_2$, on Pt(111). Different data points correspond to different unit cell sizes. Different marker types and linear fits correspond to calculations performed at different adsorbed hydrogen coverages (Θ). The extrapolation to $\Delta U = 0$ corresponds to the activation energy of the PCET reaction at constant electrode potential. Figure reproduced with permission from ref 104. Copyright 2008 Elsevier. (B) Parity plot comparing reaction energies and activation energies obtained using the charge-extrapolation model (eq 15) and the cell-extrapolation model for various electrochemical reactions on Pt(111). Panel reproduced with permission from ref 172. Copyright 2015 American Chemical Society.

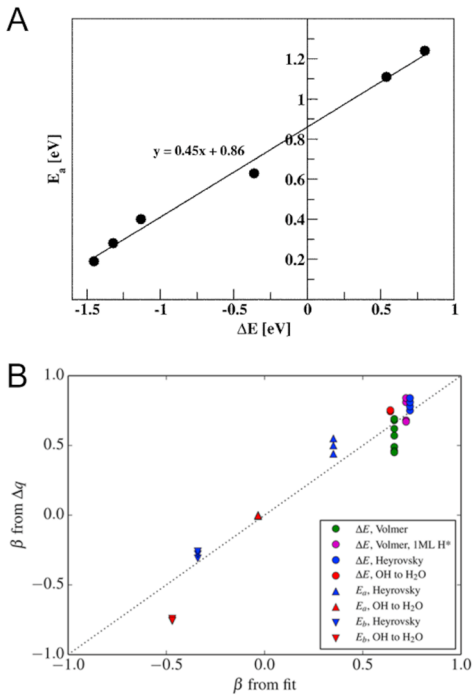

Figure 20. (A) Brønsted–Evans–Polanyi relationship between activation energy (E_a) and reaction energy (ΔE) for the Heyrovsky reaction on Pt(111). Reproduced from ref 100 with permission from the PCCP Owner Societies. Copyright 2007 Royal Society of Chemistry. (B) Parity plot between Butler–Volmer transfer coefficient β determined from a linear fit of reaction energies and activation energies vs work function (horizontal axis), and β determined from Bader charge analysis (vertical axis). Reproduced with permission from ref 180. Copyright 2016 American Chemical Society.

previous computational studies had established the existence of Brønsted–Evans–Polanyi relationships for thermal (de)-hydrogenation reactions on metal surfaces,[179] this later study provided computational support for these linear Brønsted–Evans–Polanyi relations in heterogeneous electrochemical PCET and established their relationship to Butler–Volmer transfer coefficients.

In the charge-extrapolation approach developed by Chan and Nørskov, a single barrier calculation is used to estimate activation energies at constant potential by separating the chemical and electrostatic contributions to the change in energy of a PCET process at an electrochemical interface.[172] Separating the chemical and electrostatic (capacitive) contributions to the total energy leads to the following expression for the difference in energy between states 1 and 2 (corresponding to the initial state, transition state, or final state) at a constant applied potential:

$$\Delta U(\Phi_1) = U_2(\Phi_2) - U_1(\Phi_1) + \frac{(q_2 - q_1)(\Phi_2 - \Phi_1)}{2}$$

$$\Delta U(\Phi_2) = U_2(\Phi_2) - U_1(\Phi_1) - \frac{(q_2 - q_1)(\Phi_2 - \Phi_1)}{2} \quad (15)$$

Here, Φ_i is the work function, and q_i is the net charge of the slab and any surface adsorbates for state i. The q_i terms in eq 15 can be determined from DFT calculations using population analysis techniques, such as Bader charges. This expression was used to calculate activation energies and reaction energies, where this charge-extrapolation model[172] gave similar results as the cell-extrapolation model (Figure 19B).[104,181] The charge-extrapolation model mitigates the need to perform multiple DFT calculations at varying unit cell sizes to determine reaction energies and activation energies.

In an extension of the charge-extrapolation model, Chan and Nørskov showed that evaluation of eq 15 at two different applied potentials between the initial state (state 1) and the transition state (state 2) yields a general expression for constant-potential activation energies E_a.[180] The resulting expression is

$$E_a(\Phi) = E_a(\Phi_{ref}) - \Delta q(\Phi - \Phi_{ref}) \quad (16)$$

where Φ_{ref} corresponds to a reference work function and Δq is the difference in net charge of states 2 and 1. Note that the reaction energy may also be substituted for E_a in eq 16. In this model, Δq is related to the transfer coefficient β in Butler–Volmer kinetics by $\Delta q = -\beta$. For transition state calculations, this β corresponds to the partial charge transfer at the transition state.[180] Using eq 16, the value of β was estimated by linear fits of reaction energies and activation energies versus work functions, demonstrating reasonable agreement with β values determined from Δq calculations using Bader analysis (Figure 20B). Janik and co-workers,[182,183] as well as Greeley and co-workers,[184] later expanded on these insights, unifying Brønsted–Evans–Polanyi

https://doi.org/10.1021/acs.chemrev.1c00929
Chem. Rev. XXXX, XXX, XXX–XXX

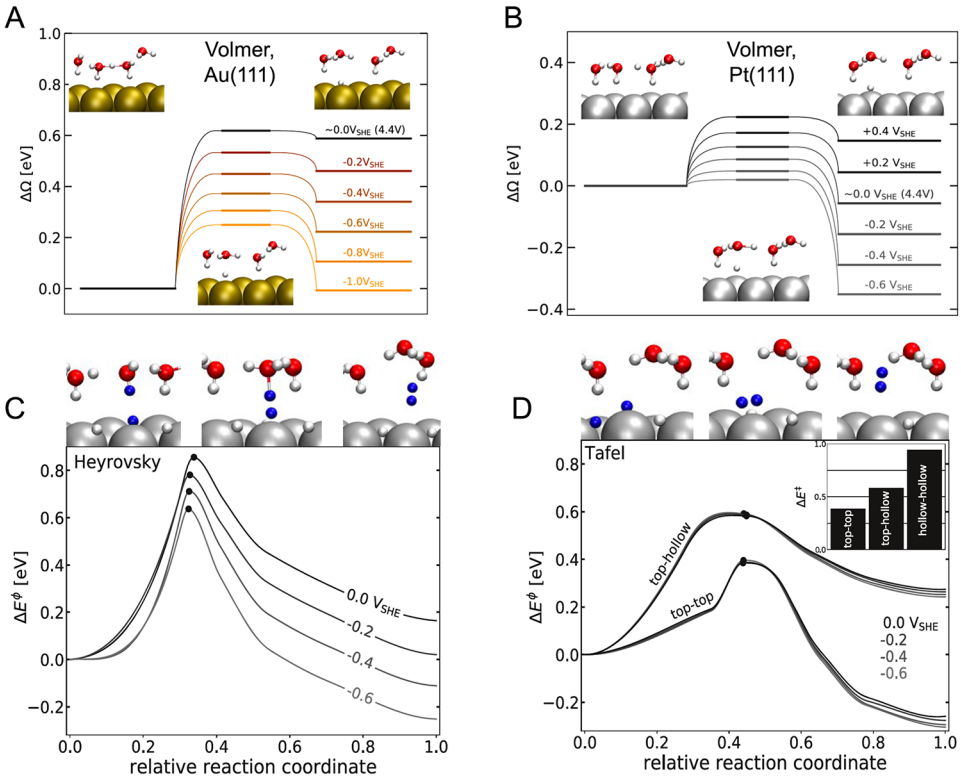

Figure 21. Grand potential free energies relative to the initial state for different steps in the HER as a function of applied potential. (A) Volmer reaction on Au(111), (B) Volmer reaction on Pt(111), (C) Heyrovsky step on Pt(111), and (D) Tafel step on Pt(111). The barriers for the Tafel step are shown for different permutations of adsorbed H* on top and hollow surface sites. The insets in each figure correspond to the initial state, transition state, and final state geometries. The Volmer and Heyrovsky barriers are sensitive to the applied potential because they are electrochemical PCET reactions, whereas the Tafel step does not exhibit this sensitivity because it is a nonelectrochemical combination of surface H atoms to form solvated H_2. Note that the notation for grand potential free energy shown on the *y*-axes differs for A and B versus C and D. Panels A and B are reproduced with permission from ref 111. Copyright 2018 American Chemical Society. Panels C and D are reproduced with permission from ref 112. Copyright 2020 American Chemical Society.

relationships for (de)hydrogenation reactions with Butler–Volmer transfer coefficients for potential-dependent interfacial PCET. Overall, these studies elucidate relationships between Brønsted–Evans–Polanyi slopes, the character of the transition state geometry (i.e., early, initial state-like or late, final state-like), and Butler–Volmer transfer coefficients.

Another approach that has been used to obtain potential-dependent activation energies is to directly control the electrode Fermi level in the electronic structure calculations using constant-potential (or grand canonical) DFT methods. Peterson and co-workers calculated PCET activation barriers by varying the number of electrons in the unit cell along with a neutralizing countercharge in dielectric continuum solvent.[111] This approach, termed the "solvated jellium" (SJ) method, was used to compute barriers for proton discharge from H_3O^+ during the acidic Volmer reaction on Au(111) and Pt(111) as a function of applied potential from the saddle point of the constant-potential MEP using the climbing image NEB method (Figure 21A,B). The results demonstrated that Pt is a better HER catalyst than Au not only from the standpoint of thermodynamics predicted by the CHE model[63] but also because there is a lower kinetic barrier when the Volmer reaction is thermoneutral; i.e., the barrier is greater than 0.2 eV on Au(111) at −1.0 V (Figure 21A) and less than 0.2 eV on Pt(111) at 0 V (Figure 21B).[111] These SJ methods were subsequently extended to the Heyrovsky and Tafel steps in the HER mechanism on Pt(111). In these steps, the Heyrovsky PCET step exhibits potential-dependent barriers (Figure 21C), whereas the Tafel step ($2H^* \rightarrow H_2 + 2^*$) is largely independent of potential (Figure 21D) because there is no formal charge transfer during the Tafel step.[112]

Interestingly, this work based on the SJ method showed that the potential-dependent relationship between the reaction energy ΔU and the activation energy E_a can be treated using a single parameter b for a given reaction according to the following expression:

$$E_a = \begin{cases} 0, & \Delta U < -4b \\ \dfrac{(\Delta U + 4b)^2}{16b} & -4b \le \Delta U \le 4b \\ \Delta U & \Delta U > 4b \end{cases} \quad (17)$$

This expression is based on the model of two intersecting parabolas in Marcus theory[185] with the reorganization energy $\lambda = 4b$, where the inverted region is treated as activationless. This model adds complexity to established Brønsted–Evans–Polanyi relations. Moreover, it smoothly interpolates from conditions of intermediate reaction energies to conditions where the barrier vanishes for very exothermic or endothermic reactions, and E_a is approximately equal to zero or the reaction energy, respectively. A variety of other constant-potential approaches have been used to evaluate PCET barriers in mechanistic analyses of hydrogen

https://doi.org/10.1021/acs.chemrev.1c00929
Chem. Rev. XXXX, XXX, XXX–XXX

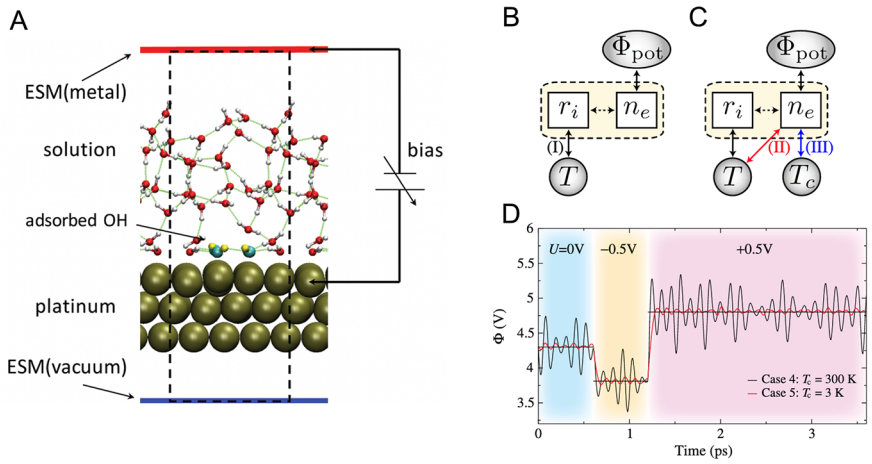

Figure 22. (A) Computational unit cell using the effective screening medium (ESM) method to perform AIMD simulations of charged metal−water interfaces. Excess charge on the atomic system is compensated by a counter-charge within the semi-infinite medium, depicted in red, which has an infinite dielectric constant and screens the periodic boundary conditions in the direction of the surface normal. Reproduced from ref 205 with permission from the PCCP Owner Societies. Copyright 2017 Royal Society of Chemistry. (B−C) Temperature and potential control schemes in constant potential AIMD. In (B), the charge is not connected directly to the thermostat, whereas it is connected to the thermostat in (C). The system is contained within the dashed boxes, and r_i and n_e are the particle and charge degrees of freedom, respectively. (D) Electrode potential over the duration of a constant potential AIMD run, where the thermostat connected to n_e with different temperatures T_c can tune the oscillations of the calculated potential. Panels B−D reproduced with permission from ref 201. Copyright 2012 American Physical Society.

evolution,[45,186,187] CO_2 reduction,[188,189] and formic acid oxidation.[190]

3.3. Interfacial Dynamics of PCET

The previous subsections outlined methods and applications to evaluate potential energy surfaces and activation barriers for electrochemical PCET using periodic DFT calculations. However, these methods do not directly include entropic effects and do not capture the dynamics of the redox species, proton donors and acceptors, solvent molecules, and ions at the electrochemical interface during PCET reactions. Although implicit solvent models can alleviate the need for statistical sampling of the solvent, they do not explicitly model hydrogen bonding interactions that involve solvent molecules. This subsection summarizes *ab initio* molecular dynamics (AIMD) methods and applications to electrochemical interfaces. In particular, we focus on methods that relate to modeling PCET at these interfaces, including constant-potential and rare event sampling methods.

Free energy barriers can be evaluated by sampling the free energy surfaces using methods such as metadynamics[191] or constrained MD.[192] Each of these methods relies on the choice of collective variables used to represent the free energy landscape. In metadynamics, the free energy surface is sampled over the chosen collective variables, and Gaussian potentials are added to accelerate the sampling of regions that are higher in free energy. In constrained MD, integration of the potential of mean force[192,193] at each value of the collective variable can be used to generate the free energy surface and barrier along the reaction coordinate. In analyses of heterogeneous PCET, these collective variables are typically defined by the bond being broken or formed in the reaction. For example, Blue Moon ensemble constrained MD calculations constrained O−H and C−H bond lengths for CH_3OH dehydrogenation to OCH_3 and CH_2OH, respectively.[194] Similar bond lengths were used as the collective variables in metadynamics simulations of PCET steps in CO_2 reduction,[195,196] although more complex collective variables defined by the collective modes of a hydrogen-bonding network involved in Eley−Rideal PCET processes have also been used.[197] Constrained MD has also been used to evaluate the reaction free energy landscapes of the Volmer and Tafel steps of HER.[198] These calculations also included *a posteriori* effects of the applied potential using the capacitive charge-extrapolation scheme described in subsection 3.2.

The computational electrode potential can be modified in MD simulations by carrying out AIMD studies with excess charge,[105] building upon calculations of charged slabs with periodic boundary conditions.[93] In this approach, termed the "effective screening medium" (ESM) or "fictitious charged particle" method, the excess charge is compensated within a fictitious slab of infinite dielectric in the vacuum region between periodic images of the slab (Figure 22A). These methods were used in studies of the orientation of water molecules near charged metal electrode surfaces.[199,200]

The ESM approach was later adapted to constant Fermi level AIMD (Figure 22B−D).[201] In this method, the system exchanges electrons with an external reservoir to maintain constant potential, representing a potentiostat, while simultaneously maintaining constant temperature with a thermostat (Figure 22B−C). This type of approach is necessary to maintain a constant electrode potential at solid−liquid interfaces because for a given charge, the potential can vary on the order of a volt based on the orientation of polar solvent molecules near the interface. In this constant Fermi level AIMD approach, charge thermalization can be achieved through the Nosé−Hoover thermostat connected to the particle degrees of freedom r_i, based on the coupling between r_i and the charge degrees of freedom n_e (Figure 22B). Because this coupling is generally weak, equilibration can be accelerated by connecting n_e to its own thermostat with temperature T_c. Provided there is weak coupling between r_i and n_e, it is not necessary that $T_c = T$, and the system approaches a quasi-equilibrium defined by these two temperatures. The utility of decoupling the two thermostats is that a smaller T_c reduces fluctuations in the potentiostat (Figure 22D). Similar constant Fermi level AIMD methods were developed[202]

https://doi.org/10.1021/acs.chemrev.1c00929
Chem. Rev. XXXX, XXX, XXX−XXX

and applied to evaluate solvation energies of PCET intermediates in the OER reaction mechanism on Pt(111).[203]

In another approach beyond maintaining a constant Fermi level, constant inner potential methods have been applied to constant electrode potential DFT and AIMD calculations.[72] Rather than maintaining a constant Fermi level, these methods modulate the inner potential of the electrode bulk, which is more closely related to the relevant electrochemical potential that is controlled by the potentiostat in experiments. This distinction becomes most important for systems such as semiconductors and outer-sphere redox species that are weakly coupled to the electrode surface.[72,204]

AIMD simulations of charged interfaces enable the modeling of the dynamics of potential-dependent PCET processes. By introducing excess charge at the aqueous Pt(111) interface, proton discharge from H_3O^+ in conjunction with the reorientation of interfacial water in response to proton transfer was observed (Figure 23A,B).[106] Figure 23C shows a snapshot from the Blue Moon ensemble constrained MD simulations that were performed in conjunction with the ESM method to maintain constant potential in a mechanistic study of hydrogen evolution by a 4,4′-bipyridine (BiPy) molecular catalyst adsorbed on Ag(111).[206] Because of the large change in the Fermi level between the reactant and transition state, a high activation energy of 0.9 eV was estimated from constant-charge dynamical simulations of the PCET step converting BiPy-H$^\bullet$ to BiPy-H_2. However, the calculated barrier was reduced to ∼0.7 eV for the constant-potential ESM simulations (Figure 23D) because the excess charge supplied to the unit cell reduced the transition state energy. Similar methods were applied to the PCET steps in ORR on Pt(111), where performing the simulations using different Fermi levels enabled the calculation of activation energies and symmetry parameters in Butler−Volmer equations.[205]

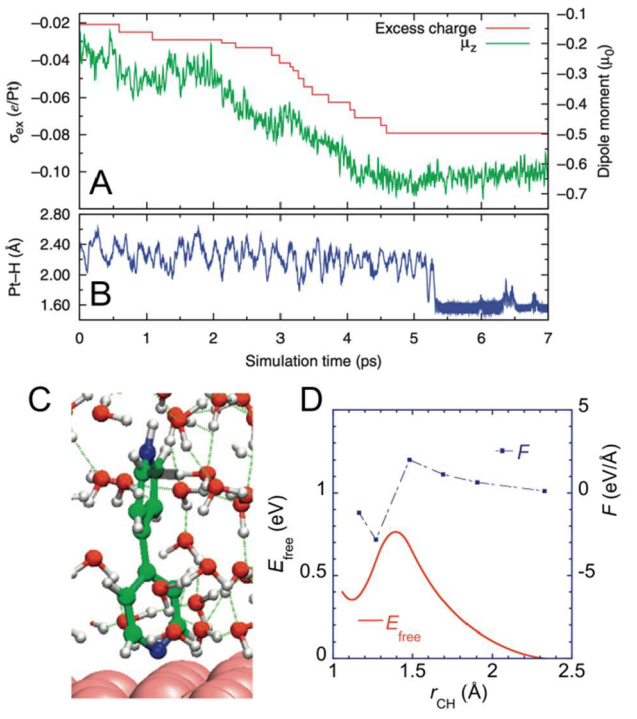

Figure 23. (A) Excess charge density σ_{ex} and average water dipole moment μ_z over the time of an AIMD simulation of the aqueous Pt(111) interface where charge is modified as an input. (B) The minimum Pt−H distance over the duration of the AIMD trajectory in (A). Panels A and B are reproduced with permission from ref 106. Copyright 2008 Physical Society of Japan. (C) AIMD snapshot near the transition state, r_{CH} = 1.5 Å, for the PCET reaction converting BiPy-H$^\bullet$ to BiPy-H_2. C, O, H, N, and Ag atoms are represented by green, red, white, blue, and pink, respectively. The gray line indicates the constrained CH bond in the Blue Moon ensemble constrained MD simulation. (D) Free energy and forces between constrained atoms for the reaction in (C). Panels C and D are reproduced with permission from ref 206. Copyright 2017 Elsevier.

Recently, constant potential AIMD methods have been combined with slow-growth constrained MD into a "constant-potential hybrid-solvation dynamic model" to analyze hydrogen peroxide formation mechanisms in ORR.[207] Although these studies were only used to analyze constant-potential O−O bond cleavage in electrocatalysis, the application of such methods that combine constant-potential dynamics and rare-event sampling is very promising for PCET studies. Moreover, even though many of the constrained MD studies described in this subsection utilized atomic distances as the reaction coordinates, more representative reaction coordinates could be used for PCET reactions,[11] such as those related to the collective bonds of the hydrogen-bonding network at the interface.[197]

4. CHARACTERIZING THE REACTION ENVIRONMENT IN THE ELECTRIC DOUBLE LAYER

The EDL, which is composed of solvent and ions at the electrode interface, could significantly impact electrochemical PCET reactions. Thus, understanding the structure and dynamics of the EDL is essential for a proper description of interfacial PCET. This field has received considerable attention, and here we only touch upon a few of the models and computational studies used to characterize the EDL. We start with a discussion of multilayer dielectric continuum models and then discuss simulations of the EDL with explicit solvent and ions. The last subsection discusses computational methods that have been used to compute spectroscopic properties, such as vibrational frequencies of probe molecules, for comparison to experiments investigating PCET at electrode interfaces. This section should not be viewed as comprehensive but rather should be viewed as providing representative examples. Other reviews have covered this topic more comprehensively.[208]

4.1. Dielectric Continuum Models of the EDL

The Gouy−Chapman−Stern model[209−212] has been used to describe the EDL in a mean-field manner. This model includes the inner Helmholtz layer (IHL), the outer Helmholtz layer (OHL), and the diffuse layer, as depicted in Figure 24. The IHL is composed of partially oriented solvent molecules and specifically adsorbed molecules, with a width typically determined by the diameter of a solvent molecule. The IHL is expected to have a low dielectric constant, often assumed to be the square of the refractive index of the solvent. The OHL is defined as the region between the exterior plane of the IHL and a plane passing through the center of the solvated counterions closest to the electrode. The dielectric constant of the OHL is expected to depend on the applied potential. The diffuse layer extends from the external plane of the OHL to bulk solution and is typically assumed to have the same dielectric constant as the bulk solvent.

An extended Gouy−Chapman−Stern model based on the generalized Stern model with spatial variation of permittivity[213−215] has been used in the context of electrochemical

https://doi.org/10.1021/acs.chemrev.1c00929
Chem. Rev. XXXX, XXX, XXX−XXX

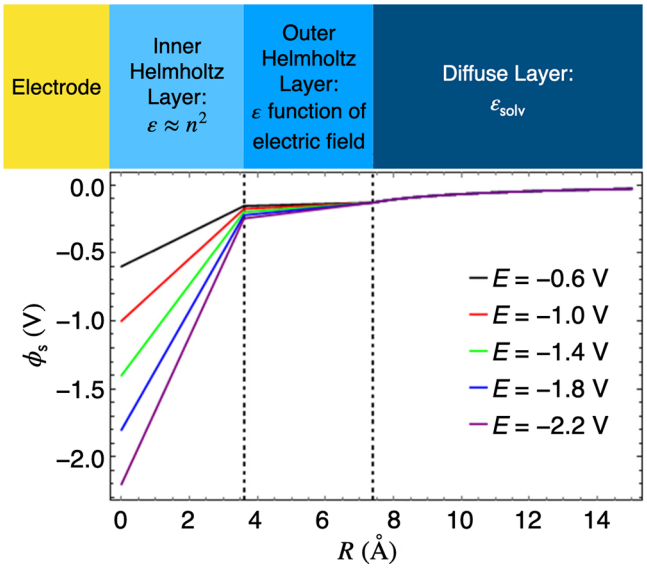

Figure 24. Schematic depiction of an extended Gouy−Chapman−Stern model of the EDL. The dielectric constants in the inner Helmholtz layer and diffuse layer are the square of the refractive index n and the solvent dielectric constant ε_{solv}, respectively, and the dielectric constant in the outer Helmholtz layer is a function of the electric field. The lower portion of this figure shows the electrostatic potential as a function of distance R from the electrode for various applied potentials relative to the potential of zero charge. Figure adapted with permission from ref 216. Copyright 2018 American Chemical Society.

PCET.[216] In this model, the Laplace and Langevin−Poisson−Boltzmann equations with appropriate boundary conditions are solved self-consistently to determine the dielectric constant in the OHL as a function of the magnitude of the electric field in this region. As shown in Figure 24, the electrostatic potential increases (or decreases) linearly in the IHL and OHL, with the majority of the increase (or decrease) occurring in the IHL because of the low dielectric constant in this region. As described in sections 5 and 6, the electrostatic potential obtained from this type of model can be added to the driving force when computing rate constants for electrochemical PCET reactions.

Continuum representations of the EDL entail self-consistent solutions to the electronic structure problem of the electrode with a Poisson or Poisson−Boltzmann theory treatment of the continuum solvent.[105,217−219] These calculations often involve interfacial switching functions[220,221] and solute cavity definitions based on solute electron density[222] as well as nonlocal solvent-aware treatments.[223] Other treatments account directly for the nuclear density over liquid solvents using classical density functionals.[123,224−226] Through an interaction functional between the solute and solvent, joint density functional theory enables a description of nonlinear fluid responses at solid−liquid interfaces[122,227,228] and can reproduce interfacial electrostatic profiles consistent with the Gouy−Chapman−Stern theory from first principles.[122]

4.2. Simulation of the EDL with Explicit Solvent and Ions

The structure and dynamics of ions and solvent in the EDL have been examined in various classical and first-principles MD studies. In particular, AIMD-based methods have been useful in estimating the potential of zero charge (PZC) of metals[106,229−232] and alignment of redox levels of semiconductors.[71,233] Dynamical sampling is needed to estimate these properties because the calculated electrode potential can vary widely based on the EDL structure, especially the orientation of solvent molecules near the surface. From these simulations, alignment schemes[234,235] can be used to reference computed PZCs and band levels to the SHE. AIMD simulations have provided key insights into the water structure and double layer reorganization near metal[236−239] and semiconductor[71,103,240] surfaces, as well as the differential capacitance in the EDL.[241] Pertaining directly to electrocatalysis, sampling of explicit solvent configurations has aided in the prediction of solvation energies of adsorbed intermediates.[174,194] While AIMD simulations are limited in terms of the system size and sampling time, machine learning methods can use data from equilibrated AIMD runs to parametrize force fields for classical simulations with improved statistics.[242]

Classical MD simulations performed with molecular mechanical force fields have implemented electrode and electrolyte boundary conditions to describe the electrochemical interface.[243−245] The augmentation of such methods to include potential bias has been shown to reproduce the characteristic double-layer structure of the electrochemical electrode−electrolyte interface.[246,247] However, the structure of interfacial water in classical simulations can be sensitive to the hydrophilicity of the electrode surface.[248] Classical MD simulations have also helped establish the role of spectator cations on solvation of redox molecules in the EDL, which in turn impacts outer-sphere ET rates.[249] Reactive force fields parametrized from QM calculations (i.e., ReaxFF) can provide additional insights into chemical bonding at solid−liquid interfaces.[250,251] For example, the RexPoN reactive force field was recently used to describe interfacial long-range polarization effects and combined with machine learning methods to describe the structure and reactivity of the electrode−electrolyte interface in the proximity of different types of surface sites on realistic Au nanoparticle catalysts.[252] Combining such approaches enables the description of the EDL using simulations with thousands of atoms, beyond that which could be probed using *ab initio* methods.

4.3. Computing Spectroscopic Observables to Characterize the EDL

Computational chemistry methods have been useful in describing the PCET reaction environment within the EDL through direct comparison with *in situ* or *operando* experimental measurements. For example, α-Al_2O_3/water interfaces have been characterized through direct comparison of measured and simulated interfacial X-ray reflectivity patterns, providing a protocol to validate theoretical modeling approaches for solid−liquid interfaces.[253] In another study, periodic DFT and AIMD calculations of adsorbed OH in both hydrated and nonhydrated environments on Pt(111) showed that hydrated OH adsorbates most likely dominate under ORR conditions, despite previous X-ray photoelectron spectroscopy studies suggesting that adsorbed OH is not hydrated.[254] The interfacial structures discerned from these joint computational and experimental studies help establish the interfacial PCET reaction environment within the EDL with molecular-level precision.

Beyond X-ray characterization techniques, vibrational spectroscopy has been useful in the description of the reaction environment for PCET in electrochemical systems. Inspired in part by studies of enzyme catalysis,[255,256] vibrational probes can be used to measure the local electric field in the EDL.[257−261] To a first-order approximation, the change in the local electric field ΔF can be inferred from the change in the probe vibrational frequency $\Delta\nu$ using the linear Stark equation:

https://doi.org/10.1021/acs.chemrev.1c00929
Chem. Rev. XXXX, XXX, XXX−XXX

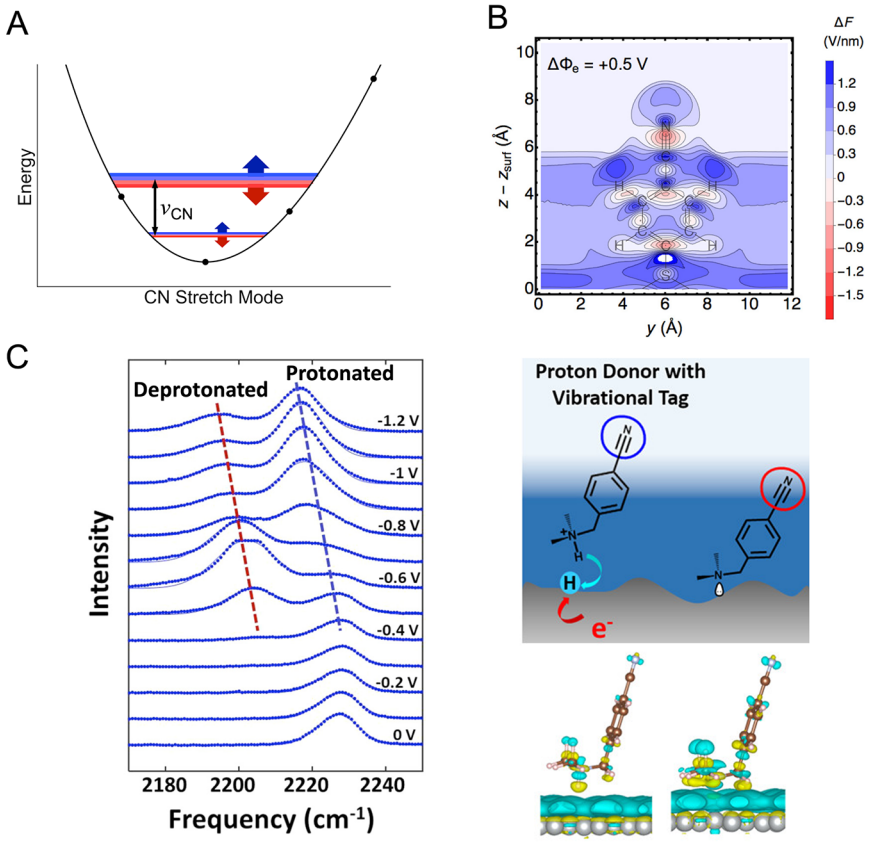

Figure 25. (A) Schematic of the grid-based approach used to calculate the energy splitting between the lowest two vibrational states of a CN vibrational probe, where the Fourier grid Hamiltonian method is used to solve the one-dimensional Schrödinger equation on the potential energy curve along the CN normal mode. (B) Surface-normal electric fields relative to the field at PZC in the *yz* plane across 4-MBN adsorbed on Au(111). Panels A and B adapted with permission from ref 262. Copyright 2020 American Chemical Society. (C) Upper right: a schematic of the Volmer reaction using a tertiary ammonium proton donor attached to a benzonitrile vibrational probe. Lower right: Periodic DFT calculations showing physisorption of the protonated molecule and chemisorption of the deprotonated molecule. Left: surface-enhanced Raman spectra as a function of applied potential, with the blue and red dashed lines indicating the peaks assigned to the protonated and deprotonated molecule, respectively. Periodic DFT calculations using the grid-based approach depicted in panel A were used to interpret these spectra in terms of different stages of the Volmer reaction. Panel reproduced with permission from ref 265. Copyright 2021 American Chemical Society.

$$h\Delta\nu = \Delta\mu\cdot\Delta F \tag{18}$$

where h is Planck's constant and $\Delta\mu$ is the Stark tuning rate. However, this linear relationship does not always hold at electrochemical interfaces due to the complexity of the EDL.

Periodic DFT in dielectric continuum solvent has been used to calculate potential-dependent vibrational frequencies of 4-mercaptobenzonitrile (4-MBN) adsorbed on Au(111).[262] The electrode potential was altered in these calculations by varying the number of electrons in the unit cell, and the CN vibrational frequencies of the nitrile probe were calculated for different applied electrode potentials using a grid-based approach that accounts for anharmonicity. In this approach, a potential energy curve is computed by performing single-point energy calculations on a grid along the CN vibrational mode, and the Fourier grid Hamiltonian method[263,264] is used to compute the energy splitting between the lowest two vibrational states (Figure 25A). The calculated shifts in nitrile frequencies using this approach exhibited close agreement with experiments by the Dawlaty group.[257,258] Interestingly, the interfacial electric fields across the 4-MBN molecule (i.e., the first-derivative of the electrostatic potential) showed significant spatial inhomogeneity (Figure 25B),[262] implying atomic-level complexity of the relationship between the nitrile stretch frequency and the applied potential extending beyond the linear Stark equation given in eq 18. These calculations demonstrate the limitations of the linear Stark equation and mean-field models such as the Gouy−Chapman−Stern model described above.

Another study used the aforementioned grid-based approach to compute potential-dependent CN vibrational frequency shifts for 4-[(dimethylammonium)methyl], a benzonitrile probe attached to a tertiary ammonium proton donor that undergoes the Volmer reaction at a silver electrode (Figure 25C).[265] This computational study assisted in the interpretation of *operando* surface-enhanced Raman spectroscopy measurements that monitored the interfacial PCET process corresponding to proton donation to the electrode. In particular, the calculations showed that the nitrile frequencies shift based on the protonation state of the molecule as well as when the molecule enters the EDL. These findings elucidated key stages of the nonaqueous Volmer reaction involving the entry of the proton donor into the EDL, the formation of a stationary product layer on the electrode surface, and the generation of steady-state current. These studies demonstrate the important interplay between interfacial electrostatics and PCET and illustrate how theory and experiment can gauge the impact of interfacial electric fields in the reaction environment.

https://doi.org/10.1021/acs.chemrev.1c00929
Chem. Rev. XXXX, XXX, XXX−XXX

5. THEORY OF HOMOGENEOUS ELECTROCHEMICAL PCET

The fundamental concepts underlying PCET are related to Marcus theory for electron transfer[19−23] and extensions by Hynes and co-workers to proton transfer.[266−271] Subsequently, Marcus theory for electron transfer was extended to describe PCET by treating the proton transfer coordinate as an inner-sphere solute mode.[272−275] A more general, comprehensive theory for homogeneous PCET in solution, proteins, and electrochemical systems was developed by Soudackov and Hammes-Schiffer.[1,24−27,30] The relationship between these various theories has been discussed elsewhere,[26] but to retain coherence, this section focuses mainly on the more general formulation. Homogeneous electrochemical PCET, in which the electrode does not participate directly in the chemical bond breaking and forming associated with proton transfer, is discussed in this section, and heterogeneous electrochemical PCET will be discussed in the next section.

5.1. Fundamental Theoretical Concepts

A general theory for homogeneous PCET in solution and proteins has been developed by Soudackov and Hammes-Schiffer.[24−27,30] In this theory, a PCET reaction involving one electron and one proton is described in terms of four diabatic electronic states associated with the electron and proton both localized on either their donors or their acceptors or one localized on its donor with the other localized on its acceptor (Figure 26). This formalism can describe both sequential and

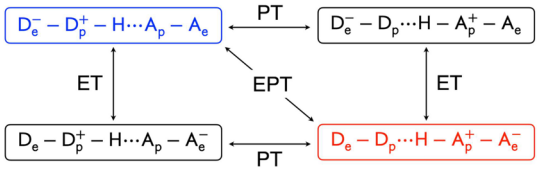

Figure 26. Four diabatic electronic states used to describe a PCET reaction involving one electron and one proton. The sequential mechanism corresponds to moving along the outer edges of the rectangle, either ET−PT or PT−ET. The concerted mechanism corresponds to moving along the diagonal, indicated as EPT. These diabatic states serve as the basis for the multistate continuum theory developed for PCET and used to derive analytical rate constant expressions.

concerted PCET mechanisms, depending on the relative energies and couplings among these four states. The sequential mechanism corresponds to moving around the edges of the rectangle, either ET−PT or PT−ET, whereas the concerted mechanism corresponds to moving along the diagonal, denoted EPT. The concerted mechanism can be described in terms of two states corresponding to the electron localized on its donor or acceptor, designated the reactant and product, respectively.

In this PCET theory, the transferring hydrogen nucleus is treated quantum mechanically, and the proton vibrational states are computed for the reactant and product electronic states. This procedure leads to a set of reactant and product electron−proton vibronic states, where each vibronic state is the product of an electronic state and an associated proton vibrational state. Specifically, if the reactant (initial) and product (final) electronic states are denoted $|\psi_i\rangle$ and $|\psi_f\rangle$, and the corresponding proton vibrational states are denoted $|\chi_\mu^{(i)}\rangle$ and $|\chi_\nu^{(f)}\rangle$, the reactant and product vibronic states are given by the direct products $|\psi_f\rangle|\chi_\mu^{(i)}\rangle$ and $|\psi_f\rangle|\chi_\nu^{(f)}\rangle$, respectively.

A multistate continuum theory[24,276] was used to derive expressions for the free energies of these vibronic states as functions of two collective solvent coordinates corresponding to ET and PT, respectively, as depicted in Figure 27A. Under certain well-defined approximations,[25,26] the PCET reaction can be described in terms of the one-dimensional parabolas connecting the minima of these two-dimensional free energy surfaces (Figure 27B). These parabolic free energy curves along a collective solvent coordinate are analogous to the electronic curves in Marcus theory for electron transfer[19,20,277] and the proton vibrational curves in subsequent theories by Hynes and co-workers and others for proton transfer.[266−268,278−281] In the case of PCET, these curves correspond to the reactant and product electron−proton vibronic states.[24,26] More generally, this theoretical formulation produces two sets of stacked paraboloids, or parabolas for a one-dimensional slice, corresponding to the different proton vibrational states for each electronic state (see lighter blue and red parabolas in Figure 27B). Note that the splittings between the parabolas correspond to the splittings between the proton vibrational energy levels. In the vibronically adiabatic regime, PCET reactions are described in terms of motion on the adiabatic ground vibronic state using a framework such as transition state theory. In the vibronically nonadiabatic regime, PCET reactions are described in terms of nonadiabatic transitions between pairs of reactant and product vibronic states.

To describe vibronically nonadiabatic PCET, Fermi's golden rule was used to derive rate constant expressions in various well-defined regimes. For a fixed proton donor−acceptor distance R, the vibronically nonadiabatic PCET rate constant is[26]

$$k = \sum_\mu P_\mu \sum_\nu \frac{|V_{\mu\nu}|^2}{\hbar}\sqrt{\frac{\pi}{\lambda k_B T}}\exp\left[-\frac{(\Delta G^\circ_{\mu\nu}+\lambda)^2}{4\lambda k_B T}\right] \quad (19)$$

where the summations are over reactant and product vibronic states, P_μ is the Boltzmann population of reactant state μ, $V_{\mu\nu}$ is the vibronic coupling between reactant and product vibronic states μ and ν, λ is the reorganization energy, and $\Delta G^\circ_{\mu\nu}$ is the free energy of reaction for states μ and ν (Figure 27B). The vibronically nonadiabatic rate constant is applicable when the vibronic coupling is much less than the thermal energy, in conjunction with fast solvent relaxation and other conditions.[26,282]

The form of the vibronic coupling depends on the electron−proton nonadiabaticity.[28,29] In the electronically nonadiabatic limit, $V_{\mu\nu} = V^{el} S_{\mu\nu}$, where $V^{el} = \langle\psi_i|H|\psi_f\rangle$ is the electronic coupling between the reactant and product electronic states ψ_i and ψ_f, and $S_{\mu\nu} = \langle\chi_\mu^{(i)}|\chi_\nu^{(f)}\rangle$ is the overlap integral between the reactant and product proton vibrational wave functions $\chi_\mu^{(i)}$ and $\chi_\nu^{(f)}$ (magenta region in Figure 27B). In the electronically adiabatic limit, the vibronic coupling is half the tunneling splitting for the ground electronic state. In the intermediate regime, a general expression for the vibronic coupling,[28,29] which is the product of a prefactor κ and the adiabatic vibronic coupling, should be used. The factor κ depends on the electronic coupling and the proton potential energy curves associated with the two diabatic electronic states. A variety of diagnostics have been devised to determine the degree of electron−proton nonadiabaticity.[29,283−285] For example, a semiclassical formalism[28] can be used to compute the effective electronic transition and proton tunneling times, and the ratio between these quantities determines the degree of electron−proton nonadiabaticity. An alternative approach is to analyze the electronic

https://doi.org/10.1021/acs.chemrev.1c00929
Chem. Rev. XXXX, XXX, XXX−XXX

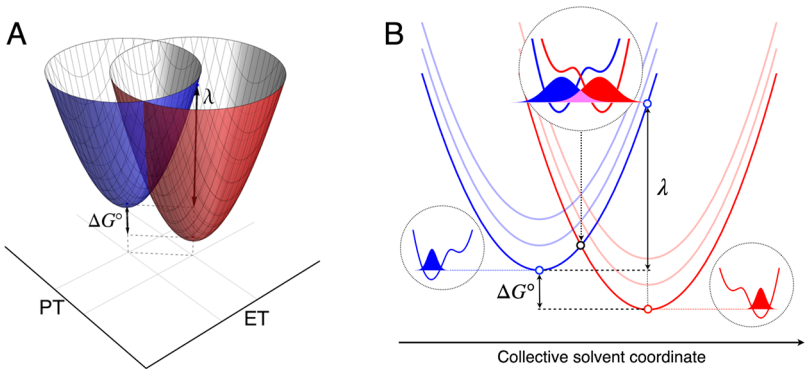

Figure 27. Schematic depiction of fundamental concepts underlying general PCET theory. (A) Reactant (blue) and product (red) two-dimensional vibronic free energy surfaces as functions of the ET and PT collective solvent coordinates. The reactant and product states correspond to the electron on its donor or acceptor, respectively. The reaction free energy ΔG° and reorganization λ are indicated. (B) One-dimensional slice connecting the minima of the vibronic free energy surfaces shown in panel A (dark blue and red parabolas for the reactant and product, respectively). The proton potential energy curves and associated ground state proton vibrational wave functions for the reactant (blue) and product (red) are depicted in gray circles. The overlap between the reactant and product proton vibrational wave functions at the crossing point, where the two vibronic states are degenerate, is shown in magenta. The lighter blue and red parabolas indicate the excited reactant and product vibronic free energy surfaces, which correspond to the excited proton vibrational states for each electronic state. Figure adapted with permission from ref 27. Copyright 2008 American Chemical Society.

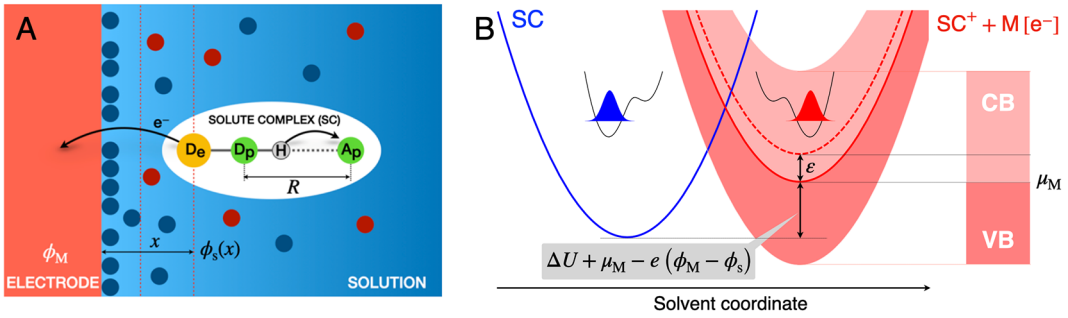

Figure 28. (A) Schematic picture of a homogeneous electrochemical PCET reaction system consisting of a solute complex near the surface of a metal electrode in solution. The electron transfers from the electron donor D_e of the solute complex to the electrode, and the proton transfers from D_p to A_p within the solute complex. Filled circles represent the ions of the supporting electrolyte in the solvent. ϕ_M is the inner potential of the electrode, $\phi_s(x)$ is the electrostatic potential in solution at a distance x from the electrode surface, and R is the proton donor−acceptor distance within the solute complex. (B) Free energy curves for the electrochemical PCET reaction as functions of the collective solvent coordinate. The reactant free energy curve on the left (blue) corresponds to the reduced form of the solute complex, SC, in solution and the metal electrode, M, in its initial electronic state. The continuum of curves on the right (red) represents the oxidized solute complex, SC^+, and the metal electrode, $M[e^-]$, with an additional electron occupying one of the one-electron states in the conduction band of the metal. In the anodic (oxidation) process, the reaction occurs via nonadiabatic transitions from the left curve to any of the curves in the product continuum. The transitions occur at the intersection points between the blue and red curves. The reaction free energy for each of these transitions is the sum of the intrinsic free energy difference, ΔU, the Fermi level of the electrode, μ_M, the energy, ε, of the accepting one-electron state of the electrode, and $-e(\phi_M - \phi_s)$, which arises from the difference between the electrostatic potentials in the metal and in solution at the location of the solute complex. The proton potential energy profiles as functions of the proton coordinate and the associated ground-state proton vibrational wave functions are also shown for the reactant and product vibronic states. Figure adapted with permission from ref 31. Copyright 2008 American Chemical Society.

charge distribution or the nonadiabatic coupling component along the proton transfer coordinate.[283−287]

The vibronic coupling depends strongly on the proton donor−acceptor distance R. As a result of this strong dependence, this PCET theory has been extended to include the dynamical motion of this proton donor−acceptor distance.[30] Analytical rate constant expressions were derived based on the assumption that the vibronic coupling decreases exponentially with R for each pair of reactant and product vibronic states, and a series of PCET rate constants were derived in well-defined regimes.[30] An alternative, more general approach utilizes a thermal averaging procedure, in which the PCET rate constant given in eq 19 is calculated at a series of different distances R to yield $k(R)$. In this approach, the total PCET rate constant is calculated by integrating over all values of R, weighting each rate constant $k(R)$ by the probability $P(R)$ of sampling that value of R:

$$k_{tot} = \int P(R)k(R)\,dR \tag{20}$$

The analytical and thermal averaged rate constants have been shown to be mathematically equivalent in certain well-defined limits.[288]

5.2. Vibronically Nonadiabatic Homogeneous Electrochemical PCET Theory

In homogeneous electrochemical PCET, the electrode serves as a reservoir for electrons but does not participate in the forming and breaking of chemical bonds. In this case, the electron transfers between the redox molecule and the electrode

https://doi.org/10.1021/acs.chemrev.1c00929
Chem. Rev. XXXX, XXX, XXX−XXX

concurrently with proton transfer within the molecule or hydrogen-bonded molecular complex (Figure 28A).

The vibronically nonadiabatic PCET theory described in the previous subsection has been extended to describe homogeneous electrochemical PCET.[31,289,290] An analogous four-state model is used to describe the PCET reaction, and the transferring proton is treated quantum mechanically. In the electrochemical case, the product state corresponds to a continuum of electronic states in the electrode (Figure 28), and the effects of the applied electrode potential and EDL must be included. The electrochemical PCET process is also described in terms of nonadiabatic transitions between reactant and product electron−proton vibronic states. Analogous to the homogeneous case, analytical rate constant expressions were derived in various well-defined regimes under the assumption that the vibronic coupling decreases exponentially with the proton donor−acceptor distance R. These expressions are provided elsewhere.[31,289] The expressions using the more general, thermal averaging procedure are given here.

For a fixed proton donor−acceptor distance R and distance x between the redox molecule and the electrode, the anodic and cathodic vibronically nonadiabatic PCET rate constants are[27,31,289,291]

$$k_a(\eta; R, x) = \frac{\rho_F}{\hbar\beta'}\sqrt{\frac{\pi}{\lambda k_B T}}\sum_{\mu,\nu} P_\mu |V_{\mu\nu}|^2 \int d\varepsilon [1 - f(\varepsilon)] \exp\left[-\frac{(\Delta\tilde{U}_{\mu\nu} + \varepsilon - e(\eta - \phi_s) + \lambda)^2}{4\lambda k_B T}\right]$$

$$k_c(\eta; R, x) = \frac{\rho_F}{\hbar\beta'}\sqrt{\frac{\pi}{\lambda k_B T}}\sum_{\mu,\nu} P_\nu |V_{\mu\nu}|^2 \int d\varepsilon f(\varepsilon) \exp\left[-\frac{(-\Delta\tilde{U}_{\mu\nu} - \varepsilon + e(\eta - \phi_s) + \lambda)^2}{4\lambda k_B T}\right] \quad (21)$$

Here ρ_F is the density of electronic states at the Fermi level of the electrode, $f(\varepsilon)$ is the Fermi distribution function for the electronic states with energy ε in the electrode, η is the overpotential defined relative to the formal electrode potential E°,[31,292] and ϕ_s is the electrostatic potential at the position x of the redox molecule relative to the potential in the bulk solvent.

Typically, homogeneous electrochemical PCET is expected to be electronically nonadiabatic with respect to the proton motion, mainly due to relatively large electron tunneling distances, and therefore $V_{\mu\nu} = V^{el}S_{\mu\nu}$.[29,283−285] Moreover, homogeneous electrochemical PCET is typically vibronically nonadiabatic in that the vibronic coupling $V_{\mu\nu}$ is much less than the thermal energy, mainly due to the small proton vibrational wave function overlap, allowing the use of the golden rule rate constant expression. In eq 21, β' is a parameter of magnitude ∼1 Å^{-1} representing the exponential decay of the electronic coupling V^{el} with distance x from the electrode surface. Moreover, $\Delta\tilde{U}_{\mu\nu} = \Delta U_{\mu\nu} + k_B T \ln(Q^{ox}/Q^{red})$, where $\Delta U_{\mu\nu}$ is the energy difference between the vibronic states ν and μ, and Q^{red} and Q^{ox} are the total partition functions of the reduced and oxidized solute species, respectively, in bulk solution. In practice, often it is reasonable to assume that $\Delta\tilde{U}_{\mu\nu} = \varepsilon_\nu - \varepsilon_\mu$, where ε_μ and ε_ν are the proton vibrational energy levels for the reactant and product relative to their respective ground states.[31] The other quantities are defined as for eq 19 in the previous subsection. Here P_μ, $V_{\mu\nu}$, and $\Delta\tilde{U}_{\mu\nu}$ depend on the proton donor−acceptor distance R, and typically the other quantities are assumed to be independent of R. A comparison between these rate constant expressions and those used by Savéant and co-workers[293−296] is provided elsewhere.[31]

The total homogeneous electrochemical anodic and cathodic PCET rate constants are obtained by thermal averaging over the proton donor−acceptor distance R:

$$k_a(\eta; x) = \int P(R) k_a(\eta; R, x)\, dR$$

$$k_c(\eta; x) = \int P(R) k_c(\eta; R, x)\, dR \quad (22)$$

In these expressions, $P(R)$ is the normalized probability distribution function for the proton donor−acceptor distance R. In principle, $P(R)$ could be different for the anodic and cathodic processes, but they are often assumed to be the same. In practice, $P(R)$ can be chosen to be the classical or quantum probability distribution function for a harmonic oscillator with specified equilibrium proton donor−acceptor distance and effective force constant. Alternatively, $P(R)$ can be computed numerically with a series of DFT geometry optimizations of the redox molecule with the proton donor−acceptor distance constrained. In general, $P(R)$ may depend on the applied potential, but this dependence is expected to be weak and therefore is often neglected because the proton transfer interface is spatially separated from the electrode surface in homogeneous electrochemical PCET (Figure 28A). The standard homogeneous electrochemical rate constant is defined for the η at which the anodic and cathodic current densities are equal, thus corresponding to the equilibrium potential. The anodic and cathodic current densities are obtained by explicit integration of the corresponding rate constants over the distance x between the redox molecule and the electrode, weighting by the concentrations of the reduced and oxidized species, C_{red} and C_{ox}, respectively:[31]

$$j_a(\eta) = F\int dx\, C_{red}(\eta; x) k_a(\eta; x)$$

$$j_c(\eta) = F\int dx\, C_{ox}(\eta; x) k_c(\eta; x) \quad (23)$$

Nonadiabatic PCET rate constant expressions have also been derived using model system-bath Hamiltonians in conjunction with a four-state model and a quantum mechanical treatment of the transferring proton.[39,289] The Anderson−Newns−Schmickler model for PCET[39] includes an explicit double-well potential for the proton and explicit electron−proton and proton−solvent interaction terms. This Hamiltonian describes the interaction between the redox molecule and the electrode in terms of electronic couplings that are independent of the proton and bath vibrational modes. A subsequent extension of this model Hamiltonian[289] is expressed in a basis of electron−proton vibronic states without introducing an explicit proton coordinate or proton potential. This extension also includes the proton donor−acceptor mode coordinate, which is known to be important for PCET,[30] and describes the interaction between the redox molecule and the electrode in terms of vibronic couplings that depend on this proton donor−acceptor mode coordinate.

The extended Anderson−Newns−Schmickler model Hamiltonian was also used to derive electrochemical PCET rate constant expressions that interpolate between the golden rule and solvent-controlled limits.[290] In the golden rule limit, which

https://doi.org/10.1021/acs.chemrev.1c00929
Chem. Rev. XXXX, XXX, XXX−XXX

corresponds to weak vibronic coupling and fast solvent relaxation, the rate constant is proportional to the square of the vibronic coupling and is independent of the solvent relaxation time. In the solvent-controlled limit, which corresponds to strong vibronic coupling and slow solvent relaxation, the rate constant is independent of the vibronic coupling and increases as the solvent relaxation time decreases. These rate constant expressions are provided elsewhere.[290]

5.3. Calculation of Input Quantities to Vibronically Nonadiabatic PCET Rate Constant Expressions

5.3.1. Reorganization Energy. The total reorganization energy is typically expressed as the sum of the inner-sphere and outer-sphere reorganization energies. The inner-sphere reorganization energy can be calculated using the extended four-point method given in eq 13. This expression requires geometry optimizations of the molecule in both the reduced and oxidized states, leading to the equilibrium geometries defined as Q^{red} and Q^{ox}, respectively. Subsequently, the energy of the oxidized state at Q^{red} is computed after optimizing the transferring proton at its position in the oxidized state, and the energy of the reduced state at Q^{ox} is computed after optimizing the transferring proton at its position for the reduced state. These two nonequilibrium energies, in conjunction with the energies of both states at their respective equilibrium geometries, are combined to compute the inner-sphere reorganization energy. These electronic energies are computed in the gas phase, but they may be computed for geometries optimized either in the gas phase or in solution because the geometries do not need to be stationary points in the gas phase.

The outer-sphere (solvent) reorganization energy can be calculated using the analytical expression given in eq 14. This expression depends on the static and optical dielectric constants of the solvent as well as the change in charge of the molecule upon oxidation or reduction, which is often ± 1. The radius of the spherical cavity representing the redox molecule can be estimated from the volume of the molecular cavity determined from a dielectric continuum model calculation. For simplicity, the distance between the molecule and the electrode can be assumed to be the same as the cavity radius (i.e., $d = a$ in eq 14), or it could be placed elsewhere if more information about its location is known. More elaborate calculations of the solvent reorganization energy with molecular cavities can be performed using electronic structure calculations combined with the IEF-PCM method[147,151,152] as described in subsection 2.6.2.

5.3.2. Proton Potentials, Vibrational Wave Functions, and Energy Levels. The vibronically nonadiabatic PCET theory described above requires the proton potential energy curves for the redox molecule at a range of different proton donor−acceptor distances R. The proton potentials for the reduced and oxidized states of the redox molecule can be computed in various ways. Here we describe one approach that has been successfully applied to homogeneous electrochemical PCET systems.[33] In this approach, the proton potentials are computed for average structures generated by averaging the optimized reduced and oxidized structures at each proton donor−acceptor distance R. This procedure is consistent with the occurrence of nonadiabatic transitions at the crossing point between the initial and final states, corresponding to a structure in between the equilibrium reduced and oxidized structures. In practice, constrained geometry optimizations are performed for the reduced and oxidized species for a series of distances R, and the reduced and oxidized structures are aligned and averaged for each R.

For each average structure, the proton coordinate is defined on a one-dimensional grid placed along the axis connecting the equilibrium positions of the proton on its donor and acceptor with all other atoms fixed. A series of single-point energy calculations at these grid points produces the proton potential energy curve for each proton donor−acceptor distance R. The shapes of the proton potential energy curves depend strongly on R, with the proton transfer barrier increasing as R increases. The proton vibrational wave functions and energy levels can be computed by numerically solving the one-dimensional Schrödinger equation for the proton moving according to each of these proton potential energy curves. These wave functions and energies are used to compute the overlap $S_{\mu\nu}$ and the energy splittings $\Delta U_{\mu\nu}$ in the PCET rate constant expressions given above.

5.3.3. Proton Donor−Acceptor Distance Probability Distribution Function. In the thermal averaging approach, the total homogeneous electrochemical rate constant is obtained by numerically integrating eq 22. In this expression, the probability distribution function $P(R)$ indicates the probability of sampling each proton donor−acceptor distance R. This probability distribution function can be calculated in several different ways. For example, it could be expressed as the probability distribution function for a classical harmonic oscillator. The equilibrium distance could be chosen to be the average of the proton donor−acceptor distances in the reduced and oxidized optimized structures. The effective force constant can be chosen to be the average of the effective force constants for the reduced and oxidized optimized structures. Each effective force constant can be obtained by projecting all of the normal modes onto the proton donor−acceptor axis and computing a weighted sum, as described elsewhere.[32,148] Alternatively, $P(R)$ could be obtained from the energies of the average structures used to compute the proton potential energy curves or from the energies determined from the constrained geometry optimizations of the reactant state (i.e., either the reduced or oxidized species).

5.3.4. Electronic Coupling. The electronic coupling between the redox molecule and the electrode states in the general nonadiabatic rate constant expression is usually assumed to be constant for the electrode states near the Fermi level. This assumption corresponds to the wide band approximation,[297] which is a reasonable approximation for most metals. In this case, the electronic coupling can be described by a single parameter V^{el}, which is associated with the electronic coupling between the redox molecule and the electronic state at the Fermi level of the metal electrode. The squared V^{el} then appears in the nonadiabatic rate constant expression as a prefactor and thus is not required when calculating relative rate constants or kinetic isotope effects because this prefactor cancels. When absolute rate constants are calculated, this parameter can in principle be computed using electronic structure methods such as constrained DFT[138,298−300] adapted for periodic calculations within the Projector Augmented Wave method.[301] To go beyond the wide band approximation, the total density of states weighted by the squared electronic couplings for all electronic states of the electrode, known as the weighted density of states (WDOS), must be calculated. This far more challenging task can be accomplished using complex scaling techniques,[302] Green's function methods,[303−305] and diabatization schemes based on projection operator techniques.[306−312]

https://doi.org/10.1021/acs.chemrev.1c00929
Chem. Rev. XXXX, XXX, XXX−XXX

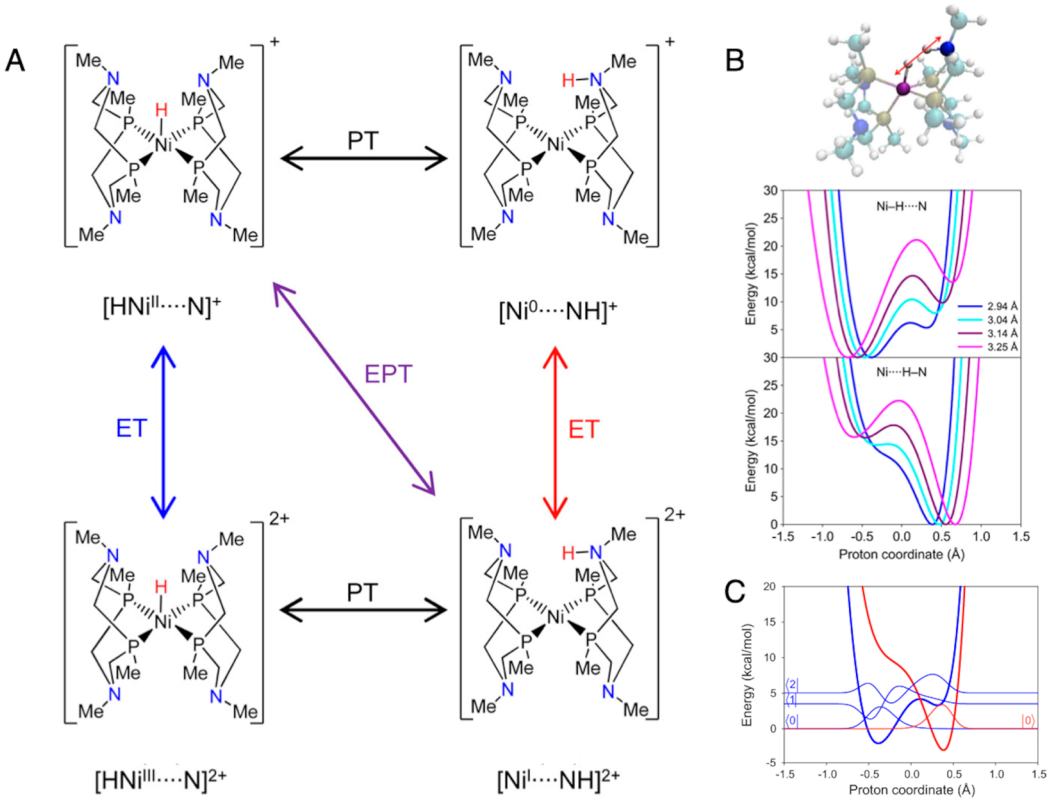

Figure 29. Application of vibronically nonadiabatic electrochemical PCET theory to $Ni(P_2N_2)_2$ electrocatalysts for hydrogen oxidation and evolution. (A) Four diabatic electronic states for PCET involving ET between the electrode and this electrocatalyst and PT between the nickel and the pendant amine nitrogen. (B) At the top is the electrocatalyst with the Ni (dark pink) and N (dark blue) atoms involved in the PT reaction, as well as the proton axis used for generation of the proton potentials (red line). The hydrogen atom is shown at its equilibrium position for both the reduced and oxidized states (i.e., bound to the Ni and N atoms, respectively), but in the calculations only one hydrogen atom is included here and is moved along the proton axis to generate the proton potentials. In the lower portion, proton potential energy curves for (top) the reduced state and (bottom) the oxidized state of the catalyst for the average structures at the Ni–N distances indicated. As the Ni–N distance decreases, the separation between the minima and the barrier for each proton potential decrease. (C) Proton potentials and corresponding vibrational wave functions for the contributing reactant (blue, reduced) and product (red, oxidized) vibronic states at a Ni–N distance of 2.94 Å. The main contributions to the standard rate constant arise from the (1,0) and (2,0) pairs of reactant/product vibronic states (i.e., the first and second excited reactant states in conjunction with the ground product state). These excited reactant proton vibrational wave functions (blue $\langle 1|$ and $\langle 2|$) are delocalized enough to have significant overlap with the ground product wave function (red $|0\rangle$). The dominant and average equilibrium Ni–N distances are 3.0 and 3.25 Å, respectively. A detailed analysis of the contributions of excited vibronic states to the total rate constant for other proton donor–acceptor distances and higher overpotentials is provided in ref 32. Figure adapted from ref 32. Copyright 2012 United States National Academy of Sciences.

5.4. Applications of Homogeneous Electrochemical PCET

5.4.1. Homogeneous Electrochemical PCET in Nickel Catalysts with Pendant Amines. The vibronically nonadiabatic PCET theory described in subsection 5.3 was used to study several different electrocatalytic systems. This formulation inherently includes the zero-point energy and tunneling effects of the transferring proton(s). One of the first examples is the investigation of the $Ni(P_2N_2)_2$ electrocatalysts for hydrogen oxidation and production.[32] In the PCET reaction studied, the electron transfers between the electrode and the nickel complex, and the proton transfers between the nickel and the nitrogen of the pendant amine. The four-state model for this PCET reaction is depicted in Figure 29A.[32] The molecular electrocatalyst and the proton potential energy curves for several different nickel–nitrogen distances are depicted in Figure 29B. The proton vibrational wave functions for the reactant and product vibronic states that contribute the most to the rate constant at a relatively short proton donor–acceptor distance are shown in Figure 29C. This study provided a clear illustration that the concerted PCET standard rate constant increases as the equilibrium proton donor–acceptor distance decreases. This trend was attributed to the greater overlap between the reactant and product proton vibrational wave functions, despite the lower probability of sampling these shorter distances. Thus, these calculations predicted that the concerted PCET mechanism would be favored when the pendant amine becomes more flexible because the contraction of this distance would incur a lower energy penalty.

5.4.2. Homogeneous Electrochemical PCET in Benzimidazole Phenols. This PCET theory was also used to study a range of substituted benzimidazole phenols (BIPs), which were designed to mimic the tyrosine–histidine pair in photosystem II.[33] In these systems, oxidation induces proton transfer from the oxygen to the nitrogen. The four-state model for this system is shown in Figure 30A, and the proton potential energy curves for a range of oxygen–nitrogen distances are shown in Figure 30B. The PCET mechanism was found to be concerted for this molecule. A variant of this BIP molecule with a $COOCH_3$ substituent, shown in Figure 30C, also exhibits a concerted PCET mechanism. The dominant pair of reactant/product vibronic states at the dominant oxygen–nitrogen distance for

https://doi.org/10.1021/acs.chemrev.1c00929
Chem. Rev. XXXX, XXX, XXX–XXX

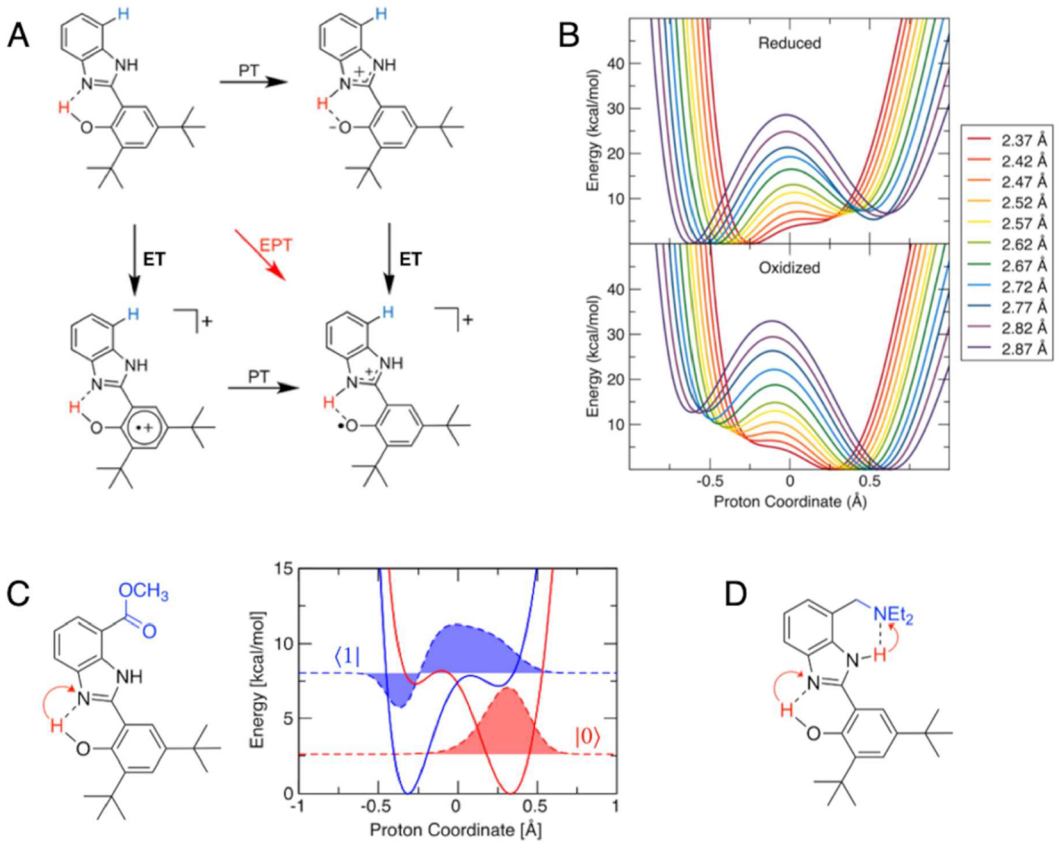

Figure 30. Application of vibronically nonadiabatic electrochemical PCET theory to BIP molecules designed to mimic the tyrosine−histidine pair in photosystem II. (A) Four diabatic electronic states for PCET involving ET between the electrode and the phenol of BIP and proton transfer between the oxygen and nitrogen. In the direction shown, oxidation induces proton transfer from oxygen to nitrogen. (B) Proton potential energy curves for (top) the reduced state and (bottom) the oxidized state of BIP for the average structures at the O−N distances indicated. (C) BIP-$COOCH_3$ molecule (left) with its proton potential energy curves and main contributing proton vibrational wave functions for the reduced (blue) and oxidized (red) states at the dominant O−N distance of 2.48 Å. The main contributing pair of reactant/product vibronic states at this distance is the (1,0) pair shown (i.e., the first excited reactant and ground product proton vibrational states). (D) BIP-CH_2NEt_2 (Et denotes an ethyl group) molecule that undergoes double proton transfer upon oxidation, corresponding to E2PT. Figure adapted from ref 33. Copyright 2017 American Chemical Society.

this BIP-$COOCH_3$ molecule was found to be the first excited reactant and the ground product vibronic states, as shown in Figure 30C.

DFT calculations of redox potentials guided the design of BIP molecules in which two, three, or four protons transfer upon oxidation.[33,313] For example, the amino-substituted BIP molecule shown in Figure 30D exhibits double proton transfer upon oxidation, denoted an E2PT mechanism. The PCET theory described earlier in this section[24] has been extended to systems with N charge transfer reactions, where N is the total number of possible electron and proton transfers. In this case, 2^N diabatic states are required, and the free energy surfaces depend on N collective solvent coordinates. The dimensionality of the proton potential energy surfaces and vibrational wave functions is equal to the number of proton transfer reactions. Thus, the E2PT system with one electron and two proton transfers shown in Figure 30D requires the calculation of two-dimensional proton potential energy surfaces and two-dimensional proton vibrational wave functions, as shown elsewhere.[33] The form of the rate constant expression given in eq 21 is still applicable to PCET reactions with multiple proton transfers.

A detailed analysis of the PCET rate constants for these systems provided an explanation of the experimentally observed kinetic isotope effects. In particular, the kinetic isotope effect is ∼2 for the BIP and BIP-$COOCH_3$ EPT systems, which exhibit only single proton transfer, but decreases to ∼1 for the amino-substituted E2PT system, which exhibits double proton transfer. These kinetic isotope effects were explained in terms of the dominant reactant/product vibronic states contributing to the PCET rate constant. The dominant contributions for the EPT systems exhibit moderate overlap between the reactant and product proton vibrational wave functions (Figure 30C), whereas the dominant contributions for the E2PT systems exhibit a larger overlap that does not distinguish as much between hydrogen and deuterium.[33,314]

5.4.3. Electrochemical PCET for Oxygen Reduction at Gold or Platinum Electrodes in Ionic Liquids. This vibronically nonadiabatic PCET theory[26,27,31] has also been used to investigate the ORR at an interfacial layer of protic ionic liquid on gold or platinum.[34] The ORR activity was found to be enhanced by the presence of the ionic liquid, with a volcano-shaped dependence on the pK_a of the ionic liquid. In the proposed mechanism, the ionic liquid protic cation forms a hydrogen bond with OOH adsorbed on the gold electrode or OH adsorbed on the platinum electrode. The ensuing concerted PCET reaction entails proton transfer from the protic cation to the adsorbed species, producing H_2O_2 or H_2O, respectively, in conjunction with electron transfer from the metal electrode (Figure 31). Although this is a heterogeneous PCET reaction, the homogeneous concerted PCET rate constant expres-

https://doi.org/10.1021/acs.chemrev.1c00929
Chem. Rev. XXXX, XXX, XXX−XXX

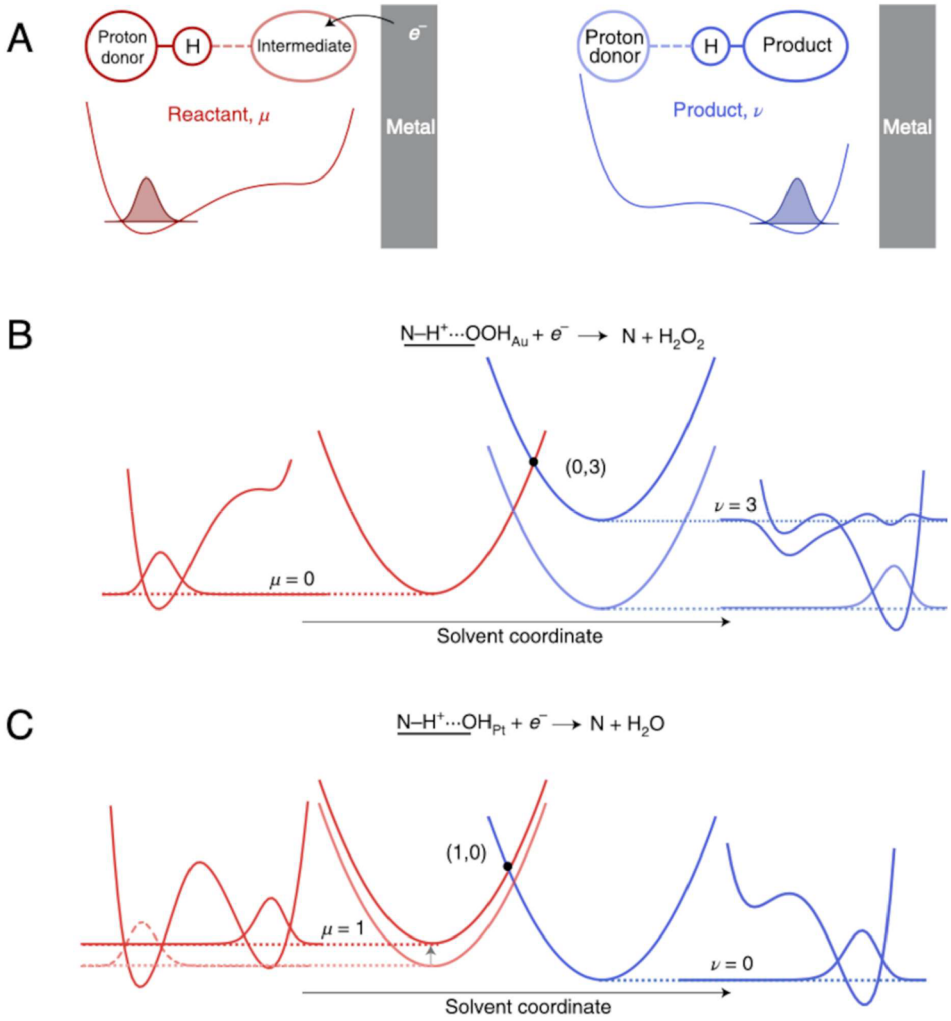

Figure 31. Application of vibronically nonadiabatic electrochemical PCET theory to the oxygen reduction reaction at Pt and Au surfaces. (A) Schematic of the PCET reaction at a hydrogen-bonded interface. The red and blue curves depict the proton potential and wave function in the ground state of the reactant and product as functions of the proton coordinate. The intermediate corresponds to either OOH adsorbed on Au (OOH_{Au}) or OH adsorbed on Pt (OH_{Pt}). The PCET reactions at these surfaces are ($N{-}H^{+}{\cdots}OOH_{Au} + e^{-} \rightarrow H_2O_2 + N$) and ($N{-}H^{+}{\cdots}OH_{Pt} + e^{-} \rightarrow H_2O + N$). (B, C) Schematic depiction of the free energy curves and associated proton potentials and wave functions for the dominant contributing pair of reactant and product vibronic states for each of these PCET reactions. Figure adapted with permission from ref 34. Copyright 2021 Springer Nature Limited.

sion[26,27,31] was used to describe it by treating the protic cation and either OOH or OH as a hydrogen-bonded molecular species in implicit 2-pentanone solvent, neglecting the effects of the electrode and the applied potential. Analysis of the contributions to the rate constant indicated that the observed dependence of ORR activity on the pK_a of the ionic liquid can be explained in terms of stronger hydrogen bonds exhibiting greater overlap integrals $S_{\mu\nu}$ for the dominant pair of reactant and product vibronic states (Figure 31). Thus, these calculations revealed that stronger hydrogen-bonding interactions between ionic liquids and ORR intermediates with comparable pK_a values enhance the hydrogen tunneling probability of the interfacial PCET reaction.

6. THEORY OF HETEROGENEOUS ELECTROCHEMICAL PCET

In heterogeneous electrochemical PCET processes, the electrode participates directly in the chemical reaction, specifically the breaking and forming of chemical bonds during the proton transfer reaction. Thus, the electrode surface not only serves as a reservoir for electrons but also plays the role of proton acceptor in the adsorption process or proton donor in the desorption process. In some cases, a chemisorbed species may play this role of proton acceptor and donor. Heterogeneous electrochemical PCET underlies a wide range of electrocatalytic processes. Although many of the fundamental concepts discussed in the previous section for homogeneous electrochemical PCET also apply to the heterogeneous reaction, several new concepts must be developed when the electrode participates in the chemical reaction.

The HER at metal electrodes has been widely studied due to its importance in hydrogen production from water splitting and as the reverse of the anodic hydrogen oxidation reaction in hydrogen fuel cells.[181,315,316] The first elementary step in heterogeneous HER is proton discharge on the electrode surface, also referred to as the Volmer step. This step can be viewed as a heterogeneous electrochemical PCET reaction because both a proton and an electron participate in a single elementary act occurring at the electrode surface. The Volmer

https://doi.org/10.1021/acs.chemrev.1c00929
Chem. Rev. XXXX, XXX, XXX−XXX

step can be formally described by the following chemical equation

$$AH^+ + M^* + e^- \rightleftharpoons A + MH_{ads} \quad (24)$$

where AH^+ is the general acid playing the role of the proton donor, M* designates an active site on the electrode surface, and MH_{ads} is the adsorbed hydrogen atom. The electron on the left side of this equation is supplied from the electron reservoir of the metal electrode kept at a constant applied potential. Although the subsequent steps of HER resulting in formation of molecular hydrogen are very important and sometimes even rate limiting, they will not be described here. Instead, this section will focus on the Volmer step, which represents the most fundamental heterogeneous electrochemical PCET reaction.

6.1. Early Models for Proton Discharge on Metal Electrodes

Early theoretical models of proton discharge on metal electrodes[35,317−320] were based on an adiabatic picture of proton transfer from the donor molecule (i.e., the general acid) to the active site on the electrode surface occurring by a thermally activated process of breaking and forming of the chemical bonds. Bockris and Matthews[319] suggested that initially the proton is delivered to one of the water molecules near the surface of the electrode by a fast Grotthuss-type transfer from a hydronium ion in the bulk solution. Then the elementary act of proton discharge occurs as a proton transfers from the surface hydronium to the active site at the electrode surface. In this model, the reaction coordinate was associated with the transferring proton, and the energy profile along the proton coordinate was assumed to have a typical double well form with a barrier. The quantum mechanical nature of the proton transfer was also recognized to be important, and early quantum mechanical models[35,319] described the proton transfer as tunneling between the ground vibrational levels in the reactant and product wells under the barrier approximated by an analytical Eckart barrier. In these models, the role of the solvent in the reaction was underestimated and was reduced to equilibrium solvation of the reactant complex. The coupling of solvent fluctuations to the reaction coordinate was simply ignored.

The early nonadiabatic theoretical models for the Volmer step or proton discharge on metal electrodes[36,37,321,322] were based on the nonadiabatic theory of electrochemical ET developed by Marcus, Levich, and Dogonadze.[20−22,323,324] As in ET theory, the reaction is described in terms of nonadiabatic transitions between the initial and final quantum states when these states are brought into resonance by the fluctuations of the slow classical environment described by the solvent polarization. In the case of the proton discharge reaction, however, the initial and final states are represented as products of the initial and final electronic states $|\psi_i\rangle$ and $|\psi_f\rangle$ and the corresponding proton vibrational states $|\chi_\mu^{(i)}\rangle$ and $|\chi_\nu^{(f)}\rangle$. The proton vibrational states are obtained by quantization along the proton coordinate in the initial and final electronic states and are assumed to be independent of the solvent configuration due to weak coupling between the solvent polarization and the proton. In the original formulation,[36] the theory was based entirely on the harmonic approximation, and the proton vibrational states were defined as harmonic oscillator states for the normal modes associated with the hydrogen stretch in the initial (i.e., the proton in the hydronium ion, H_3O^+) and final (i.e., the adsorbed hydrogen atom) electronic states. The stretching vibrational modes of the proton are usually well localized with high frequencies on the order of 3000 cm^{-1}, and thus the separation of the proton motion within the double adiabatic approximation is reasonable.

For a metal electrode kept at a constant applied potential E, the transition probability $W(\varepsilon, E)$ for the discharge of the hydronium ion when an electron is supplied from one of the occupied levels ε of the metal electrode can be obtained using Fermi's golden rule and averaging over all pairs of proton vibrational states. In this case, the transition probability is

$$W(\varepsilon, E) = \frac{1}{Z_p} \sum_\mu e^{-\varepsilon_\mu^{(i)}/k_B T} \sum_\nu w_{\mu\nu}(\varepsilon, E) \quad (25)$$

where Z_p is the proton vibrational partition function, $w_{\mu\nu}(\varepsilon, E)$ is a partial transition probability for a given pair of initial and final proton vibrational states $|\chi_\mu^{(i)}\rangle$ and $|\chi_\nu^{(f)}\rangle$, and $\varepsilon_\mu^{(i)}$ are the energies of the reactant proton vibrational states. In the harmonic approximation, the latter quantity was obtained analytically in various limits.[36,37] In the nonadiabatic regime and the high temperature limit for the solvent modes, the expression for $w_{\mu\nu}(\varepsilon, E)$ closely resembles the nonadiabatic expression for electrochemical ET:

$$w_{\mu\nu}(\varepsilon, E) = \frac{1}{\hbar} |V^{el} S_{\mu\nu}|^2 \sqrt{\frac{\pi}{\lambda k_B T}} \exp\left[-\frac{(\Delta U_{\mu\nu} + \varepsilon - eE + \lambda)^2}{4\lambda k_B T} \right] \quad (26)$$

Here V^{el} is the constant electronic coupling parameter, λ is the solvent reorganization energy, $\Delta U_{\mu\nu}$ is the intrinsic energy bias, which includes the energy difference $\varepsilon_\nu^{(f)} - \varepsilon_\mu^{(i)}$ for the pair of proton vibrational states μ and ν, and $S_{\mu\nu} = \langle \chi_\mu^{(i)} | \chi_\nu^{(f)} \rangle$ is the proton vibrational overlap. The additional prefactor with the proton vibrational overlap does not appear in the theory of electrochemical ET and reflects the effects of proton tunneling in the nonadiabatic limit.

Finally, the expression for the total current density associated with proton discharge is obtained by integrating over all occupied energy levels in the electrode

$$j(E) = FC_s \int W(\varepsilon, E) f(\varepsilon) \rho(\varepsilon)\, d\varepsilon \quad (27)$$

where F is the Faraday constant, C_s is the surface concentration of hydronium ions, $f(\varepsilon)$ is the Fermi distribution function, and $\rho(\varepsilon)$ is the density of electronic states in the electrode. Model calculations using various limits of the general expression in eq 27 for a wide range of applied potentials were used to explain the basic features of Tafel plots, including the deviation from linear behavior observed in the region of high overvoltage.[36]

This nonadiabatic theory, referred to as the Dogonadze−Kuznetsov−Levich (DKL) model for the electrochemical proton discharge reaction, was extended and generalized in several important directions.[38,325−329] These directions include developing models with different frequencies of the proton vibration in the initial and final states,[325] accounting for electron−electron repulsion leading to modulation of the effective charge on the transferring proton due to interaction with the electrostatic environment,[326] accounting for electronic friction due to electron−hole excitations in the electrode,[328] and incorporating the effects of the interaction of the local proton mode with the environment.[329] These models were reasonably successful in reproducing the experimentally observed dependence of the transfer coefficient on the applied potential, in particular, the much wider high overvoltage regions with linear

https://doi.org/10.1021/acs.chemrev.1c00929
Chem. Rev. XXXX, XXX, XXX−XXX

Tafel plots and constant transfer coefficient than predicted by the original DKL model. The important contributions of the excited proton vibrational states were also shown to be partially responsible for extended linear regions of the Tafel plots.[326]

6.2. Potential-Dependent Kinetic Isotope Effects for Volmer Reaction in Acetonitrile

The interest in theoretical modeling of the proton discharge reaction has been renewed recently due to refined experiments that pose new questions[330−335] and suggest that the underlying mechanism of this elementary reaction is not yet fully understood. As an illustrative example, recent electrochemical experiments[334] probing the reaction of proton discharge from triethylammonium ($TEAH^+$) and its deuterated counterpart ($TEAD^+$) on a gold surface in acetonitrile (Figure 32) revealed

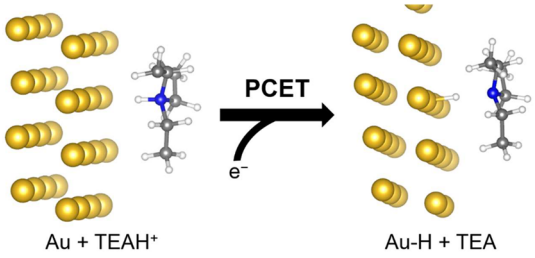

Figure 32. Schematic depiction of the PCET reaction between $TEAH^+$ and the Au electrode surface; Au atoms are gold, N atoms are blue, C atoms are gray, and H atoms are white. Figure reproduced with permission from ref 216. Copyright 2019 American Chemical Society.

new features that have not been observed in acidic aqueous solution, where the proton donor is the hydronium ion H_3O^+. These experiments showed significantly different Tafel slopes for $TEAH^+$ and $TEAD^+$, resulting in a kinetic isotope effect that depends strongly on the applied potential. This phenomenon has been explained[216] using an extension of the vibronically nonadiabatic electrochemical PCET theory[31,289] described in subsection 5.2, which is also related to the nonadiabatic theory for proton discharge discussed in subsection 6.1.

To model the experimental data,[334] the cathodic current density was calculated[216] by thermal averaging of the nonadiabatic rate constant $k(R, E)$ over the distance R between the proton donor (i.e., the nitrogen atom) and the gold electrode surface:

$$j(E) = F\int c_{HA^+}(R, E)k(R, E)\,dR \tag{28}$$

Here $c_{HA^+}(R, E)$ is the potential-dependent concentration of the acid at the distance R from the electrode surface. Note that R is the proton donor−acceptor distance, analogous to its definition for the homogeneous case in section 5, except the proton acceptor is the gold electrode surface in the Volmer reaction, and the probability distribution function is replaced by the concentration of the acid.

The rate constant is given by the following weighted sum of partial rate constants for nonadiabatic transitions between pairs of reactant and product electron−proton vibronic states with indices μ and ν, respectively:[31,216]

$$k(R, E) = \frac{\rho_F}{\hbar}\sqrt{\frac{\pi}{\lambda k_B T}}\sum_{\mu,\nu} P_\mu |V_{\mu\nu}(R)|^2 \int f(\varepsilon)\exp\left[-\frac{(\Delta G_{\mu\nu}(R, E, \varepsilon) + \lambda)^2}{4\lambda k_B T}\right] d\varepsilon \tag{29}$$

Here ρ_F is the density of states at the Fermi level for the gold electrode, λ is the total reorganization energy, which includes outer-sphere solvent and inner-sphere solute components, P_μ is the Boltzmann population of the reactant vibronic state μ, $V_{\mu\nu}(R)$ is the coupling between the vibronic states μ and ν, and $f(\varepsilon)$ is the Fermi distribution function.

The free energy difference $\Delta G_{\mu\nu}(R, E, \varepsilon)$ for the pair of states μ and ν depends on the distance R to the electrode surface, the applied potential E relative to the reference potential E_{ref}, and the energy of the electronic level ε relative to the Fermi level:

$$\Delta G_{\mu\nu}(R, E, \varepsilon) = \Delta G^\circ(R) + \Delta\varepsilon_{\mu\nu} - \varepsilon + e(E + E_{ref}) - e\phi_s(R, E) \tag{30}$$

Here ΔG° is the intrinsic free energy bias, which includes the nonelectrostatic work term associated with bringing the acid molecule from bulk solution to a distance R from the electrode surface and moving the conjugate base from R to bulk solution, $\Delta\varepsilon_{\mu\nu}$ is the difference between the proton vibrational energy levels for the product vibronic state ν and the reactant vibronic state μ relative to the minima of their respective potentials, and $\phi_s(R, E)$ is the electrostatic potential near the electrode surface relative to bulk solution. The electrostatic potential $\phi_s(R, E)$ was calculated in the framework of the extended Gouy−Chapman−Stern model with a variable dielectric constant in the outer Helmholtz layer,[213,215,216,336] as described in subsection 4.1. Note that the dependence of the rate constant in eq 29 on the distance R is determined by a balance between the distance dependence of the vibronic coupling and the electrostatic potential.[216,337]

One of the important differences between the model employed in ref 216 and the earlier nonadiabatic models is the treatment of the vibronic couplings $V_{\mu\nu}(R)$ between the mixed electron−proton vibronic states. These couplings were calculated using the general semiclassical expression valid in the electronically adiabatic and nonadiabatic regimes as well as the intermediate regime[28,29]

$$V_{\mu\nu} = \kappa_{\mu\nu}\frac{\Delta_{\mu\nu}}{2} \tag{31}$$

Here $\Delta_{\mu\nu}$ is the tunneling splitting between two vibrational levels in the electronically adiabatic proton potential computed from the diabatic electronic proton potentials associated with the degenerate vibrational levels μ and ν (see ref 216 for technical details). Moreover, the prefactor $\kappa_{\mu\nu}$ depends on the electronic coupling and other quantities that are obtained from the diabatic electronic proton potentials. This prefactor spans the electronically adiabatic ($\kappa_{\mu\nu} \approx 1$) and electronically nonadiabatic ($\kappa_{\mu\nu} \ll 1$) regimes. In the electronically nonadiabatic regime, the expression in eq 31 reduces to the product of the electronic coupling and the proton vibrational overlap, $V_{\mu\nu} = V^{el} S_{\mu\nu}$.

This theoretical model[216] was able to reproduce the experimentally measured Tafel plots for the Volmer reaction from $TEAH^+$ and $TEAD^+$ to gold in acetonitrile.[334] The results presented in Figure 33B exhibit excellent agreement with the experimental data in Figure 33A. Most of the input quantities to

https://doi.org/10.1021/acs.chemrev.1c00929
Chem. Rev. XXXX, XXX, XXX−XXX

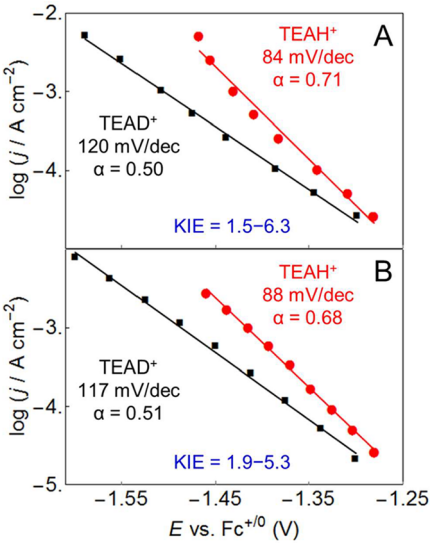

Figure 33. Tafel plots, which reflect the current density versus the applied potential, obtained from (A) experimental data[334] and (B) theoretical calculations[216] for the PCET reaction associated with proton discharge from $TEAH^+$ (red circles) or $TEAD^+$ (black, squares) on a gold electrode in acetonitrile. The theoretical data are shifted horizontally to correspond to the experimental range of applied potentials. The reported Tafel slopes and electrochemical transfer coefficients, α, are obtained from linear fits to the data points shown. The smallest and largest KIEs reported are the ratios between the $TEAH^+$ and $TEAD^+$ linear fits at −1.30 V and −1.46 V, respectively. Figure reproduced with permission from ref 216. Copyright 2018 American Chemical Society.

the rate constant expression were calculated with DFT or other computational methods, but there were also several free parameters fit to certain aspects of the experimental data, such as constants that shifted the absolute values of the current density and applied potential. More important than the quantitative agreement with the experimental data was the ability of this theoretical model to describe the potential-dependent kinetic isotope effect and to provide a physical explanation for this unusual phenomenon.

The analysis of the contributions of individual pairs of reactant and product vibronic states to the total current density revealed that the different Tafel slopes measured for $TEAH^+$ and $TEAD^+$ are due to different relative contributions from excited vibronic states that depend strongly on the applied potential. In $TEAH^+$, the pair of vibronic states corresponding to the first excited reactant and ground product vibronic states represented the dominant contribution to the current density, whereas in $TEAD^+$, the pair of vibronic states corresponding to the second excited reactant and ground product vibronic states represented a significant contribution. The greater contribution from higher excited reactant vibronic states for deuterium is due to the smaller splittings between the vibrational states for deuterium than for hydrogen, leading to greater Boltzmann populations of the excited reactant vibronic states for deuterium. The percentage of this contribution depends on the applied potential, leading to a potential-dependent kinetic isotope effect. In this formalism, the magnitude and potential dependence of the kinetic isotope effect are determined primarily by the relative contributions from the excited vibronic states and the corresponding vibrational wave function overlaps for hydrogen and deuterium.

The importance of the contributions from excited proton vibrational states to the total current density was also emphasized when analyzing the origins of the wide linear regions in the Tafel plots at high overvoltages in the framework of earlier nonadiabatic models.[322] It appears that the participation of excited proton vibrational states is a characteristic feature of nonadiabatic electrochemical PCET theories with quantization of the transferring proton.

6.3. Adiabatic Models for Volmer Reaction

As discussed in subsection 6.1, early adiabatic models of the Volmer reaction described the elementary act of proton discharge as overcoming the barrier on the free energy surface corresponding to the ground electronic adiabatic state of the reaction system. If an excess proton is delivered to the compact layer via Grotthuss-type transfer from the bulk solution, as hypothesized by Bockris and Matthews,[319] or comes directly from a water molecule, as must be the case in alkaline solution, then the adiabaticity of the electron−proton subsystem with respect to the environment degrees of freedom might be a reasonable assumption. Relatively short distances between the water molecules in the compact layer and the electrode surface would imply strong electronic coupling with partially occupied electronic bands of the metal electrode. When the proton is treated quantum mechanically, the double adiabatic approximation is often invoked, whereby the transferring proton responds instantaneously to the classical motion of the solvent nuclei, and the electrons respond instantaneously to the motion of the proton. In this approximation, the reaction proceeds on a single free energy surface corresponding to the ground double adiabatic electron−proton vibronic state.

An adiabatic model for the combined electron and proton transfer in electrochemical systems was developed by Grimminger and Schmickler[39,59] and further extended by Koper.[42,338] They proposed a model Hamiltonian similar to the Anderson−Newns Hamiltonian used in chemisorption theory[339−342] and adiabatic theories of electrochemical ET.[343−350] In addition to electronic terms for the transferring electron and quasi-free electrons in the metal electrode, the model Hamiltonian also included the proton terms for two localized quantum states of the proton corresponding to the proton bonded to its donor or acceptor, respectively. The solvent environment was represented by a bath of harmonic oscillators linearly coupled to both the electron and proton subsystems.[39,42] In the simple case when only two modes of bath oscillators are coupled to the electron and the proton, it is straightforward to define two reaction coordinates corresponding to the reorganization of these two modes and associate them with the electron and proton transfer directions, respectively. The two-dimensional adiabatic ground state potential energy surface for this model Hamiltonian can be obtained analytically in the mean-field approximation and can be used for the analysis of the reaction mechanism,[39,42] dynamical simulations, and estimations of rate constants using adiabatic rate theories.[59] This construction is very similar to the original general formulation of the multistate continuum theory of homogeneous PCET reactions[24−27] based on the four-state model of the electronic subsystem, as described in section 5. As also discussed in section 5, the corresponding model system-bath Hamiltonian in the second quantization representation in the basis of electron−proton vibronic states coupled to the bosonic bath of harmonic oscillators was rigorously derived and used to formulate nonadiabatic theories of electrochemical PCET.[289,290]

https://doi.org/10.1021/acs.chemrev.1c00929
Chem. Rev. XXXX, XXX, XXX−XXX

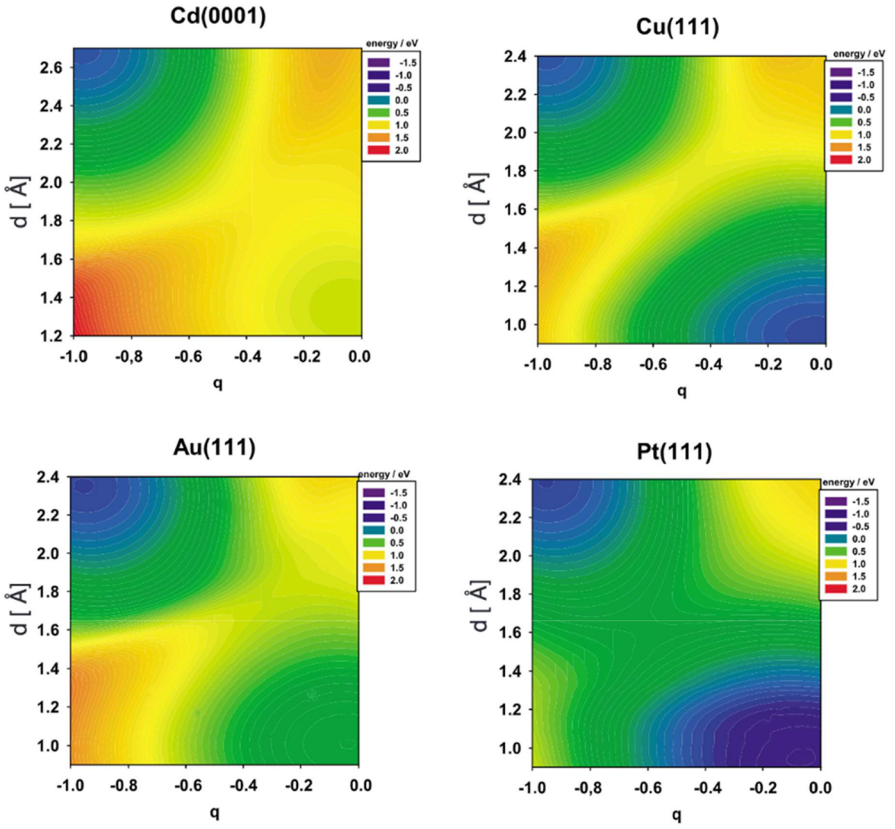

Figure 34. Free energy surfaces for hydrogen adsorption at Cd(0001), Cu(111), Au(111), and Pt(111). Figure reproduced with permission from ref 41. Copyright 2009 American Physical Society.

An adiabatic model specifically designed for the reaction of proton discharge on metal electrodes was developed by Santos and Schmickler based on the adiabatic theory for electrochemical ET coupled to bond breaking.[351−353] This model describes the proton discharge reaction as the outer-sphere electron transfer from the metal electrode to the 1s-orbital localized on the proton and unoccupied in the reactant state.[41,354−357] This picture is reminiscent of the Anderson−Newns model of chemisorption[341] except that it explicitly treats the distance from the proton to the electrode surface as one of the reaction coordinates. In the mean field approximation, the analytical expression for the two-dimensional adiabatic ground state potential energy surface as a function of the generalized solvent coordinate q and the distance d from the proton to the electrode surface has the following simple form

$$E(r, q) = \int_{-\infty}^{0} \rho_a(\varepsilon)\varepsilon \, d\varepsilon + \lambda q^2 + 2\lambda q \tag{32}$$

Here λ is the solvent reorganization energy, and $\rho_a(\varepsilon)$ is the projected density of states for the hydrogen 1s orbital. This key quantity is expressed as

$$\rho_a(\varepsilon) = \frac{\Delta(\varepsilon)}{\{\varepsilon - [\varepsilon_a + \Lambda(\varepsilon) - 2\lambda q]\}^2 + \Delta(\varepsilon)^2} \tag{33}$$

where ε_a is the energy of the unperturbed hydrogen 1s orbital. In this expression, $\Delta(\varepsilon)$ is the weighted density of states (WDOS), defined as the density of electronic states in the metal weighted by the electronic couplings V_k with the hydrogen 1s orbital,

$$\Delta(\varepsilon) = \sum_{k} |V_k|^2 \delta(\varepsilon - \varepsilon_k) \tag{34}$$

and $\Lambda(\varepsilon)$ is the level shift or chemisorption function,

$$\Lambda(\varepsilon) = \mathcal{P} \int \frac{\Delta(\varepsilon')}{\varepsilon - \varepsilon'} \, d\varepsilon' \tag{35}$$

with $\mathcal{P}$ denoting the principal value integral. The WDOS in eq 34 can in principle be obtained from electronic structure calculations either directly or by fitting the parameters of a model function for $\Delta(\varepsilon)$, typically in the form of a semielliptic electronic band, to reproduce the calculated $\rho_a(\varepsilon)$. This strategy was used in model calculations in conjunction with electronic structure parameters obtained in DFT calculations.[41,357] Examples of the calculated free energy surfaces for proton discharge on various metal electrodes are shown in Figure 34.

Another adiabatic model of proton discharge on metal electrodes has been developed with the aim to perform large-scale explicit MD simulations of metal/electrolyte solution interfaces.[40,358] This model utilizes the multistate empirical valence bond (EVB) methodology[359−362] to describe the proton translocation near the electrode surface via the Grotthuss mechanism. The EVB model parametrized with assistance from DFT calculations was used to perform large-scale MD simulations for H_2O/Pt(111)[40] and H_2O/Ag(111)[358] interfaces with an excess proton for different surface charge densities. The simulations revealed interesting energetic and structural features of these complex interfaces.

The importance of noncovalent interactions in the EDL has been stressed in a recent theoretical framework.[363] This adiabatic framework is based on the Anderson−Newns model

https://doi.org/10.1021/acs.chemrev.1c00929
Chem. Rev. XXXX, XXX, XXX−XXX

Hamiltonian with an additional noncovalent term that is derived self-consistently from the mean field model of the EDL. The model has been used to describe the kinetics of the Volmer reaction in alkaline conditions.[364]

A more general electronically adiabatic model that includes the nuclear quantum effects of the transferring proton in the double adiabatic approximation was developed for proton discharge on metal electrodes.[365] In this model, the electronic states are described in the framework of EVB theory, the electrostatic solvent interactions in the bulk and EDL are treated using a multilayer dielectric continuum model, and quantization along the proton coordinate accounts for hydrogen tunneling effects. This formulation allows the calculation of the ground and excited state electron−proton vibronic free energy surfaces as functions of the proton donor−acceptor distance and a collective solvent coordinate.

In this model, the electronic model Hamiltonian is constructed in the basis of diabatic EVB states depicted in Figure 35. The single reactant state corresponds to the valence

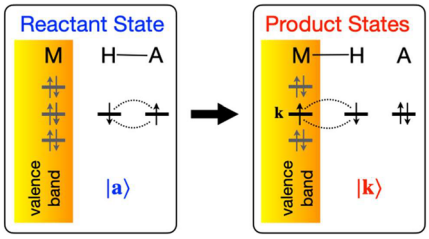

Figure 35. Schematic depiction of the reactant and product diabatic electronic states for the Volmer reaction. The dotted arcs connecting the electrons of opposite spins occupying the donor and hydrogen orbitals in the reactant state and the hydrogen and metal orbitals in the product states designate a conventional two-electron covalent bond. These product states form a basis for the product state corresponding to hydrogen adsorbed to the metal surface. Figure adapted with permission from ref 365. Copyright 2019 American Chemical Society.

bond state with two electrons forming a covalent bond between the hydrogen and the donor atom of the general acid. The continuum of product states includes all of the valence bond states with two electrons shared between the orbital localized on hydrogen and one of the delocalized orbitals below the Fermi level in the metal electrode. These valence bond states are used as a basis set to describe the physically meaningful product state for a hydrogen atom adsorbed at one of the active sites of the electrode surface. The interaction with the solvent polarization is incorporated into this model Hamiltonian by analogy with the standard ET theory in the linear response regime. The resulting infinite-dimensional matrix representation of the Hamiltonian is parametrized to yield matrix elements that depend on the applied potential E, proton coordinate r, distance R between the proton donor and the electrode surface, and a single collective solvent coordinate X related to the difference (energy gap) in electrostatic interaction energies of the solute charge distributions in the reactant and product states with the inertial polarization field of the solvent.

In this framework, the free energy surfaces for the ground and excited electronic states $\mathcal{U}_i(r, R, X; E)$ are obtained by diagonalization of the electronic Hamiltonian matrix. For a continuum of basis states, the eigenvalues are solutions of the following nonlinear equation for the energy $\mathcal{E}$:

$$\mathcal{E} + \Delta\mathcal{G}_F(r, R, E) + X - \tilde{\Lambda}(\mathcal{E}) + i\tilde{\Delta}(\mathcal{E}) = 0 \quad (36)$$

where $\Delta\mathcal{G}_F(r, R, E)$ is the gas phase electronic energy bias, $\tilde{\Lambda}(\varepsilon)$ is the WDOS for the occupied levels of the electrode, and $\tilde{\Delta}(\varepsilon)$ is its Hilbert transform or chemisorption function. For a given WDOS and chemisorption function parametrized using periodic DFT calculations, the nonlinear equation in eq 36 can be solved numerically, producing the ground state free energy surface $\mathcal{U}_0(r, R, X; E)$ and a continuum of excited state surfaces, separated from the ground state by a finite energy gap.[366] To obtain the double adiabatic vibronic free energy surfaces, the transferring proton is quantized by solving the vibrational Schrödinger equation for the proton moving on $\mathcal{U}_0(r, R, X; E)$ along the proton coordinate r at fixed values of the other coordinates.

This model was parametrized to describe proton discharge from the hydronium ion on a gold electrode. The calculated ground and excited state adiabatic vibronic free energy surfaces as functions of the solvent coordinate X and the distance R between the proton donor and the electrode surface revealed important features of the free energy landscape for this reaction. These calculations also illustrated how the free energy surface is influenced by the applied potential and the strength of electronic coupling for the d- and sp-bands of the gold electrode. Illustrative examples of two-dimensional free energy surfaces for three different strengths of electronic coupling are shown in Figure 36.

Three important features of the vibronic free energy surfaces were observed from these calculations.[365] First, the increase in the strength of the electronic coupling with the electronic bands of the electrode stabilizes only the reactant and saddle point regions of the ground state free energy surface while having virtually no effect on the product region. This feature is also characteristic of other related adiabatic models[343,346,366] for an electronic level interacting with a continuum of electronic states. Second, the distance of the proton donor from the electrode surface is significantly larger in the product minimum than in the reactant minimum, suggesting that the proton donor (i.e., water) is immediately expelled from the electrode surface after the proton is transferred. Finally, the analysis of the excited state vibronic free energy surfaces revealed that even in the compact layer with relatively short distances between the proton donor and the electrode surface, there exist avoided crossing regions with small energy gaps between the adjacent vibronic surfaces. This finding indicates that vibrational nonadiabaticity may play an important role in proton discharge reactions, and the reaction might span all regimes from the fully adiabatic at shorter distances near the electrode surface to nonadiabatic at longer distances further away from the electrode. Thus, a balanced description may require approaches capable of properly interpolating between these regimes.

6.4. Vibrational Nonadiabaticity and Interpolation Schemes for Volmer Reaction

A curve-crossing formulation for the Volmer reaction was developed[43] as a generalization of the adiabatic model in ref 365 to include effects of vibrational nonadiabaticity and solvent dynamics. This idea of combining the adiabatic and nonadiabatic theories of electrochemical PCET into a universal model is rooted in the analogous theories of ET reactions.[367−378] In the PCET formulation, the reaction is described in terms of Landau−Zener nonadiabatic transitions at the crossing point between the two diabatic vibronic states obtained by exact

https://doi.org/10.1021/acs.chemrev.1c00929
Chem. Rev. XXXX, XXX, XXX−XXX

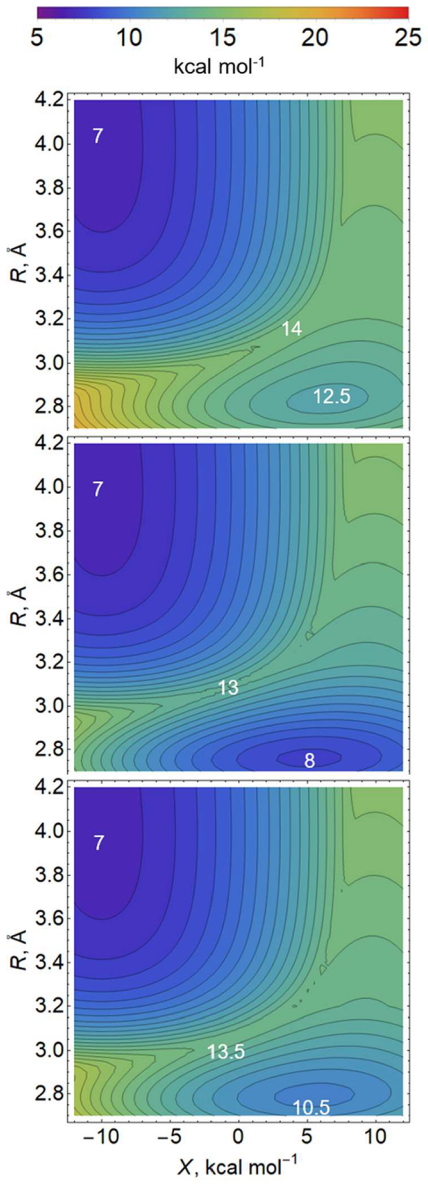

Figure 36. Two-dimensional ground vibronic state free energy surfaces as functions of R and X computed at T = 298 K and E = −0.42 V vs RHE, using the d-band and sp-band electronic coupling parameters V_d = 60, V_{sp} = 20 (top), V_d = 65, V_{sp} = 20 (center), and V_d = 60, V_{sp} = 30 (bottom) kcal mol^{-1}. Figure reproduced with permission from ref 365. Copyright 2019 American Chemical Society.

diabatization of the two lowest double adiabatic vibronic states within the adiabatic model. These two diabatic vibronic states correspond to the lowest two proton vibrational states on the ground electronic potential energy surface. Landau−Zener theory[379,380] allows the natural interpolation between the adiabatic and nonadiabatic limits as the magnitude of the vibronic coupling between the reactant and product states decreases. The effects of solvent dynamics have also been included in this model in the framework of the stable-states picture of chemical reactivity.[367,381]

In this formulation, the rate constant for proton discharge at a given distance R between the proton donor and the electrode surface was expressed as

$$k(R) = \frac{c_{HA^+}(R \to \infty)}{c_{HA^+}(R)} \nu(R) \exp\left[-\frac{\Delta G_{eff}^{\neq}}{k_B T}\right] \quad (37)$$

where the first factor is the ratio of the concentration of the proton donor in bulk solvent and at distance R, and $\Delta G_{eff}^{\neq}$ is the effective activation free energy that includes the work term needed to bring the acid from the bulk solution to a distance R from the electrode. The effective prefactor $\nu(R)$ includes the effects of vibrational nonadiabaticity and solvent dynamics:[43]

$$\nu(R) = \left[\frac{1}{\nu^{LZ}(R)} + \frac{1}{\nu^{SC}(R)}\right]^{-1} \quad (38)$$

The Landau−Zener frequency factor $\nu^{LZ}(R)$ is obtained by averaging the total Landau−Zener transition probability over the thermal Maxwell−Boltzmann distribution of velocities at the crossing point (see eqs 8 and 9 in ref 43 for the explicit expression). This factor accounts for multiple recrossings at the crossing point and thus naturally describes both the nonadiabatic (i.e., small vibronic coupling) and adiabatic (i.e., large vibronic coupling) limits as well as the intermediate regime. The factor $\nu^{SC}(R)$ is independent of the vibronic coupling and is inversely proportional to the longitudinal relaxation time τ_L of the solvent. It can be expressed in terms of the reaction free energy ΔG and reorganization energy λ according to[368,371,382,383]

$$\frac{1}{\nu^{SC}} = \tau_L \sqrt{4\pi\lambda k_B T}\left[\frac{1}{|\Delta G + \lambda|} + \frac{1}{|\Delta G - \lambda|}\right] \quad (39)$$

Note that this expression is not valid near the activationless region where $\Delta G = \pm\lambda$.

Thus, the expression for the effective prefactor given in eq 38 covers all magnitudes of the solvent relaxation time and vibronic coupling. Moreover, this expression yields the familiar adiabatic transition state theory prefactor $\omega/2\pi$ and nonadiabatic prefactor proportional to the square of the vibronic coupling in the appropriate limits. Figure 37 illustrates the applicability range of this curve-crossing formulation.

This formulation has been applied to the aqueous Volmer reaction on a gold electrode under acidic conditions (Figure 38).[43] One-dimensional slices along the solvent coordinate of the two lowest adiabatic vibronic free energy surfaces were used in the diabatization procedure performed for each value of the proton donor−acceptor distance. The current densities were computed at each value of the applied potential by integrating the rate constant over the proton donor−acceptor distance, weighting by the concentration of H_3O^+. The calculated transfer coefficients and kinetic isotope effects are in good agreement with experimental data.[384−386] The calculations revealed that both vibrational nonadiabaticity and solvent dynamics play significant roles. The reaction is vibrationally nonadiabatic at large proton donor−acceptor distances, and at shorter distances its rate constant is controlled predominantly by solvent dynamics.

Although it successfully described the Volmer reaction in acidic aqueous solution, this curve crossing formulation has two significant drawbacks. First, it relies on only the two lowest adiabatic vibronic free energy surfaces with an avoided crossing. At low overpotentials or for highly endergonic reactions (e.g., proton discharge on mercury electrodes), the two lowest surfaces might both possess reactant character and not exhibit an avoided crossing, thereby preventing meaningful diabatization.

https://doi.org/10.1021/acs.chemrev.1c00929
Chem. Rev. XXXX, XXX, XXX−XXX

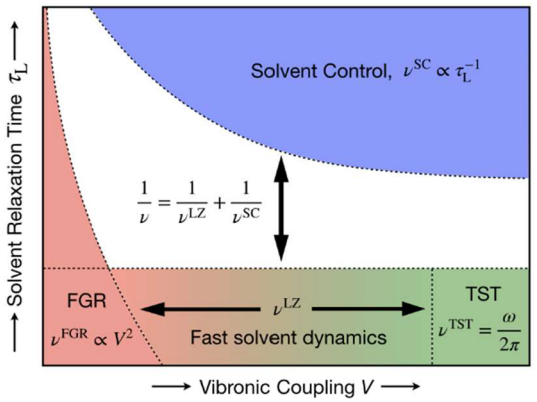

Figure 37. Schematic representation of the unified formulation to account for both nonadiabaticity and solvent dynamics. In the limit of fast solvent dynamics (bottom of figure), the pre-exponent is given by ν^{LZ}, which in the normal region interpolates between the nonadiabatic Fermi's golden rule (FGR) limit ν^{FGR} (bottom left) and the adiabatic transition state theory (TST) limit ν^{TST} (bottom right). In the limit of slow solvent dynamics (top), the pre-exponent is given by ν^{SC}, corresponding to the solvent-controlled regime. Figure reproduced with permission from ref 43. Copyright 2019 American Chemical Society.

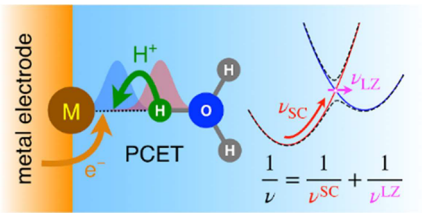

Figure 38. Schematic depiction of the curve-crossing formulation that includes the effects of vibrational nonadiabaticity and solvent dynamics and its application to the Volmer reaction from H_3O^+ to a gold electrode. The free energy curves associated with the two lowest double adiabatic vibronic states (black dashed curves) are diabatized to generate the free energy curves associated with the diabatic vibronic states (red and blue) corresponding to the lowest two proton vibrational states on the ground electronic potential energy surface. The effective prefactor ν is expressed in terms of the Landau–Zener factor ν^{LZ}, which accounts for multiple recrossings at the crossing point, naturally describing both the nonadiabatic and adiabatic limits as well as the intermediate regime, and the solvent-controlled factor ν^{SC}, which is independent of the vibronic coupling and inversely proportional to the longitudinal relaxation time. Figure reproduced with permission from ref 43. Copyright 2019 American Chemical Society.

Inclusion of more excited states in the formulation significantly complicates the diabatization procedure. Second, the presence of the continuum of excited electronic states is neglected. For highly endergonic reactions, the energy gap between the discrete ground electronic state and the continuum of excited states may become very small,[365] requiring consideration of proton vibrational states associated with the electronic states in the continuum. Thus, the development of even more general theoretical frameworks is warranted.

6.5. General Electrochemical PCET Theory in Diabatic Vibronic Representation

In a more general formulation[44] of the Volmer reaction, the proton discharge reaction is described in terms of Landau–Zener transitions at the continuum of crossing points between the free energy curves for the reactant and product vibronic states represented as Marcus parabolas along a collective solvent coordinate. In contrast to the nonadiabatic DKL model,[36,321] however, these transitions are not treated as independent transitions. Instead, the probability of undergoing a transition at a given crossing point is determined not only by the Landau–Zener probability multiplied by the probability of reaching this crossing point due to an equilibrium solvent fluctuation but also by the combined probability of bypassing all of the intermediate crossing points on the way from the reactant minimum. This mechanism is illustrated in Figure 39, where the green circles

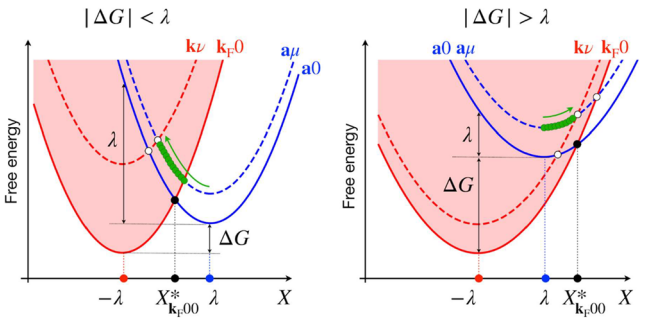

Figure 39. Stacked reactant (blue) and product (red) Marcus parabolas associated with the vibronic states. The reorganization energy λ and the total reaction free energy ΔG defined relative to the Fermi level of the electrode are indicated. The red shaded regions designate the overlapping quasi-continua of the product vibronic states corresponding to the occupied electronic levels of the electrode. The solid red and blue lines correspond to the Marcus parabolas for the ground reactant and product vibronic states, and the dashed lines show the Marcus parabolas for an individual pair of excited reactant and product vibronic states. The black and white circles designate the crossing points at which the nonadiabatic transitions occur. The green circles designate the crossing points that must be bypassed on the way to a given crossing point. Figure reproduced with permission from ref 44. Copyright 2019 American Chemical Society.

designate the crossing points that are bypassed on the way from the minimum of the reactant free energy curve to a given crossing point. A similar treatment of Landau–Zener transitions has also been utilized in Monte Carlo simulations of electrochemical electron transfer processes, where the electrode levels were modeled as a quasi-discrete set of delocalized electronic states.[387]

This formulation utilizes a diabatic representation for the vibronic states involved in electrochemical PCET. In this representation, the reactant and product vibronic states are defined as direct products of the unperturbed diabatic electronic states shown in Figure 35 and the associated proton vibrational states. As pointed out in the context of electrochemical ET,[324,388,389] the nonadiabatic treatment based on Fermi's golden rule, where the reaction is described in terms of nonadiabatic transitions at the crossing points between the unperturbed electronic state of the redox species and the continuum of unperturbed electronic states in the metal electrode, is justified because of the highly delocalized nature of the electronic states in the metal. Because the normalization factor of the wave functions for these electronic states is inversely proportional to the square root of the volume of the electrode, the electronic coupling between the electronic state of the redox species and any individual electronic state in the metal is very small for macroscopic electrodes. These small electronic couplings justify the use of perturbation theory for describing

https://doi.org/10.1021/acs.chemrev.1c00929
Chem. Rev. XXXX, XXX, XXX–XXX

the nonradiative transitions.[44,324,388,389] In the case of PCET, the assumption of small vibronic couplings is even better justified because of the typically small overlaps between the reactant and product proton vibrational wave functions. This treatment is analogous to Sumi's treatment of free carrier capture by deep-level defect electronic states in semiconductors[369] but is based on the vibronic representation of the active states.

In this formulation, the delocalized electronic states in the metal electrode are used as a convenient basis of single-particle states of quasi-free electrons in the metal for the construction of the reactant and product states in the PCET reaction. The main advantage of this basis is that the individual electronic couplings (i.e., the matrix elements of the Hamiltonian between the one-electron state of the redox species and these delocalized quasi-free electron states in the metal) are small by construction, allowing the use of a truncated expansion of the exponential in the Landau−Zener expression for the transition probabilities. In general, the results do not depend on the choice of the basis. Moreover, the strength of the electronic coupling that determines the adiabatic or nonadiabatic behavior of the overall PCET reaction is associated with the coupling between the electronic state of the redox species and an orbital localized at the active site of the electrode.

In the general PCET formulation,[44] the total reaction probability for a given crossing point between one of the reactant vibronic states μ and a product vibronic state $\mathbf{k}\nu$, with $\mathbf{k}$ denoting the electronic state in the metal electrode, is given by

$$\Upsilon_{\mathbf{k}\mu\nu} = f_{\mathbf{k}} P_{\mathbf{k}\mu\nu} \prod_{\mathbf{k}'\nu'} [1 - f_{\mathbf{k}'} P_{\mathbf{k}'\mu\nu'}] \tag{40}$$

Here $f_{\mathbf{k}}$ is the discrete Fermi distribution giving the probability of the electrode level $\mathbf{k}$ being occupied, and $P_{\mathbf{k}\mu\nu}$ are the Landau−Zener nonadiabatic transition probabilities. Explicitly accounting for the nonreactive bypassed crossings has very important consequences. Even when the vibronic couplings between individual reactant and product vibronic states are small and the individual transitions are nonadiabatic, this treatment ensures the emergence of adiabatic behavior for the overall reaction in the appropriate limit, as demonstrated for the case of electrochemical ET.[388]

The final rate constant expression derived in ref 44 after averaging over equilibrium distributions of the solvent coordinate and corresponding velocity has the following integral form:

$$k^{\mathrm{LZ}} = \frac{2\pi}{\hbar} \sum_{\mu} w_{\mu} \int_{-\infty}^{\infty} \mathrm{d}\varepsilon \bar{\Delta}_{\mu}(\varepsilon) W_{\mu 0}(\varepsilon) \int_{-\infty}^{\infty} \mathrm{d}\dot{X}\, M(\dot{X}) \times \theta[\mathrm{sign}(\dot{X})(\varepsilon - \Gamma_{\mu 0})] \exp\left[-\frac{2\pi}{\hbar |\dot{X}|} \left| \int_{\varepsilon}^{\Gamma_{\mu 0}} \mathrm{d}\varepsilon' \bar{\Delta}_{\mu}(\varepsilon') \right| \right] \tag{41}$$

Here $W_{\mu\nu}(\varepsilon)$ is the probability of sampling a crossing point for a given electrode level with energy ε and reactant and product proton vibrational states μ and ν, $M(\dot{X})$ is the Maxwell distribution function for velocities along the solvent coordinate X, and $\theta[\ldots]$ is the Heaviside step function. The very important quantity $\bar{\Delta}_{\mu}(\varepsilon)$ characterizes the strength of the vibronic couplings. This quantity is a cumulative weighted density of states (CWDOS) for the occupied levels of the electrode and is given by

$$\bar{\Delta}_{\mu}(\varepsilon) = \sum_{\alpha} |S_{\mu\alpha}|^2 f(\varepsilon + E_{\alpha}) \Delta(\varepsilon + E_{\alpha}) \tag{42}$$

where $S_{\mu\alpha}$ is the overlap integral for the reactant and product proton vibrational states μ and α, $f(\varepsilon)$ is the Fermi distribution function for the electrode, E_{α} is the energy of proton vibrational state α relative to the ground state proton vibrational energy for the product, and $\Delta(\varepsilon)$ is the WDOS for the electrode defined in eq 34.

The general rate constant expression in eq 41 smoothly interpolates between the limits of weak and strong coupling, as characterized by the magnitude of the WDOS integrated over the entire electronic band of the electrode. In the weak coupling or nonadiabatic limit, the rate constant expression reduces to half of the nonadiabatic rate constant expression in the DKL model.[36] In the opposite strong coupling or adiabatic limit, the rate constant becomes independent of the coupling strength (i.e., Δ does not appear in the limiting expression) and reaches the adiabatic limit of transition state theory. It is interesting to note that in the case when the electronic band of the electrode extends over a broad range of energies below and above the Fermi level (i.e., the extended band case) the adiabatic limit is characterized by zero activation barrier with a prefactor doubled relative to conventional transition state theory. The effects of solvent dynamics were also included using a separate interpolation scheme based on the stable-states picture of chemical reactivity,[367,381] analogously to the curve-crossing formulation described in the previous subsection.[43]

This general formulation was applied to the reaction of proton discharge on a gold electrode in alkaline aqueous solution.[44] The proposed mechanism of this reaction, where the role of the proton donor is played by a water dimer in the compact layer near the electrode surface, is shown in Figure 40A. The calculated Tafel plots and kinetic isotope effects are in qualitative agreement with experimental measurements by Sakaushi.[386] A comparison of the calculated and measured kinetic isotope effects as functions of applied potential is given in Figure 40B. The unusual decrease of the kinetic isotope effect with increasing applied potential observed experimentally was explained in terms of increasing contributions to the current density from the excited reactant proton vibrational states. The overlap integrals associated with the excited reactant proton vibrational states are larger and less isotope-dependent. The origin of this potential-dependent kinetic isotope effect is the same as the origin of the experimentally observed potential-dependent kinetic isotope effect for the Volmer reaction from triethylammonium acid to a gold electrode in acetonitrile,[216] as discussed in section 6.2. Thus, this physical explanation was obtained with two different theoretical formulations applied to two different Volmer reactions.

In general, proton tunneling is a characteristic of electrochemical PCET in acidic and alkaline aqueous solution as well as other solvents such as acetonitrile. The formalism based on the diabatic vibronic representation inherently includes zero-point energy and tunneling of the transferring proton(s). Within this framework, the magnitude of the kinetic isotope effect and its potential dependence are determined mainly by the relative contributions from excited vibronic states and their associated vibrational wave function overlaps.

6.6. Grand Canonical Formulations of Electrochemical Rate Theory

The most distinct feature of electrochemical reactions is the presence of the electrode kept under constant applied potential.

https://doi.org/10.1021/acs.chemrev.1c00929
Chem. Rev. XXXX, XXX, XXX−XXX

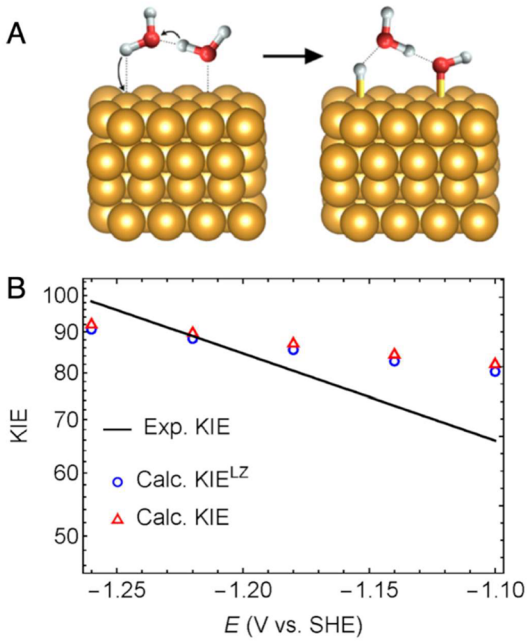

Figure 40. (A) Schematic illustration of the mechanism for the elementary act of the Volmer reaction on a gold surface in alkaline solution.[44] The Au atoms are depicted with bronze spheres, and the oxygen and hydrogen atoms are depicted with red and gray spheres, respectively. Adapted with permission from ref 44. Copyright 2021 American Chemical Society. (B) Comparison of potential dependent kinetic isotope effects measured experimentally[386] (solid black line) and calculated[44] using the general Landau−Zener expression in eq 41 (blue circles), and the expression interpolating between the Landau−Zener regime and the solvent-controlled regime (red triangles). Figure reproduced with permission from ref 44. Copyright 2020 American Chemical Society.

The applied potential controls the chemical potential of the electrons in the electrode and thus directly affects the thermodynamics and kinetics of electrochemical reactions. The system under constant applied potential can be viewed as an open system in contact with a large external reservoir of electrons (i.e., a potentiostat), and thus its thermodynamics can be rigorously described within the formalism of the grand canonical ensemble (GCE). The GCE framework for thermodynamics of electrochemical systems has been relatively well developed and has been used in conjunction with DFT to model electrocatalytic systems at constant electrode potential and at constant chemical potentials of ions in solution.[73,102,107,111,113,114,119,122,172,181,227,390]

The rate theory of electrochemical reactions has also been recently formulated in the GCE framework.[45,115,391] The straightforward generalization of the rate theory for a canonical ensemble (CE)[45] leads to the general expression for the GCE rate constant k^{GCE} for a system at a constant chemical potential μ, volume V, and temperature T as the following GCE average over systems with different numbers of particles N

$$k^{GCE}(\mu, V, T)\Xi_0 = \sum_{N=0}^{\infty} \exp\left[\frac{\mu N}{k_B T}\right] k^{CE}(N, V, T)Q_0 \tag{43}$$

where Ξ_0 and Q_0 are the initial state GCE and CE total partition functions, respectively, and k^{CE} is the CE rate constant defined for a system at constant volume V, temperature T, and number of particles N. This expression implies that all of the rate constants derived within the formalism of a CE can be generalized to the GCE by simply performing the GCE average.

The input quantities for the GCE versions of adiabatic TST rate constants, nuclear tunneling corrections, and rate constants of nonadiabatic electrochemical reactions can be extracted directly from DFT calculations in the GCE framework.[45,113] The constrained DFT methodology[301] in conjunction with a GCE formulation of the two-state model for PCET reactions has been applied to the adiabatic Volmer reaction at a gold electrode (Figure 41).[45] This application demonstrates the power of the approach and its applicability to study other electrocatalytic reactions at the electrode−solution interface using first-principles methods.

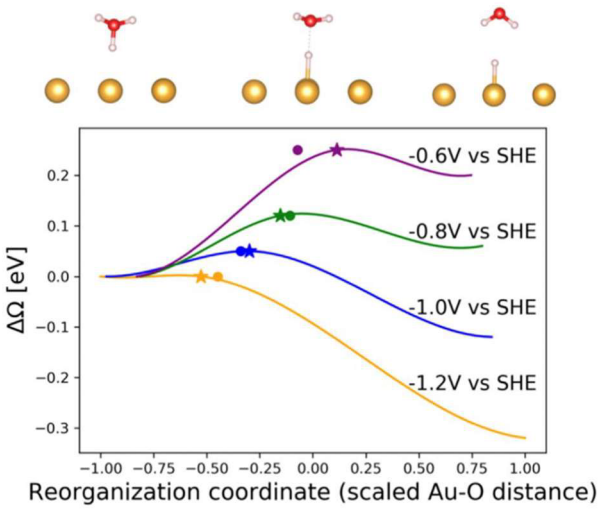

Figure 41. Grand potential along the reaction pathway for the Volmer reaction at a gold electrode at different applied potentials calculated using the GCE constrained DFT methodology in ref 45. Figure reproduced with permission from ref 45. Copyright 2019 IOP Publishing Limited.

7. KINETIC MODELING AND VOLTAMMETRY FOR ELECTROCHEMICAL PCET

7.1. Microkinetic Modeling of Electrocatalytic PCET Processes

Competing chemical and electrochemical steps determine the dominant mechanisms of electrocatalysts and their selectivity toward desired products. Because PCET reactions are the elementary steps in many electrocatalytic reactions, the methodologies used to calculate PCET thermodynamics and kinetics can be applied toward the analysis of more complex catalytic reactions. Moreover, microkinetic modeling studies have found utility in connecting computational insights to experimental observables for multistep reaction mechanisms. In this subsection, we will briefly outline some examples that provide key mechanistic insights into critical electrochemical reactions, as well as their connections to experimental observables.

Calculated potential-dependent PCET reaction free energies and barriers can be used in microkinetic models[392−395] to quantify experimental observables such as reaction orders and apparent activation energies, as well as to identify rate- and selectivity-determining steps in catalytic mechanisms.[396−398] A

https://doi.org/10.1021/acs.chemrev.1c00929
Chem. Rev. XXXX, XXX, XXX−XXX

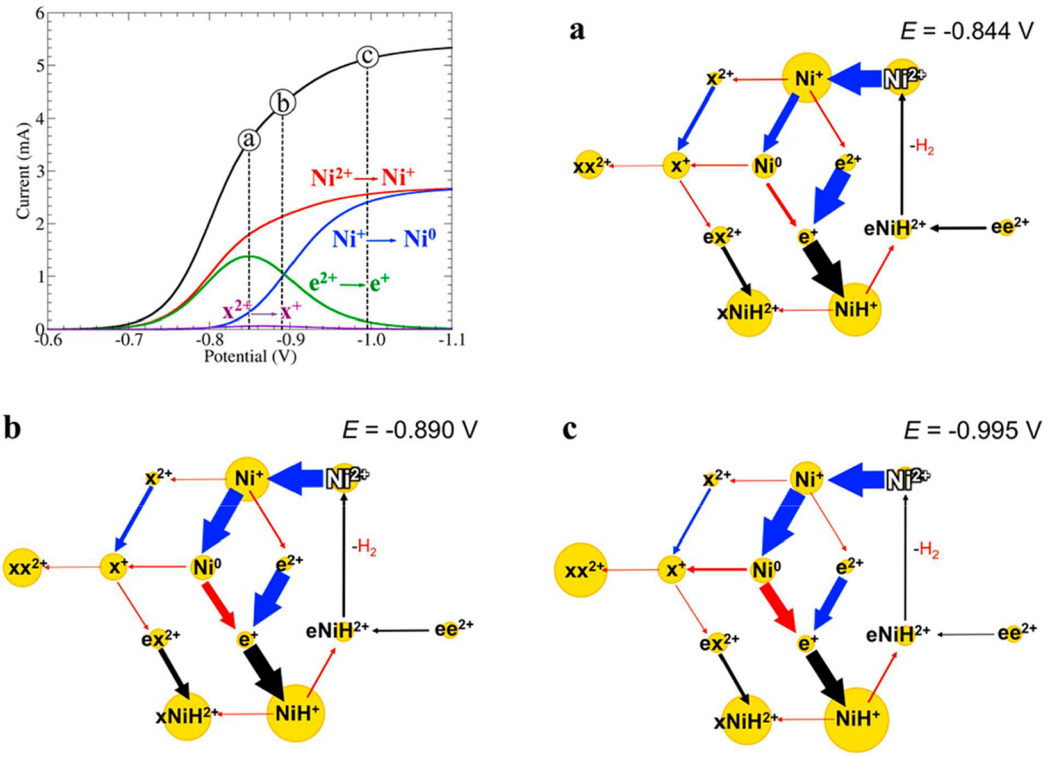

Figure 42. Results of a microkinetic model and CV simulations for hydrogen evolution using $Ni(N_2P_2)_2$ electrocatalysts. (Top left) The current in the simulated CV is deconvoluted into elementary redox reactions. Panels (a), (b), and (c) show the dominant concentrations of reaction intermediates and reaction fluxes at each of the potentials labeled in the simulated CV. The radius of the yellow circles and thickness of the arrows are proportional to the logarithm of the intermediate mole fraction and the reaction flux, respectively. Blue, red, and black arrows correspond to electron transfer, intermolecular proton transfer, and intramolecular proton reorganization and H_2 elimination, respectively. Figure reproduced with permission from ref 399. Copyright 2015 American Chemical Society.

microkinetic model using first-principles calculations as input was used to describe the homogeneous electrochemical production of hydrogen by the $Ni(P_2N_2)_2$ electrocatalysts shown in Figure 42.[399] This model reproduced the experimentally observed turnover rate as a function of acid concentration and applied potential and provided insights into the thermodynamically and kinetically preferred reaction pathways.

In an analysis of the HER on Pt(111), a microkinetic model using potential-dependent reaction free energies and barriers was used to gain a deeper understanding of the reaction kinetics.[112] In contrast to previous explanations for the optimal HER activity of Pt based on an optimal thermoneutral H binding free energy at hollow sites,[63] the microkinetic model demonstrated that the adsorbed hydrogens at the top of the HER volcano are inert. Instead, weaker binding top-site hydrogens have much lower barriers in the dominant Tafel pathway. However, the reactivity of different adsorbed hydrogens and the validity of the H* binding free energy remains a subject of debate for further exploration.[400]

Kinetic modeling studies have also been used to understand the Tafel slopes (i.e., the relationship between applied potential and the log of the current) as well as other experimental observables of electrochemical reactions. A microkinetic analysis of the ORR on Pt was performed using as a baseline a simplified mechanistic analysis assuming a single rate-limiting step at low adsorbate coverage. Combined with a Pourbaix diagram derived from periodic DFT calculations, a change in the ORR Tafel slope from −60 mV/dec at low overpotentials to −120 mV/dec at high overpotentials was determined to be due to the availability of bare surface sites for the initial PCET to O_2 rather than a change in the rate-limiting step (Figure 43A).[401] Similar microkinetic analyses of ORR were performed on different metal electrode surfaces using periodic DFT inputs to further understand pH-dependent Tafel slopes.[402]

Another approach has been to combine periodic DFT calculations with kinetic Monte Carlo simulations to analyze the mechanism of NO electroreduction on Pt(100).[175] The kinetic Monte Carlo simulations were first used to simulate the voltammetric stripping profile of adsorbed NO, which is reduced through five PCET steps to form NH_4^+, achieving close agreement with experimental measurements (Figure 43B). The mechanistic details embedded in this curve were extracted through multiple kinetic Monte Carlo simulations to determine the most probable pathways of NO electroduction.[175] Recent studies have used ion reorganization energies and Marcus work terms as fit parameters in microkinetic models, which have helped elucidate the impact of applied potential, pH, and O_2 partial pressure on oxygen evolution kinetics.[403,404]

In future studies, such analyses of heterogeneous electrocatalytic reactions can be combined with PCET rate constant calculations for the elementary steps. Incorporation of vibronically nonadiabatic effects in these PCET rate constant calculations could find utility in discerning reaction mechanisms wherein nuclear quantum effects are observed. For example, significant kinetic isotope effects have been observed experimentally for reactions such as ORR[385,406,407] and HER.[408] These experimental observations could be combined with

https://doi.org/10.1021/acs.chemrev.1c00929
Chem. Rev. XXXX, XXX, XXX−XXX

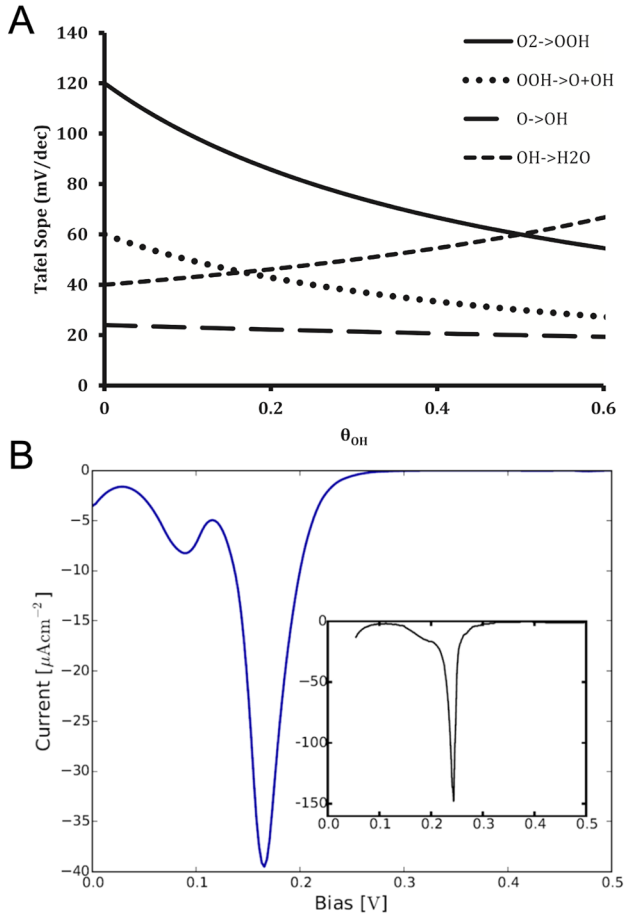

Figure 43. (A) Tafel slope as a function of OH adsorbate coverage θ_{OH} for different rate-limiting steps as determined from a microkinetic model for ORR on Pt(111). Panel reproduced with permission from ref 401. Copyright 2012 Electrochemical Society. (B) Voltammetric profile for proton-coupled reductive stripping of adsorbed NO on Pt(100). The blue profile was simulated using kinetic Monte Carlo, and the inset is the experimentally measured[405] stripping profile. Panel reproduced with permission from ref 175. Copyright 2017 American Chemical Society.

electronic structure calculations, nonadiabatic PCET theory, and microkinetic modeling to gain further insights into complex electrocatalytic reaction networks involving several PCET steps.

7.2. Simulating Voltammograms for PCET Processes

A wide range of methods have been developed to simulate cyclic voltammograms for electrochemical processes.[409−412] Rather than attempt to review this vast field, we describe a single example of how such simulations can be performed in conjunction with concepts from the vibronically nonadiabatic PCET theory described in section 5.2. Current−potential profiles obtained from linear voltammetric sweeps were simulated using a generalized Anderson−Holstein model for PCET with a quantized proton coordinate.[413] The classical master equation, which included an embedded quantum classical Liouville equation, was solved by combining diffusion of the reactant and product species in solution and surface hopping between vibronic states. The nuclear quantum effects were found to impact the voltammograms to a minor extent, and kinetic isotope effects were observed for the peak potentials but not the peak currents. Combining these current−voltage simulation methods with more accurate potential energy surfaces obtained from first-principles calculations could strengthen their predictive power and lead to further mechanistic insights.

8. REMAINING CHALLENGES AND FUTURE DIRECTIONS

Despite significant advances, many challenges must still be overcome in efforts to model and simulate electrochemical PCET. The quantum mechanical treatment of the transferring protons is important for a complete description of PCET reactions. Adding zero-point energy and hydrogen tunneling corrections to conventional electronic structure calculations is often inadequate. Quantization of the transferring protons with multicomponent quantum chemistry methods, such as the nuclear-electronic orbital (NEO) approach[414,415] or path integral methods,[416] is computationally challenging for electrochemical systems, although such calculations are becoming more tractable. In addition, the majority of homogeneous electrochemical PCET reactions are expected to be vibronically nonadiabatic. Traditional adiabatic methods such as transition state theory are unlikely to be applicable to such reactions.

The vibronically nonadiabatic PCET theory[27] provides an accurate description of a wide range of homogeneous electrochemical PCET reactions, utilizing a general form of the vibronic coupling to span the range of electronically adiabatic and nonadiabatic proton transfer. The input quantities to the vibronically nonadiabatic PCET rate constant expressions include reorganization energies, proton potential energy curves, and electronic couplings. These quantities can be computed with electronic structure methods combined with other approaches described within this review. Each of these methods, however, has underlying approximations limiting the quantitative accuracy of the computed electrochemical rate constants and current densities.

Heterogeneous electrochemical PCET can span the range of the vibronically adiabatic and nonadiabatic regimes. In some cases, a single system can span both limits because the rate constant is obtained by integrating over all distances between the proton donor or acceptor molecule and the electrode. Thus, a general theoretical framework[44] that spans the vibronically adiabatic and nonadiabatic regimes, as well as the solvent-controlled regime, provides the most reliable approach for these processes. When a specific reaction is known to be adiabatic or nonadiabatic, however, one of the more specialized rate constant expressions may be applicable. As in the homogeneous case, the quantitative calculation of the input quantities to these rate constant expressions can be challenging.

A realistic description of the EDL is required to model both homogeneous and heterogeneous PCET but is especially relevant to the latter because the proton transfer reaction occurs at the surface. Dielectric continuum models of the EDL are advantageous because they inherently include the entropic effects associated with the solvation free energies and do not require conformational sampling. Disadvantages of such models are that they cannot describe hydrogen-bonding interactions between the solvent molecules and the redox molecules and surface, and they do not describe the structure of individual ions at the interface. An explicit molecular description of the solvent and ions at the EDL addresses these issues, but conformational sampling to compute free energies is computationally intensive, particularly with first-principles electronic structure methods. Molecular mechanical force fields alleviate some of this computational expense but introduce errors from the force

https://doi.org/10.1021/acs.chemrev.1c00929
Chem. Rev. XXXX, XXX, XXX−XXX

fields, and reactive force fields are necessary to model chemical reactions such as PCET.

Other challenges arise for the description of the electrode surface itself. Often catalysis occurs at defect sites that are not present when the electrode is modeled as a perfect crystal. For electrochemical PCET, determining the active site at which the proton will adsorb is not always straightforward. Thermodynamic analyses, such as computational phase and Pourbaix diagrams, are useful computational approaches to characterize the electrode surface structure under reaction conditions but are limited by the underlying assumptions of the models and methods. Moreover, the rigorous implementation of a constant electrode potential typically entails the use of emerging grand canonical methods. The reliability of these various methods for describing the EDL and the electrode surface can be ascertained by direct comparisons to experimental spectroscopic measurements for the systems of interest. This type of feedback between computation and experiment is essential for effective modeling of heterogeneous surfaces.[87,417]

Direct molecular dynamics simulations of electrochemical PCET avoids the use of analytical rate constant expressions and also can provide dynamical information. Such simulations describe the electrode, solvent, ions, and redox molecules at an atomic level. The challenges of applying a constant electrode potential can be overcome by performing these simulations with the grand canonical ensemble (refs 73, 102, 107, 111, 113, 114, 119, 122, 172, 181, 227, and 390). The choice of functional within periodic DFT is not straightforward for these types of simulations because hybrid functionals may be necessary to describe the solvent and redox molecules but may not provide an accurate description of the metal electrode. Further development of functionals that are accurate in both circumstances is an important direction to explore. As mentioned above, the quantization of the protons with the NEO approach or path integral methods is expected to be important for describing electrochemical PCET. The inclusion of nonadiabatic effects through Ehrenfest dynamics[418] or surface hopping dynamics[419] is also expected to be critical in many cases. Furthermore, because these PCET reactions are usually too slow for direct simulation, enhanced sampling methods designed for rare events will be required.

Machine learning methods will also play a role in the field of electrochemical PCET, potentially facilitating the design of effective electrocatalysts.[420−422] Machine learning-based approaches have already been applied toward computational Pourbaix diagram construction,[423] transition state searches on adiabatic surfaces,[424,425] and reactive force field development.[252] Moving forward, machine learning can also be used to facilitate the calculation of PCET rate constants through accelerated predictions of input quantities such as proton vibrational wave functions,[426,427] reorganization energies, or electronic couplings relevant to PCET processes at electrodes. Theoretical models and computational chemistry calculations integrated with machine learning algorithms can help identify new descriptors for electrochemical PCET thermochemistry and rate constants.

In addition to all of these issues, electrochemical PCET is usually part of a larger catalytic process. The coupling of electrochemical PCET to the other catalytic steps requires a more macroscopic approach in the form of kinetic modeling. Similar to the analytical PCET rate constants, the accuracy of a kinetic model relies on the input quantities, which can be computed at various levels of theory. Designing strategies to combine microscopic and macroscopic approaches in a rigorous and physically realistic way will provide insights into these complex catalytic processes. The further development of both theories and computational methods, in conjunction with direct comparison to experimental observables, is essential to progress in this field.

AUTHOR INFORMATION

Corresponding Author

Sharon Hammes-Schiffer − *Department of Chemistry, Yale University, New Haven, Connecticut 06520, United States;* orcid.org/0000-0002-3782-6995; Email: sharon.hammes-schiffer@yale.edu

Authors

Robert E. Warburton − *Department of Chemistry, Yale University, New Haven, Connecticut 06520, United States;* orcid.org/0000-0002-9693-307X

Alexander V. Soudackov − *Department of Chemistry, Yale University, New Haven, Connecticut 06520, United States;* orcid.org/0000-0001-9581-8494

Complete contact information is available at: https://pubs.acs.org/10.1021/acs.chemrev.1c00929

Notes

The authors declare no competing financial interest.

Biographies

Robert E. Warburton received his B.S. in chemical engineering from The Ohio State University and his Ph.D. in chemical engineering from Purdue University under the supervision of Jeffrey Greeley. During graduate school, he also performed research under the supervision of Larry Curtiss at Argonne National Laboratory with the support of a Department of Energy Office of Science Graduate Research (SCGSR) Award. He is currently an Arnold O. Beckman Postdoctoral Fellow in the Hammes-Schiffer group at Yale University. His research is directed at understanding and controlling interfacial processes for applications in energy storage and catalysis using first-principles computational methods.

Alexander V. Soudackov received his B.S. in chemistry and M.Sc. in quantum chemistry from Lomonosov Moscow State University and his Ph.D in physics and mathematics from Karpov Institute of Physical Chemistry in Moscow, Russia. His postdoctoral career included University of Hanover in Germany (Alexander von Humboldt Research Fellowship), University of Notre Dame, and University of Utah. Currently, he is a research scientist in the Chemistry Department at Yale University. His research is focused on the theory of proton-coupled electron transfer reactions in complex environments.

Sharon Hammes-Schiffer received her B.A. from Princeton University and her Ph.D. from Stanford University, followed by two years at AT&T Bell Laboratories. Her academic career progressed from the University of Notre Dame to Pennsylvania State University to the University of Illinois. She is currently the Sterling Professor of Chemistry at Yale University. Her research centers on the investigation of electron, proton, and proton-coupled electron transfer reactions in chemical, biological, and interfacial processes, with particular interests in quantum dynamical and non-Born−Oppenheimer effects. Her work encompasses the development of analytical theories and computational methods, as well as applications to a wide range of experimentally relevant systems.

https://doi.org/10.1021/acs.chemrev.1c00929
Chem. Rev. XXXX, XXX, XXX−XXX

ACKNOWLEDGMENTS

We are grateful for the important contributions to the electrochemical PCET projects from the following group members: Brian Solis, Ben Auer, Samantha Horvath, Laura Fernandez, Michelle Ludlow, Charulatha Venkataraman, Irina Navrotskaya, Soumya Ghosh, Zachary Goldsmith, Yan-Choi Lam, Mioy Huynh, Josh Goings, Max Secor, Phillips Hutchison, and William Lake. The writing of this review was supported as part of the Center for Molecular Electrocatalysis and the Center for Alkaline-Based Energy Solutions, Energy Frontier Research Centers funded by the U.S. Department of Energy, Office of Science, Office of Basic Energy Sciences, as well as supported by the Air Force Office of Scientific Research under AFOSR Award No. FA9550-18-1-0420. R.E.W. acknowledges support from an Arnold O. Beckman Postdoctoral Fellowship.

REFERENCES

(1) Hammes-Schiffer, S. Theoretical Perspectives on Proton-Coupled Electron Transfer Reactions. *Acc. Chem. Res.* **2001**, *34*, 273−281.
(2) Huynh, M. H. V.; Meyer, T. J. Proton-Coupled Electron Transfer. *Chem. Rev.* **2007**, *107*, 5004−5064.
(3) Rosenthal, J.; Nocera, D. G. Role of Proton-Coupled Electron Transfer in O-O Bond Activation. *Acc. Chem. Res.* **2007**, *40*, 543−553.
(4) Costentin, C. Electrochemical Approach to the Mechanistic Study of Proton-Coupled Electron Transfer. *Chem. Rev.* **2008**, *108*, 2145−2179.
(5) Dempsey, J. L.; Brunschwig, B. S.; Winkler, J. R.; Gray, H. B. Hydrogen Evolution Catalyzed by Cobaloximes. *Acc. Chem. Res.* **2009**, *42*, 1995−2004.
(6) Warren, J. J.; Tronic, T. A.; Mayer, J. M. Thermochemistry of Proton-Coupled Electron Transfer Reagents and Its Implications. *Chem. Rev.* **2010**, *110*, 6961−7001.
(7) Hammes-Schiffer, S.; Stuchebrukhov, A. A. Theory of Coupled Electron and Proton Transfer Reactions. *Chem. Rev.* **2010**, *110*, 6939−6960.
(8) Weinberg, D. R.; Gagliardi, C. J.; Hull, J. F.; Murphy, C. F.; Kent, C. A.; Westlake, B. C.; Paul, A.; Ess, D. H.; McCafferty, D. G.; Meyer, T. J. Proton-Coupled Electron Transfer. *Chem. Rev.* **2012**, *112*, 4016−4093.
(9) van der Ham, C. J. M.; Koper, M. T. M.; Hetterscheid, D. G. H. Challenges in Reduction of Dinitrogen by Proton and Electron Transfer. *Chem. Soc. Rev.* **2014**, *43*, 5183−5191.
(10) Bullock, R. M.; Helm, M. L. Molecular Electrocatalysts for Oxidation of Hydrogen Using Earth-Abundant Metals: Shoving Protons around with Proton Relays. *Acc. Chem. Res.* **2015**, *48*, 2017−2026.
(11) Xu, S.; Carter, E. A. Theoretical Insights into Heterogeneous (Photo)Electrochemical Co2 Reduction. *Chem. Rev.* **2019**, *119*, 6631−6669.
(12) Martin, D. J.; Wise, C. F.; Pegis, M. L.; Mayer, J. M. Developing Scaling Relationships for Molecular Electrocatalysis through Studies of Fe-Porphyrin-Catalyzed O2 Reduction. *Acc. Chem. Res.* **2020**, *53*, 1056−1065.
(13) Tyburski, R.; Liu, T.; Glover, S. D.; Hammarström, L. Proton-Coupled Electron Transfer Guidelines, Fair and Square. *J. Am. Chem. Soc.* **2021**, *143*, 560−576.
(14) Wang, F.; Stahl, S. S. Electrochemical Oxidation of Organic Molecules at Lower Overpotential: Accessing Broader Functional Group Compatibility with Electron-Proton Transfer Mediators. *Acc. Chem. Res.* **2020**, *53*, 561−574.
(15) Bullock, R. M.; Chen, J. G.; Gagliardi, L.; Chirik, P. J.; Farha, O. K.; Hendon, C. H.; Jones, C. W.; Keith, J. A.; Klosin, J.; Minteer, S. D.; et al. Using Nature's Blueprint to Expand Catalysis with Earth-Abundant Metals. *Science* **2020**, *369*, No. eabc3183.
(16) Hammes-Schiffer, S. Proton-Coupled Electron Transfer: Classification Scheme and Guide to Theoretical Methods. *Energ Environ. Sci.* **2012**, *5*, 7696−7703.
(17) Schmickler, W.; Santos, E. *Interfacial Electrochemistry*, 2nd ed.; Springer, 1996.
(18) Grimaud, A.; Diaz-Morales, O.; Han, B.; Hong, W. T.; Lee, Y.-L.; Giordano, L.; Stoerzinger, K. A.; Koper, M. T. M.; Shao-Horn, Y. Activating Lattice Oxygen Redox Reactions in Metal Oxides to Catalyse Oxygen Evolution. *Nat. Chem.* **2017**, *9*, 457−465.
(19) Marcus, R. A. On the Theory of Oxidation-Reduction Reactions Involving Electron Transfer. I. *J. Chem. Phys.* **1956**, *24*, 966−978.
(20) Marcus, R. A. On the Theory of Electrochemical and Chemical Electron Transfer Processes. *Can. J. Chem.* **1959**, *37*, 155−163.
(21) Marcus, R. A. On the Theory of Oxidation-Reduction Reactions Involving Electron Transfer. V. Comparison and Properties of Electrochemical and Chemical Rate Constants. *J. Phys. Chem.* **1963**, *67*, 853−857.
(22) Marcus, R. A. Chemical and Electrochemical Electron-Transfer Theory. *Annu. Rev. Phys. Chem.* **1964**, *15*, 155−196.
(23) Marcus, R. A. On the Theory of Electron-Transfer Reactions. Vi. Unified Treatment for Homogeneous and Electrode Reactions. *J. Chem. Phys.* **1965**, *43*, 679−701.
(24) Soudackov, A.; Hammes-Schiffer, S. Multistate Continuum Theory for Multiple Charge Transfer Reactions in Solution. *J. Chem. Phys.* **1999**, *111*, 4672−4687.
(25) Soudackov, A.; Hammes-Schiffer, S. Theoretical Study of Photoinduced Proton-Coupled Electron Transfer through Asymmetric Salt Bridges. *J. Am. Chem. Soc.* **1999**, *121*, 10598−10607.
(26) Soudackov, A.; Hammes-Schiffer, S. Derivation of Rate Expressions for Nonadiabatic Proton-Coupled Electron Transfer Reactions in Solution. *J. Chem. Phys.* **2000**, *113*, 2385−2396.
(27) Hammes-Schiffer, S.; Soudackov, A. V. Proton-Coupled Electron Transfer in Solution, Proteins, and Electrochemistry. *J. Phys. Chem. B* **2008**, *112*, 14108−14123.
(28) Georgievskii, Y.; Stuchebrukhov, A. A. Concerted Electron and Proton Transfer: Transition from Nonadiabatic to Adiabatic Proton Tunneling. *J. Chem. Phys.* **2000**, *113*, 10438−10450.
(29) Skone, J. H.; Soudackov, A. V.; Hammes-Schiffer, S. Calculation of Vibronic Couplings for Phenoxyl/Phenol and Benzyl/Toluene Self-Exchange Reactions: Implications for Proton-Coupled Electron Transfer Mechanisms. *J. Am. Chem. Soc.* **2006**, *128*, 16655−16663.
(30) Soudackov, A.; Hatcher, E.; Hammes-Schiffer, S. Quantum and Dynamical Effects of Proton Donor-Acceptor Vibrational Motion in Nonadiabatic Proton-Coupled Electron Transfer Reactions. *J. Chem. Phys.* **2005**, *122*, 014505.
(31) Venkataraman, C.; Soudackov, A. V.; Hammes-Schiffer, S. Theoretical Formulation of Nonadiabatic Electrochemical Proton-Coupled Electron Transfer at Metal-Solution Interfaces. *J. Phys. Chem. C* **2008**, *112*, 12386−12397.
(32) Horvath, S.; Fernandez, L. E.; Soudackov, A. V.; Hammes-Schiffer, S. Insights into Proton-Coupled Electron Transfer Mechanisms of Electrocatalytic H2 Oxidation and Production. *Proc. National Acad. Sci.* **2012**, *109*, 15663−15668.
(33) Huynh, M. T.; Mora, S. J.; Villalba, M.; Tejeda-Ferrari, M. E.; Liddell, P. A.; Cherry, B. R.; Teillout, A.-L.; Machan, C. W.; Kubiak, C. P.; Gust, D.; et al. Concerted One-Electron Two-Proton Transfer Processes in Models Inspired by the Tyr-His Couple of Photosystem Ii. *ACS Cent. Sci.* **2017**, *3*, 372−380.
(34) Wang, T.; Zhang, Y.; Huang, B.; Cai, B.; Rao, R. R.; Giordano, L.; Sun, S.-G.; Shao-Horn, Y. Enhancing Oxygen Reduction Electrocatalysis by Tuning Interfacial Hydrogen Bonds. *Nat. Catal* **2021**, *4*, 753−762.
(35) Bockris, J. O. M.; Matthews, D. B. Proton Tunneling in the Hydrogen-Evolution Reaction. *J. Chem. Phys.* **1966**, *44*, 298−309.
(36) Dogonadze, R. R.; Kuznetsov, A. M.; Levich, V. G. Theory of Hydrogen-Ion Discharge on Metals: Case of High Overvoltages. *Electrochim. Acta* **1968**, *13*, 1025−1044.
(37) Kharkats, Y. I.; Ulstrup, J. Quantum Theories of Elementary Steps in Electrochemical Hydrogen Evolution Reaction. *J. Electroanal. Chem.* **1975**, *65*, 555−572.

https://doi.org/10.1021/acs.chemrev.1c00929
Chem. Rev. XXXX, XXX, XXX−XXX

(38) Ovchinnikov, A. A.; Benderskii, V. A. Theory of Electrochemical Hydrogen Evolution Reactions. Part I. The Model and Fundamental Relationships. *J. Electroanal. Chem.* **1979**, *100*, 563−582.
(39) Grimminger, J.; Bartenschlager, S.; Schmickler, W. A Model for Combined Electron and Proton Transfer in Electrochemical Systems. *Chem. Phys. Lett.* **2005**, *416*, 316−320.
(40) Wilhelm, F.; Schmickler, W.; Nazmutdinov, R. R.; Spohr, E. A Model for Proton Transfer to Metal Electrodes. *J. Phys. Chem. C* **2008**, *112*, 10814−10826.
(41) Santos, E.; Lundin, A.; Pötting, K.; Quaino, P.; Schmickler, W. Model for the Electrocatalysis of Hydrogen Evolution. *Phys. Rev. B* **2009**, *79*, 235436.
(42) Koper, M. T. M. Theory of the Transition from Sequential to Concerted Electrochemical Proton-Electron Transfer. *Phys. Chem. Chem. Phys.* **2013**, *15*, 1399−1407.
(43) Lam, Y.-C.; Soudackov, A. V.; Hammes-Schiffer, S. Kinetics of Proton Discharge on Metal Electrodes: Effects of Vibrational Nonadiabaticity and Solvent Dynamics. *J. Phys. Chem. Lett.* **2019**, *10*, 5312−5317.
(44) Lam, Y.-C.; Soudackov, A. V.; Hammes-Schiffer, S. Theory of Electrochemical Proton-Coupled Electron Transfer in Diabatic Vibronic Representation: Application to Proton Discharge on Metal Electrodes in Alkaline Solution. *J. Phys. Chem. C* **2020**, *124*, 27309−27322.
(45) Melander, M. M. Grand Canonical Rate Theory for Electrochemical and Electrocatalytic Systems I: General Formulation and Proton-Coupled Electron Transfer Reactions. *J. Electrochem. Soc.* **2020**, *167*, 116518.
(46) Mayer, J. M. Proton-Coupled Electron Transfer: A Reaction Chemist's View. *Annu. Rev. Phys. Chem.* **2004**, *55*, 363−390.
(47) Solis, B. H.; Hammes-Schiffer, S. Proton-Coupled Electron Transfer in Molecular Electrocatalysis: Theoretical Methods and Design Principles. *Inorg. Chem.* **2014**, *53*, 6427−6443.
(48) Roy, L. E.; Jakubikova, E.; Guthrie, M. G.; Batista, E. R. Calculation of One-Electron Redox Potentials Revisited. Is It Possible to Calculate Accurate Potentials with Density Functional Methods? *J. Phys. Chem. A* **2009**, *113*, 6745−6750.
(49) Tissandier, M. D.; Cowen, K. A.; Feng, W. Y.; Gundlach, E.; Cohen, M. H.; Earhart, A. D.; Coe, J. V.; Tuttle, T. R. The Proton's Absolute Aqueous Enthalpy and Gibbs Free Energy of Solvation from Cluster-Ion Solvation Data. *J. Phys. Chem. A* **1998**, *102*, 7787−7794.
(50) Vollmer, J. M.; Curtiss, L. A.; Vissers, D. R.; Amine, K. Reduction Mechanisms of Ethylene, Propylene, and Vinylethylene Carbonates - a Quantum Chemical Study. *J. Electrochem. Soc.* **2004**, *151*, A178−A183.
(51) Kelly, C. P.; Cramer, C. J.; Truhlar, D. G. Aqueous Solvation Free Energies of Ions and Ion-Water Clusters Based on an Accurate Value for the Absolute Aqueous Solvation Free Energy of the Proton. *J. Phys. Chem. B* **2006**, *110*, 16066−16081.
(52) Qi, X. J.; Fu, Y.; Liu, L.; Guo, Q. X. Ab Initio Calculations of Thermodynamic Hydricities of Transition-Metal Hydrides in Acetonitrile. *Organometallics* **2007**, *26*, 4197−4203.
(53) Tsai, M. K.; Rochford, J.; Polyansky, D. E.; Wada, T.; Tanaka, K.; Fujita, E.; Muckerman, J. T. Characterization of Redox States of Ru(Oh(2))(Q)(Tpy)(2+) (Q = 3,5-Di-Tert-Butyl-1,2-Benzoquinone, Tpy = 2,2′:6′,2″-Terpyridine) and Related Species through Experimental and Theoretical Studies. *Inorg. Chem.* **2009**, *48*, 4372−4383.
(54) Casasnovas, R.; Ortega-Castro, J.; Frau, J.; Donoso, J.; Muñoz, F. Theoretical Pkacalculations with Continuum Model Solvents, Alternative Protocols to Thermodynamic Cycles. *Int. J. Quantum Chem.* **2014**, *114*, 1350−1363.
(55) Solis, B. H.; Hammes-Schiffer, S. Substituent Effects on Cobalt Diglyoxime Catalysts for Hydrogen Evolution. *J. Am. Chem. Soc.* **2011**, *133*, 19036−19039.
(56) Solis, B. H.; Hammes-Schiffer, S. Theoretical Analysis of Mechanistic Pathways for Hydrogen Evolution Catalyzed by Cobaloximes. *Inorg. Chem.* **2011**, *50*, 11252−11262.
(57) Raugei, S.; DuBois, D. L.; Rousseau, R.; Chen, S.; Ho, M.-H.; Bullock, R. M.; Dupuis, M. Toward Molecular Catalysts by Computer. *Acc. Chem. Res.* **2015**, *48*, 248−255.
(58) Nørskov, J. K.; Rossmeisl, J.; Logadottir, A.; Lindqvist, L.; Kitchin, J. R.; Bligaard, T.; Jónsson, H. Origin of the Overpotential for Oxygen Reduction at a Fuel-Cell Cathode. *J. Phys. Chem. B* **2004**, *108*, 17886−17892.
(59) Grimminger, J.; Schmickler, W. Dynamics of Combined Electron-and Proton Transfer at Metal Electrodes. *Chem. Phys.* **2007**, *334*, 8−17.
(60) Koper, M. T. Theory of the Transition from Sequential to Concerted Electrochemical Proton-Electron Transfer. *Phys. Chem. Chem. Phys.* **2013**, *15*, 1399−1407.
(61) Katsounaros, I.; Chen, T.; Gewirth, A. A.; Markovic, N. M.; Koper, M. T. Evidence for Decoupled Electron and Proton Transfer in the Electrochemical Oxidation of Ammonia on Pt(100). *J. Phys. Chem. Lett.* **2016**, *7*, 387−392.
(62) Grimaud, A.; Diaz-Morales, O.; Han, B.; Hong, W. T.; Lee, Y. L.; Giordano, L.; Stoerzinger, K. A.; Koper, M. T. M.; Shao-Horn, Y. Activating Lattice Oxygen Redox Reactions in Metal Oxides to Catalyse Oxygen Evolution. *Nat. Chem.* **2017**, *9*, 457−465.
(63) Nørskov, J. K.; Bligaard, T.; Logadottir, A.; Kitchin, J. R.; Chen, J. G.; Pandelov, S.; Stimming, U. Trends in the Exchange Current for Hydrogen Evolution. *J. Electrochem. Soc.* **2005**, *152*, J23.
(64) Greeley, J.; Jaramillo, T. F.; Bonde, J.; Chorkendorff, I. B.; Norskov, J. K. Computational High-Throughput Screening of Electrocatalytic Materials for Hydrogen Evolution. *Nat. Mater.* **2006**, *5*, 909−913.
(65) Greeley, J.; Stephens, I. E.; Bondarenko, A. S.; Johansson, T. P.; Hansen, H. A.; Jaramillo, T. F.; Rossmeisl, J.; Chorkendorff, I.; Norskov, J. K. Alloys of Platinum and Early Transition Metals as Oxygen Reduction Electrocatalysts. *Nat. Chem.* **2009**, *1*, 552−556.
(66) Viswanathan, V.; Hansen, H. A.; Rossmeisl, J.; Norskov, J. K. Unifying the 2e(−) and 4e(−) Reduction of Oxygen on Metal Surfaces. *J. Phys. Chem. Lett.* **2012**, *3*, 2948−2951.
(67) Kulkarni, A.; Siahrostami, S.; Patel, A.; Nørskov, J. K. Understanding Catalytic Activity Trends in the Oxygen Reduction Reaction. *Chem. Rev.* **2018**, *118*, 2302−2312.
(68) Peterson, A. A.; Abild-Pedersen, F.; Studt, F.; Rossmeisl, J.; Norskov, J. K. How Copper Catalyzes the Electroreduction of Carbon Dioxide into Hydrocarbon Fuels. *Energ Environ. Sci.* **2010**, *3*, 1311−1315.
(69) Trasatti, S. The Absolute Electrode Potential - the End of the Story. *Electrochim. Acta* **1990**, *35*, 269−271.
(70) Tripkovic, V.; Björketun, M. E.; Skúlason, E.; Rossmeisl, J. Standard Hydrogen Electrode and Potential of Zero Charge in Density Functional Calculations. *Phys. Rev. B* **2011**, *84*, 115452.
(71) Hörmann, N. G.; Guo, Z.; Ambrosio, F.; Andreussi, O.; Pasquarello, A.; Marzari, N. Absolute Band Alignment at Semiconductor-Water Interfaces Using Explicit and Implicit Descriptions for Liquid Water. *npj Computational Materials* **2019**, *5*, 1−6.
(72) Melander, M.; Wu, T.; Honkala, K., Constant Inner Potential Dft for Modelling Electrochemical Systems under Constant Potential and Bias. *ChemRxiv* **2021**, DOI: 10.33774/chemrxiv-2021-r621x.
(73) Taylor, C. D.; Wasileski, S. A.; Filhol, J.-S.; Neurock, M. First Principles Reaction Modeling of the Electrochemical Interface: Consideration and Calculation of a Tunable Surface Potential from Atomic and Electronic Structure. *Phys. Rev. B* **2006**, *73*, 165402.
(74) Rossmeisl, J.; Chan, K.; Ahmed, R.; Tripkovic, V.; Bjorketun, M. E. Ph in Atomic Scale Simulations of Electrochemical Interfaces. *Phys. Chem. Chem. Phys.* **2013**, *15*, 10321−10325.
(75) Nielsen, M.; Björketun, M. E.; Hansen, M. H.; Rossmeisl, J. Towards First Principles Modeling of Electrochemical Electrode−Electrolyte Interfaces. *Surf. Sci.* **2015**, *631*, 2−7.
(76) Duan, Z.; Henkelman, G. Theoretical Resolution of the Exceptional Oxygen Reduction Activity of Au(100) in Alkaline Media. *ACS Catal.* **2019**, *9*, 5567−5573.
(77) Gerischer, H. Über Den Zusammenhang Zwischen Dem Mechanismus Der Elektrolytischen Wasserstoffabscheidung Und Der Adsorptionsenergie Des Atomaren Wasserstoffs an Verschiedenen Metallen. *Z. Phys. Chem.* **1956**, *8*, 137−153.

AQ

(78) Parsons, R. The Rate of Electrolytic Hydrogen Evolution and the Heat of Adsorption of Hydrogen. *Trans. Faraday Society* **1958**, *54*, 1053−1063.
(79) Trasatti, S. Work Function, Electronegativity, and Electrochemical Behaviour of Metals: Iii. Electrolytic Hydrogen Evolution in Acid Solutions. *Electroanal. Chem. Interfacial Electrochem.* **1972**, *39*, 163−184.
(80) Schmickler, W.; Trasatti, S. Comment on "Trends in the Exchange Current for Hydrogen Evolution. *J. Electrochem. Soc.* **2006**, *153*, L31; *J. Electrochem. Soc.* **2006**, *153*, L31−L32.
(81) Exner, K. S. Does a Thermoneutral Electrocatalyst Correspond to the Apex of a Volcano Plot for a Simple Two-Electron Process? *Angew. Chem., Int. Ed.* **2020**, *59*, 10236−10240.
(82) Lindgren, P.; Kastlunger, G.; Peterson, A. A. A Challenge to the G ∼ 0 Interpretation of Hydrogen Evolution. *ACS Catal.* **2020**, *10*, 121−128.
(83) Goldsmith, Z. K.; Harshan, A. K.; Gerken, J. B.; Voros, M.; Galli, G.; Stahl, S. S.; Hammes-Schiffer, S. Characterization of Nife Oxyhydroxide Electrocatalysts by Integrated Electronic Structure Calculations and Spectroelectrochemistry. *Proc. Natl. Acad. Sci. U.S.A.* **2017**, *114*, 3050−3055.
(84) Warburton, R. E.; Hutchison, P.; Jackson, M. N.; Pegis, M. L.; Surendranath, Y.; Hammes-Schiffer, S. Interfacial Field-Driven Proton-Coupled Electron Transfer at Graphite-Conjugated Organic Acids. *J. Am. Chem. Soc.* **2020**, *142*, 20855−20864.
(85) Jackson, M. N.; Pegis, M. L.; Surendranath, Y. Graphite-Conjugated Acids Reveal a Molecular Framework for Proton-Coupled Electron Transfer at Electrode Surfaces. *ACS Cent. Sci.* **2019**, *5*, 831−841.
(86) Jackson, M. N.; Surendranath, Y. Molecular Control of Heterogeneous Electrocatalysis through Graphite Conjugation. *Acc. Chem. Res.* **2019**, *52*, 3432−3441.
(87) Hammes-Schiffer, S.; Galli, G. Integration of Theory and Experiment in the Modelling of Heterogeneous Electrocatalysis. *Nature Energy* **2021**, *6*, 700−705.
(88) Agarwal, R. G.; Coste, S. C.; Groff, B. D.; Heuer, A. M.; Noh, H.; Parada, G. A.; Wise, C. F.; Nichols, E. M.; Warren, J. J.; Mayer, J. M. Free Energies of Proton-Coupled Electron Transfer Reagents and Their Applications. *Chem. Rev.* **2022**, *122*, 1−49.
(89) Connelly, S. J.; Wiedner, E. S.; Appel, A. M. Predicting the Reactivity of Hydride Donors in Water: Thermodynamic Constants for Hydrogen. *Dalton Trans.* **2015**, *44*, 5933−5938.
(90) Wise, C. F.; Mayer, J. M. Electrochemically Determined O-H Bond Dissociation Free Energies of Nio Electrodes Predict Proton-Coupled Electron Transfer Reactivity. *J. Am. Chem. Soc.* **2019**, *141*, 14971−14975.
(91) Wise, C. F.; Mayer, J. M. Correction to "Electrochemically Determined O−H Bond Dissociation Free Energies of Nio Electrodes Predict Proton-Coupled Electron Transfer Reactivity. *J. Am. Chem. Soc.* **2020**, *142*, 12544−12545.
(92) Warburton, R. E.; Mayer, J. M.; Hammes-Schiffer, S. Proton-Coupled Defects Impact O−H Bond Dissociation Free Energies on Metal Oxide Surfaces. *J. Phys. Chem. Lett.* **2021**, *12*, 9761−9767.
(93) Lozovoi, A. Y.; Alavi, A.; Kohanoff, J.; Lynden-Bell, R. M. Ab Initio Simulation of Charged Slabs at Constant Chemical Potential. *J. Chem. Phys.* **2001**, *115*, 1661−1669.
(94) Lozovoi, A. Y.; Alavi, A. Reconstruction of Charged Surfaces: General Trends and a Case Study of Pt(110) and Au(110). *Phys. Rev. B* **2003**, *68*, 245416.
(95) Schwarz, K.; Sundararaman, R. The Electrochemical Interface in First-Principles Calculations. *Surf. Sci. Rep.* **2020**, *75*, 100492.
(96) Filhol, J. S.; Neurock, M. Elucidation of the Electrochemical Activation of Water over Pd by First Principles. *Angew. Chem., Int. Ed.* **2006**, *45*, 402−406.
(97) Rossmeisl, J.; Norskov, J. K.; Taylor, C. D.; Janik, M. J.; Neurock, M. Calculated Phase Diagrams for the Electrochemical Oxidation and Reduction of Water over Pt(111). *J. Phys. Chem. B* **2006**, *110*, 21833−21839.
(98) Janik, M. J.; Taylor, C. D.; Neurock, M. First-Principles Analysis of the Initial Electroreduction Steps of Oxygen over Pt(111). *J. Electrochem. Soc.* **2009**, *156*, B126−B135.
(99) Yeh, K. Y.; Janik, M. J. Density Functional Theory-Based Electrochemical Models for the Oxygen Reduction Reaction: Comparison of Modeling Approaches for Electric Field and Solvent Effects. *J. Comput. Chem.* **2011**, *32*, 3399−3408.
(100) Skulason, E.; Karlberg, G. S.; Rossmeisl, J.; Bligaard, T.; Greeley, J.; Jonsson, H.; Norskov, J. K. Density Functional Theory Calculations for the Hydrogen Evolution Reaction in an Electrochemical Double Layer on the Pt(111) Electrode. *Phys. Chem. Chem. Phys.* **2007**, *9*, 3241−3250.
(101) Freysoldt, C.; Neugebauer, J.; Van de Walle, C. G. Electrostatic Interactions between Charged Defects in Supercells. *Phys. Status Solidi B* **2011**, *248*, 1067−1076.
(102) Surendralal, S.; Todorova, M.; Finnis, M. W.; Neugebauer, J. First-Principles Approach to Model Electrochemical Reactions: Understanding the Fundamental Mechanisms Behind Mg Corrosion. *Phys. Rev. Lett.* **2018**, *120*, 246801.
(103) Cheng, J.; Sprik, M. The Electric Double Layer at a Rutile Tio(2) Water Interface Modelled Using Density Functional Theory Based Molecular Dynamics Simulation. *J. Phys.: Condens. Matter* **2014**, *26*, 244108.
(104) Rossmeisl, J.; Skulason, E.; Bjorketun, M. E.; Tripkovic, V.; Norskov, J. K. Modeling the Electrified Solid-Liquid Interface. *Chem. Phys. Lett.* **2008**, *466*, 68−71.
(105) Otani, M.; Sugino, O. First-Principles Calculations of Charged Surfaces and Interfaces: A Plane-Wave Nonrepeated Slab Approach. *Phys. Rev. B* **2006**, *73*, 115407.
(106) Otani, M.; Hamada, I.; Sugino, O.; Morikawa, Y.; Okamoto, Y.; Ikeshoji, T. Electrode Dynamics from First Principles. *J. Phys. Soc. Jpn.* **2008**, *77*, 024802.
(107) Hörmann, N. G.; Andreussi, O.; Marzari, N. Grand Canonical Simulations of Electrochemical Interfaces in Implicit Solvation Models. *J. Chem. Phys.* **2019**, *150*, 041730.
(108) Hörmann, N. G.; Marzari, N.; Reuter, K. Electrosorption at Metal Surfaces from First Principles. *npj Computational Materials* **2020**, *6*, 1−10.
(109) Gauthier, J. A.; Ringe, S.; Dickens, C. F.; Garza, A. J.; Bell, A. T.; Head-Gordon, M.; Nørskov, J. K.; Chan, K. Challenges in Modeling Electrochemical Reaction Energetics with Polarizable Continuum Models. *ACS Catal.* **2019**, *9*, 920−931.
(110) Gauthier, J. A.; Dickens, C. F.; Heenen, H. H.; Vijay, S.; Ringe, S.; Chan, K. Unified Approach to Implicit and Explicit Solvent Simulations of Electrochemical Reaction Energetics. *J. Chem. Theory Comput.* **2019**, *15*, 6895−6906.
(111) Kastlunger, G.; Lindgren, P.; Peterson, A. A. Controlled-Potential Simulation of Elementary Electrochemical Reactions: Proton Discharge on Metal Surfaces. *J. Phys. Chem. C* **2018**, *122*, 12771−12781.
(112) Lindgren, P.; Kastlunger, G.; Peterson, A. A. A Challenge to the G Similar to 0 Interpretation of Hydrogen Evolution. *ACS Catal.* **2020**, *10*, 121−128.
(113) Melander, M. M.; Kuisma, M. J.; Christensen, T. E. K.; Honkala, K. Grand-Canonical Approach to Density Functional Theory of Electrocatalytic Systems: Thermodynamics of Solid-Liquid Interfaces at Constant Ion and Electrode Potentials. *J. Chem. Phys.* **2019**, *150*, 041706.
(114) Sundararaman, R.; Goddard, W. A.; Arias, T. A. Grand Canonical Electronic Density-Functional Theory: Algorithms and Applications to Electrochemistry. *J. Chem. Phys.* **2017**, *146*, 114104.
(115) Melander, M. M. Grand Canonical Ensemble Approach to Electrochemical Thermodynamics, Kinetics, and Model Hamiltonians. *Curr. Opin Electrochem* **2021**, *29*, 100749.
(116) Filhol, J.-S.; Doublet, M.-L. An Ab Initio Study of Surface Electrochemical Disproportionation: The Case of a Water Monolayer Adsorbed on a Pd(111) Surface. *Catal. Today* **2013**, *202*, 87−97.

https://doi.org/10.1021/acs.chemrev.1c00929
Chem. Rev. XXXX, XXX, XXX−XXX

(117) Bonnet, N.; Dabo, I.; Marzari, N. Chemisorbed Molecules under Potential Bias: Detailed Insights from First-Principles Vibrational Spectroscopies. *Electrochim. Acta* **2014**, *121*, 210−214.
(118) Steinmann, S. N.; Michel, C.; Schwiedernoch, R.; Sautet, P. Impacts of Electrode Potentials and Solvents on the Electroreduction of Co 2: A Comparison of Theoretical Approaches. *Phys. Chem. Chem. Phys.* **2015**, *17*, 13949−13963.
(119) Hutchison, P.; Warburton, R. E.; Soudackov, A. V.; Hammes-Schiffer, S. Multicapacitor Approach to Interfacial Proton-Coupled Electron Transfer Thermodynamics at Constant Potential. *J. Phys. Chem. C* **2021**, *125*, 21891−21901.
(120) Petrosyan, S. A.; Rigos, A. A.; Arias, T. A. Joint Density-Functional Theory: Ab Initio Study of Cr2o3 Surface Chemistry in Solution. *J. Phys. Chem. B* **2005**, *109*, 15436−15444.
(121) Gunceler, D.; Letchworth-Weaver, K.; Sundararaman, R.; Schwarz, K. A.; Arias, T. A. The Importance of Nonlinear Fluid Response in Joint Density-Functional Theory Studies of Battery Systems. *Modell. Simul. Mater. Sci. Eng.* **2013**, *21*, 074005.
(122) Letchworth-Weaver, K.; Arias, T. A. Joint Density Functional Theory of the Electrode-Electrolyte Interface: Application to Fixed Electrode Potentials, Interfacial Capacitances, and Potentials of Zero Charge. *Phys. Rev. B* **2012**, *86*, 075140.
(123) Sundararaman, R.; Letchworth-Weaver, K.; Arias, T. A. A Computationally Efficacious Free-Energy Functional for Studies of Inhomogeneous Liquid Water. *J. Chem. Phys.* **2012**, *137*, 044107.
(124) Sundararaman, R.; Schwarz, K. A.; Letchworth-Weaver, K.; Arias, T. A. Spicing up Continuum Solvation Models with Salsa: The Spherically Averaged Liquid Susceptibility Ansatz. *J. Chem. Phys.* **2015**, *142*, 054102.
(125) Sundararaman, R.; Figueiredo, M. C.; Koper, M. T. M.; Schwarz, K. A. Electrochemical Capacitance of Co-Terminated Pt(111) Dominated by the Co-Solvent Gap. *J. Phys. Chem. Lett.* **2017**, *8*, 5344−5348.
(126) Kim, D.; Shi, J.; Liu, Y. Substantial Impact of Charge on Electrochemical Reactions of Two-Dimensional Materials. *J. Am. Chem. Soc.* **2018**, *140*, 9127−9131.
(127) Ge, A.; Kastlunger, G.; Meng, J.; Lindgren, P.; Song, J.; Liu, Q.; Zaslavsky, A.; Lian, T.; Peterson, A. A. On the Coupling of Electron Transfer to Proton Transfer at Electrified Interfaces. *J. Am. Chem. Soc.* **2020**, *142*, 11829−11834.
(128) Delley, M. F.; Nichols, E. M.; Mayer, J. M. Interfacial Acid-Base Equilibria and Electric Fields Concurrently Probed by in Situ Surface-Enhanced Infrared Spectroscopy. *J. Am. Chem. Soc.* **2021**, *143*, 10778−10792.
(129) Rizo, R.; Sitta, E.; Herrero, E.; Climent, V.; Feliu, J. M. Towards the Understanding of the Interfacial Ph Scale at Pt(111) Electrodes. *Electrochim. Acta* **2015**, *162*, 138−145.
(130) Kamyabi, M. A.; Martínez-Hincapié, R.; Feliu, J. M.; Herrero, E. Effects of the Interfacial Structure on the Methanol Oxidation on Platinum Single Crystal Electrodes. *Surfaces* **2019**, *2*, 177−192.
(131) Pourbaix, M. *Atlas of Electrochemical Equilibria in Aqueous Solutions*; National Association of Corrosion Engineers: Houston, TX, 1974.
(132) Horvath, S.; Fernandez, L. E.; Appel, A. M.; Hammes-Schiffer, S. Ph-Dependent Reduction Potentials and Proton-Coupled Electron Transfer Mechanisms in Hydrogen-Producing Nickel Molecular Electrocatalysts. *Inorg. Chem.* **2013**, *52*, 3643−3652.
(133) Appel, A. M.; Pool, D. H.; O'Hagan, M.; Shaw, W. J.; Yang, J. Y.; Rakowski DuBois, M.; DuBois, D. L.; Bullock, R. M. [Ni(Pph2nbn2)-2(Ch3cn)]2+ as an Electrocatalyst for H2 Production: Dependence on Acid Strength and Isomer Distribution. *ACS Catal.* **2011**, *1*, 777−785.
(134) Hansen, H. A.; Rossmeisl, J.; Norskov, J. K. Surface Pourbaix Diagrams and Oxygen Reduction Activity of Pt, Ag and Ni(111) Surfaces Studied by Dft. *Phys. Chem. Chem. Phys.* **2008**, *10*, 3722−3730.
(135) Gossenberger, F.; Juarez, F.; Gross, A. Sulfate, Bisulfate, and Hydrogen Co-Adsorption on Pt(111) and Au(111) in an Electrochemical Environment. *Front. Chem.* **2020**, *8*, 634.
(136) Zeng, Z. H.; Chang, K. C.; Kubal, J.; Markovic, N. M.; Greeley, J. Stabilization of Ultrathin (Hydroxy) Oxide Films on Transition Metal Substrates for Electrochemical Energy Conversion. *Nature Energy* **2017**, *2*, 1−9.
(137) Groß, A. Grand-Canonical Approaches to Understand Structures and Processes at Electrochemical Interfaces from an Atomistic Perspective. *Curr. Opin Electrochem* **2021**, *27*, 100684.
(138) Kaduk, B.; Kowalczyk, T.; Van Voorhis, T. Constrained Density Functional Theory. *Chem. Rev.* **2012**, *112*, 321−370.
(139) Wu, Q.; Van Voorhis, T. Direct Optimization Method to Study Constrained Systems within Density-Functional Theory. *Phys. Rev. A* **2005**, *72*, 024502.
(140) Oberhofer, H.; Blumberger, J. Charge Constrained Density Functional Molecular Dynamics for Simulation of Condensed Phase Electron Transfer Reactions. *J. Chem. Phys.* **2009**, *131*, 064101.
(141) Blumberger, J.; Lamoureux, G. Reorganization Free Energies and Quantum Corrections for a Model Electron Self-Exchange Reaction: Comparison of Polarizable and Non-Polarizable Solvent Models. *Mol. Phys.* **2008**, *106*, 1597−1611.
(142) Mikkelsen, K. V.; Pedersen, S. U.; Lund, H.; Swanstrom, P. A New and Rigorous Method for Calculating Intramolecular Reorganization Energies for Electron-Transfer Reactions - Applied for Self-Exchange Reactions Involving Alkyl and Benzyl Radicals. *J. Phys. Chem.* **1991**, *95*, 8892−8899.
(143) Jakobsen, S.; Mikkelsen, K. V.; Pedersen, S. U. Calculations of Intramolecular Reorganization Energies for Electron-Transfer Reactions Involving Organic Systems. *J. Phys. Chem.* **1996**, *100*, 7411−7417.
(144) Iordanova, N.; Decornez, H.; Hammes-Schiffer, S. Theoretical Study of Electron, Proton, and Proton-Coupled Electron Transfer in Iron Bi-Imidazoline Complexes. *J. Am. Chem. Soc.* **2001**, *123*, 3723−3733.
(145) Hatcher, E.; Soudackov, A. V.; Hammes-Schiffer, S. Proton-Coupled Electron Transfer in Soybean Lipoxygenase. *J. Am. Chem. Soc.* **2004**, *126*, 5763−5775.
(146) Nelsen, S. F.; Blackstock, S. C.; Kim, Y. Estimation of Inner Shell Marcus Terms for Amino Nitrogen Compounds by Molecular Orbital Calculations. *J. Am. Chem. Soc.* **1987**, *109*, 677−682.
(147) Ghosh, S.; Horvath, S.; Soudackov, A. V.; Hammes-Schiffer, S. Electrochemical Solvent Reorganization Energies in the Framework of the Polarizable Continuum Model. *J. Chem. Theory Comput.* **2014**, *10*, 2091−2102.
(148) Auer, B.; Fernandez, L. E.; Hammes-Schiffer, S. Theoretical Analysis of Proton Relays in Electrochemical Proton-Coupled Electron Transfer. *J. Am. Chem. Soc.* **2011**, *133*, 8282−8292.
(149) Liu, Y. P.; Newton, M. D. Reorganization Energy for Electron-Transfer at Film-Modified Electrode Surfaces - a Dielectric Continuum Model. *J. Phys. Chem.* **1994**, *98*, 7162−7169.
(150) Bangle, R. E.; Schneider, J.; Piechota, E. J.; Troian-Gautier, L.; Meyer, G. J. Electron Transfer Reorganization Energies in the Electrode-Electrolyte Double Layer. *J. Am. Chem. Soc.* **2020**, *142*, 674−679.
(151) Ghosh, S.; Hammes-Schiffer, S. Calculation of Electrochemical Reorganization Energies for Redox Molecules at Self-Assembled Mono Layer Modified Electrodes. *J. Phys. Chem. Lett.* **2015**, *6*, 1−5.
(152) Ghosh, S.; Soudackov, A. V.; Hammes-Schiffer, S. Electrochemical Electron Transfer and Proton-Coupled Electron Transfer: Effects of Double Layer and Ionic Environment on Solvent Reorganization Energies. *J. Chem. Theory Comput.* **2016**, *12*, 2917−2925.
(153) Hartnig, C.; Koper, M. T. M. Molecular Dynamics Simulations of Solvent Reorganization in Electron-Transfer Reactions. *J. Chem. Phys.* **2001**, *115*, 8540−8546.
(154) Hartnig, C.; Koper, M. T. M. Molecular Dynamics Simulation of the First Electron Transfer Step in the Oxygen Reduction Reaction. *J. Electroanal. Chem.* **2002**, *532*, 165−170.
(155) Hartnig, C.; Koper, M. T. Solvent Reorganization in Electron and Ion Transfer Reactions near a Smooth Electrified Surface: A Molecular Dynamics Study. *J. Am. Chem. Soc.* **2003**, *125*, 9840−9845.
(156) Hartnig, C.; Vassilev, P.; Koper, M. T. M. Ab Initio and Classical Molecular Dynamics Studies of Electrode Reactions. *Electrochim. Acta* **2003**, *48*, 3751−3758.

https://doi.org/10.1021/acs.chemrev.1c00929
Chem. Rev. XXXX, XXX, XXX−XXX

(157) Hartnig, C.; Koper, M. T. M. Molecular Dynamics Simulation of Solvent Reorganization in Ion Transfer Reactions near a Smooth and Corrugated Surface. *J. Phys. Chem. B* **2004**, *108*, 3824−3827.
(158) Limaye, A. M.; Ding, W.; Willard, A. P. Understanding Attenuated Solvent Reorganization Energies near Electrode Interfaces. *J. Chem. Phys.* **2020**, *152*, 114706.
(159) Matyushov, D. V. Reorganization Energy of Electron Transfer in Polar Liquids. Dependence on Reactant Size, Temperature and Pressure. *Chem. Phys.* **1993**, *174*, 199−218.
(160) Vath, P.; Zimmt, M. B.; Matyushov, D. V.; Voth, G. A. A Failure of Continuum Theory: Temperature Dependence of the Solvent Reorganization Energy of Electron Transfer in Highly Polar Solvents. *J. Phys. Chem. B* **1999**, *103*, 9130−9140.
(161) Milischuk, A. A.; Matyushov, D. V.; Newton, M. D. Activation Entropy of Electron Transfer Reactions. *Chem. Phys.* **2006**, *324*, 172−194.
(162) Waskasi, M. M.; Newton, M. D.; Matyushov, D. V. Impact of Temperature and Non-Gaussian Statistics on Electron Transfer in Donor-Bridge-Acceptor Molecules. *J. Phys. Chem. B* **2017**, *121*, 2665−2676.
(163) Matyushov, D. V.; Newton, M. D. Thermodynamics of Reactions Affected by Medium Reorganization. *J. Phys. Chem. B* **2018**, *122*, 12302−12311.
(164) Jensen, F. *Introduction to Computational Chemistry*, 2nd ed.; Wiley, 2006.
(165) Jónsson, H.; Mills, G.; Jacobsen, K. W. In *Classical and Quantum Dynamics in Condensed Phase Simulations*; World Scientific, 1998; pp 385−404.
(166) Henkelman, G.; Uberuaga, B. P.; Jonsson, H. A Climbing Image Nudged Elastic Band Method for Finding Saddle Points and Minimum Energy Paths. *J. Chem. Phys.* **2000**, *113*, 9901−9904.
(167) Henkelman, G.; Jonsson, H. Improved Tangent Estimate in the Nudged Elastic Band Method for Finding Minimum Energy Paths and Saddle Points. *J. Chem. Phys.* **2000**, *113*, 9978−9985.
(168) Henkelman, G.; Jóhannesson, G.; Jónsson, H. In *Theoretical Methods in Condensed Phase Chemistry*; Schwartz, S. D., Ed.; Springer Netherlands: Dordrecht, 2002; pp 269−302.
(169) Goodrow, A.; Bell, A. T.; Head-Gordon, M. Are Spin-Forbidden Crossings a Bottleneck in Methanol Oxidation? *J. Phys. Chem. C* **2009**, *113*, 19361−19364.
(170) Cheng, L.; Ferguson, G. A.; Zygmunt, S. A.; Curtiss, L. A. Structure-Activity Relationships for Propane Oxidative Dehydrogenation by Anatase-Supported Vanadium Oxide Monomers and Dimers. *J. Catal.* **2013**, *302*, 31−36.
(171) Getsoian, A.; Shapovalov, V.; Bell, A. T. Dft Plus U Investigation of Propene Oxidation over Bismuth Molybdate: Active Sites, Reaction Intermediates, and the Role of Bismuth. *J. Phys. Chem. C* **2013**, *117*, 7123−7137.
(172) Chan, K.; Nørskov, J. K. Electrochemical Barriers Made Simple. *J. Phys. Chem. Lett.* **2015**, *6*, 2663−2668.
(173) Nie, X.; Esopi, M. R.; Janik, M. J.; Asthagiri, A. Selectivity of Co(2) Reduction on Copper Electrodes: The Role of the Kinetics of Elementary Steps. *Angew. Chem., Int. Ed. Engl.* **2013**, *52*, 2459−2462.
(174) Clayborne, A.; Chun, H. J.; Rankin, R. B.; Greeley, J. Elucidation of Pathways for No Electroreduction on Pt(111) from First Principles. *Angew. Chem., Int. Ed. Engl.* **2015**, *54*, 8255−8258.
(175) Chun, H. J.; Apaja, V.; Clayborne, A.; Honkala, K.; Greeley, J. Atomistic Insights into Nitrogen-Cycle Electrochemistry: A Combined Dft and Kinetic Monte Carlo Analysis of No Electrochemical Reduction on Pt(100). *ACS Catal.* **2017**, *7*, 3869−3882.
(176) Deshpande, S.; Greeley, J. First-Principles Analysis of Coverage, Ensemble, and Solvation Effects on Selectivity Trends in No Electroreduction on Pt3sn Alloys. *ACS Catal.* **2020**, *10*, 9320−9327.
(177) Nie, X. W.; Luo, W. J.; Janik, M. J.; Asthagiri, A. Reaction Mechanisms of Co2 Electrochemical Reduction on Cu(111) Determined with Density Functional Theory. *J. Catal.* **2014**, *312*, 108−122.
(178) Luo, W. J.; Nie, X. W.; Janik, M. J.; Asthagiri, A. Facet Dependence of Co2 Reduction Paths on Cu Electrodes. *ACS Catal.* **2016**, *6*, 219−229.
(179) Wang, S.; Petzold, V.; Tripkovic, V.; Kleis, J.; Howalt, J. G.; Skúlason, E.; Fernández, E. M.; Hvolbæk, B.; Jones, G.; Toftelund, A.; et al. Universal Transition State Scaling Relations for (De)-Hydrogenation over Transition Metals. *Phys. Chem. Chem. Phys.* **2011**, *13*, 20760−20765.
(180) Chan, K.; Nørskov, J. K. Potential Dependence of Electrochemical Barriers from Ab Initio Calculations. *J. Phys. Chem. Lett.* **2016**, *7*, 1686−1690.
(181) Skúlason, E.; Tripkovic, V.; Björketun, M. E.; Gudmundsdóttir, S.; Karlberg, G.; Rossmeisl, J.; Bligaard, T.; Jónsson, H.; Nørskov, J. K. Modeling the Electrochemical Hydrogen Oxidation and Evolution Reactions on the Basis of Density Functional Theory Calculations. *J. Phys. Chem. C* **2010**, *114*, 18182−18197.
(182) Akhade, S. A.; Bernstein, N. J.; Esopi, M. R.; Regula, M. J.; Janik, M. J. A Simple Method to Approximate Electrode Potential-Dependent Activation Energies Using Density Functional Theory. *Catal. Today* **2017**, *288*, 63−73.
(183) Akhade, S. A.; Nidzyn, R. M.; Rostamikia, G.; Janik, M. J. Using Bronsted-Evans-Polanyi Relations to Predict Electrode Potential-Dependent Activation Energies. *Catal. Today* **2018**, *312*, 82−91.
(184) Chun, H. J.; Zeng, Z. H.; Greeley, J. Direct Demonstration of Unified Bronsted-Evans-Polanyi Relationships for Proton-Coupled Electron Transfer Reactions on Transition Metal Surfaces. *J. Electrochem. Soc.* **2020**, *167*, 166516.
(185) Newton, M. D.; Sutin, N. Electron Transfer Reactions in Condensed Phases. *Annu. Rev. Phys. Chem.* **1984**, *35*, 437−480.
(186) Huang, Y.; Nielsen, R. J.; Goddard, W. A. Reaction Mechanism for the Hydrogen Evolution Reaction on the Basal Plane Sulfur Vacancy Site of Mos2 Using Grand Canonical Potential Kinetics. *J. Am. Chem. Soc.* **2018**, *140*, 16773−16782.
(187) Van den Bossche, M.; Skúlason, E.; Rose-Petruck, C.; Jónsson, H. Assessment of Constant-Potential Implicit Solvation Calculations of Electrochemical Energy Barriers for H2 Evolution on Pt. *J. Phys. Chem. C* **2019**, *123*, 4116−4124.
(188) Goodpaster, J. D.; Bell, A. T.; Head-Gordon, M. Identification of Possible Pathways for C−C Bond Formation During Electrochemical Reduction of Co2: New Theoretical Insights from an Improved Electrochemical Model. *J. Phys. Chem. Lett.* **2016**, *7*, 1471−1477.
(189) Singh, M. R.; Goodpaster, J. D.; Weber, A. Z.; Head-Gordon, M.; Bell, A. T. Mechanistic Insights into Electrochemical Reduction of Co2 over Ag Using Density Functional Theory and Transport Models. *Proc. National Acad. Sci.* **2017**, *114*, E8812−E8821.
(190) Schwarz, K. A.; Sundararaman, R.; Moffat, T. P.; Allison, T. C. Formic Acid Oxidation on Platinum: A Simple Mechanistic Study. *Phys. Chem. Chem. Phys.* **2015**, *17*, 20805−20813.
(191) Laio, A.; Parrinello, M. Escaping Free-Energy Minima. *Proc. National Acad. Sci.* **2002**, *99*, 12562−12566.
(192) Carter, E. A.; Ciccotti, G.; Hynes, J. T.; Kapral, R. Constrained Reaction Coordinate Dynamics for the Simulation of Rare Events. *Chem. Phys. Lett.* **1989**, *156*, 472−477.
(193) Sprik, M.; Ciccotti, G. Free Energy from Constrained Molecular Dynamics. *J. Chem. Phys.* **1998**, *109*, 7737−7744.
(194) Herron, J. A.; Morikawa, Y.; Mavrikakis, M. Ab Initio Molecular Dynamics of Solvation Effects on Reactivity at Electrified Interfaces. *Proc. National Acad. Sci.* **2016**, *113*, E4937−E4945.
(195) Cheng, T.; Xiao, H.; Goddard, W. A. Full Atomistic Reaction Mechanism with Kinetics for Co Reduction on Cu(100) from Ab Initio Molecular Dynamics Free-Energy Calculations at 298 K. *Proc. National Acad. Sci.* **2017**, *114*, 1795−1800.
(196) Goddard, W. A. New Quantum Mechanics Based Methods for Multiscale Simulations with Applications to Reaction Mechanisms for Electrocatalysis. *Top. Catal.* **2020**, *63*, 1658−1666.
(197) Cheng, T.; Xiao, H.; Goddard, W. A. Free-Energy Barriers and Reaction Mechanisms for the Electrochemical Reduction of Co on the

https://doi.org/10.1021/acs.chemrev.1c00929
Chem. Rev. XXXX, XXX, XXX−XXX

Cu(100) Surface, Including Multiple Layers of Explicit Solvent at Ph 0. *J. Phys. Chem. Lett.* **2015**, *6*, 4767−4773.
(198) Kronberg, R.; Laasonen, K. Reconciling the Experimental and Computational Hydrogen Evolution Activities of Pt(111) through Dft-Based Constrained Md Simulations. *ACS Catal.* **2021**, *11*, 8062−8078.
(199) Sugino, O.; Hamada, I.; Otani, M.; Morikawa, Y.; Ikeshoji, T.; Okamoto, Y. First-Principles Molecular Dynamics Simulation of Biased Electrode/Solution Interface. *Surf. Sci.* **2007**, *601*, 5237−5240.
(200) Otani, M.; Hamada, I.; Sugino, O.; Morikawa, Y.; Okamoto, Y.; Ikeshoji, T. Structure of the Water/Platinum Interface−a First Principles Simulation under Bias Potential. *Phys. Chem. Chem. Phys.* **2008**, *10*, 3609−3612.
(201) Bonnet, N.; Morishita, T.; Sugino, O.; Otani, M. First-Principles Molecular Dynamics at a Constant Electrode Potential. *Phys. Rev. Lett.* **2012**, *109*, 266101.
(202) Bouzid, A.; Pasquarello, A. Atomic-Scale Simulation of Electrochemical Processes at Electrode/Water Interfaces under Referenced Bias Potential. *J. Phys. Chem. Lett.* **2018**, *9*, 1880−1884.
(203) Bouzid, A.; Gono, P.; Pasquarello, A. Reaction Pathway of Oxygen Evolution on Pt(111) Revealed through Constant Fermi Level Molecular Dynamics. *J. Catal.* **2019**, *375*, 135−139.
(204) Islas-Vargas, C.; Guevara-García, A.; Galván, M. Electronic Structure Behavior of Pbo 2, Iro 2, and Sno 2 Metal Oxide Surfaces (110) with Dissociatively Adsorbed Water Molecules as a Function of the Chemical Potential. *J. Chem. Phys.* **2021**, *154*, 074704.
(205) Ikeshoji, T.; Otani, M. Toward Full Simulation of the Electrochemical Oxygen Reduction Reaction on Pt Using First-Principles and Kinetic Calculations. *Phys. Chem. Chem. Phys.* **2017**, *19*, 4447−4453.
(206) Ikeshoji, T.; Uchida, T.; Otani, M.; Osawa, M. First-Principles Molecular Dynamics Simulation for Electrochemical Hydrogen Production by 4,4′-Bipyridine Molecular Catalyst on Silver Electrode. *J. Electroanal. Chem.* **2017**, *800*, 13−18.
(207) Zhao, X.; Liu, Y. Origin of Selective Production of Hydrogen Peroxide by Electrochemical Oxygen Reduction. *J. Am. Chem. Soc.* **2021**, *143*, 9423−9428.
(208) Nattino, F.; Truscott, M.; Marzari, N.; Andreussi, O. Continuum Models of the Electrochemical Diffuse Layer in Electronic-Structure Calculations. *J. Chem. Phys.* **2019**, *150*, 041722.
(209) Gouy, G. Constitution of the Electric Charge at the Surface of an Electrolyte. *J. Phys. Theor. Appl.* **1910**, *9*, 457−468.
(210) Chapman, D. L. A Contribution to the Theory of Electrocapillarity. *Philosophical Mag, Ser. 6* **1913**, *25*, 475−481.
(211) Stern, O. The Theory of the Electrolytic Double-Layer. *Zeitschrift fuer Elektrochemie und Angewandte Physikalische Chemie* **1924**, *30*, 508−516.
(212) Bard, A. J. F., Larry, R. *Electrochemical Methods: Fundamentals and Applications*; John Wiley and Sons, 2000.
(213) Gongadze, E.; Van Rienen, U.; Iglič, A. Generalized Stern Models of the Electric Double Layer Considering the Spatial Variation of Permittivity and Finite Size of Ions in Saturation Regime. *Cellular & Molecular Biology Letters* **2011**, *16*, 576.
(214) Gongadze, E.; Iglič, A. Decrease of Permittivity of an Electrolyte Solution near a Charged Surface Due to Saturation and Excluded Volume Effects. *Bioelectrochemistry* **2012**, *87*, 199−203.
(215) Gongadze, E.; Iglic, A. Relative Permittivity in Stern and Diffuse Layers. *Acta Chim. Slov.* **2014**, *61*, 241−245.
(216) Goldsmith, Z. K.; Lam, Y. C.; Soudackov, A. V.; Hammes-Schiffer, S. Proton Discharge on a Gold Electrode from Triethylammonium in Acetonitrile: Theoretical Modeling of Potential-Dependent Kinetic Isotope Effects. *J. Am. Chem. Soc.* **2019**, *141*, 1084−1090.
(217) Borukhov, I.; Andelman, D.; Orland, H. Steric Effects in Electrolytes: A Modified Poisson-Boltzmann Equation. *Arxiv* **1997**, *79*, 435−438.
(218) Borukhov, I.; Andelman, D.; Orland, H. Adsorption of Large Ions from an Electrolyte Solution: A Modified Poisson−Boltzmann Equation. *Electrochim. Acta* **2000**, *46*, 221−229.
(219) Jinnouchi, R.; Anderson, A. B. Electronic Structure Calculations of Liquid-Solid Interfaces: Combination of Density Functional Theory and Modified Poisson-Boltzmann Theory. *Phys. Rev. B* **2008**, *77*, 245417.
(220) Fattebert, J. L.; Gygi, F. Density Functional Theory for Efficient Ab Initio Molecular Dynamics Simulations in Solution. *J. Comput. Chem.* **2002**, *23*, 662−666.
(221) Fattebert, J. L.; Gygi, F. First-Principles Molecular Dynamics Simulations in a Continuum Solvent. *Int. J. Quantum Chem.* **2003**, *93*, 139−147.
(222) Andreussi, O.; Dabo, I.; Marzari, N. Revised Self-Consistent Continuum Solvation in Electronic-Structure Calculations. *J. Chem. Phys.* **2012**, *136*, 064102.
(223) Andreussi, O.; Hörmann, N. G.; Nattino, F.; Fisicaro, G.; Goedecker, S.; Marzari, N. Solvent-Aware Interfaces in Continuum Solvation. *J. Chem. Theory Comput.h* **2019**, *15*, 1996−2009.
(224) Wu, J.; Jiang, T.; Jiang, D.-e.; Jin, Z.; Henderson, D. A Classical Density Functional Theory for Interfacial Layering of Ionic Liquids. *Soft Matter* **2011**, *7*, 11222.
(225) Sundararaman, R.; Arias, T. A. Efficient Classical Density-Functional Theories of Rigid-Molecular Fluids and a Simplified Free Energy Functional for Liquid Water. *Comput. Phys. Commun.* **2014**, *185*, 818−825.
(226) Sundararaman, R.; Letchworth-Weaver, K.; Arias, T. A. A Recipe for Free-Energy Functionals of Polarizable Molecular Fluids. *J. Chem. Phys.* **2014**, *140*, 144504.
(227) Petrosyan, S. A.; Briere, J.-F.; Roundy, D.; Arias, T. A. Joint Density-Functional Theory for Electronic Structure of Solvated Systems. *Phys. Rev. B* **2007**, *75*, 205105.
(228) Mathew, K.; Sundararaman, R.; Letchworth-Weaver, K.; Arias, T. A.; Hennig, R. G. Implicit Solvation Model for Density-Functional Study of Nanocrystal Surfaces and Reaction Pathways. *J. Chem. Phys.* **2014**, *140*, 084106.
(229) Schnur, S.; Groß, A. Challenges in the First-Principles Description of Reactions in Electrocatalysis. *Catal. Today* **2011**, *165*, 129−137.
(230) Hansen, M. H.; Rossmeisl, J. Ph in Grand Canonical Statistics of an Electrochemical Interface. *J. Phys. Chem. C* **2016**, *120*, 29135−29143.
(231) Le, J.; Iannuzzi, M.; Cuesta, A.; Cheng, J. Determining Potentials of Zero Charge of Metal Electrodes Versus the Standard Hydrogen Electrode from Density-Functional-Theory-Based Molecular Dynamics. *Phys. Rev. Lett.* **2017**, *119*, 016801.
(232) Le, J.-B.; Cheng, J. Modeling Electrochemical Interfaces from Ab Initio Molecular Dynamics: Water Adsorption on Metal Surfaces at Potential of Zero Charge. *Curr. Opin Electrochem* **2020**, *19*, 129−136.
(233) Guo, Z.; Ambrosio, F.; Chen, W.; Gono, P.; Pasquarello, A. Alignment of Redox Levels at Semiconductor−Water Interfaces. *Chem. Mater.* **2018**, *30*, 94−111.
(234) Cheng, J.; Sprik, M. Alignment of Electronic Energy Levels at Electrochemical Interfaces. *Phys. Chem. Chem. Phys.* **2012**, *14*, 11245−11267.
(235) Cheng, J.; Sprik, M. Aligning Electronic Energy Levels at the Tio2/H2o Interface. *Phys. Rev. B* **2010**, *82*, 081406.
(236) Groß, A.; Gossenberger, F.; Lin, X.; Naderian, M.; Sakong, S.; Roman, T. Water Structures at Metal Electrodes Studied by Ab Initio Molecular Dynamics Simulations. *J. Electrochem. Soc.* **2014**, *161*, E3015.
(237) Sakong, S.; Forster-Tonigold, K.; Groß, A. The Structure of Water at a Pt(111) Electrode and the Potential of Zero Charge Studied from First Principles. *J. Chem. Phys.* **2016**, *144*, 194701.
(238) Sakong, S.; Groß, A. The Electric Double Layer at Metal-Water Interfaces Revisited Based on a Charge Polarization Scheme. *J. Chem. Phys.* **2018**, *149*, 084705.
(239) Sakong, S.; Groß, A. Water Structures on a Pt(111) Electrode from Ab Initio Molecular Dynamic Simulations for a Variety of Electrochemical Conditions. *Phys. Chem. Chem. Phys.* **2020**, *22*, 10431−10437.
(240) Calegari Andrade, M. F.; Ko, H.-Y.; Car, R.; Selloni, A. Structure, Polarization, and Sum Frequency Generation Spectrum of Interfacial Water on Anatase Tio2. *J. Phys. Chem. Lett.* **2018**, *9*, 6716−6721.

https://doi.org/10.1021/acs.chemrev.1c00929
Chem. Rev. XXXX, XXX, XXX−XXX

(241) Le, J.-B.; Fan, Q.-Y.; Li, J.-Q.; Cheng, J. Molecular Origin of Negative Component of Helmholtz Capacitance at Electrified Pt(111)/Water Interface. *Science Advances* **2020**, *6*, No. eabb1219.
(242) Natarajan, S. K.; Behler, J. Neural Network Molecular Dynamics Simulations of Solid−Liquid Interfaces: Water at Low-Index Copper Surfaces. *Phys. Chem. Chem. Phys.* **2016**, *18*, 28704−28725.
(243) Perram, J. W.; Ratner, M. A. Simulations at Conducting Interfaces: Boundary Conditions for Electrodes and Electrolytes. *J. Chem. Phys.* **1996**, *104*, 5174−5180.
(244) Pounds, M.; Tazi, S.; Salanne, M.; Madden, P. A. Ion Adsorption at a Metallic Electrode: An Ab Initio Based Simulation Study. *J. Phys. (Paris)* **2009**, *21*, 424109.
(245) Willard, A. P.; Reed, S. K.; Madden, P. A.; Chandler, D. Water at an Electrochemical Interface—a Simulation Study. *Faraday Discuss.* **2009**, *141*, 423−441.
(246) Petersen, M. K.; Kumar, R.; White, H. S.; Voth, G. A. A Computationally Efficient Treatment of Polarizable Electrochemical Cells Held at a Constant Potential. *J. Phys. Chem. C* **2012**, *116*, 4903−4912.
(247) Dwelle, K. A.; Willard, A. P. Constant Potential, Electrochemically Active Boundary Conditions for Electrochemical Simulation. *J. Phys. Chem. C* **2019**, *123*, 24095−24103.
(248) Shin, S.; Willard, A. P. Water's Interfacial Hydrogen Bonding Structure Reveals the Effective Strength of Surface−Water Interactions. *J. Phys. Chem. B* **2018**, *122*, 6781−6789.
(249) Huang, B.; Myint, K. H.; Wang, Y.; Zhang, Y.; Rao, R. R.; Sun, J.; Muy, S.; Katayama, Y.; Garcia, J. C.; Fraggedakis, D.; et al. Cation-Dependent Interfacial Structures and Kinetics for Outer-Sphere Electron-Transfer Reactions. *J. Phys. Chem. C* **2021**, *125*, 4397−4411.
(250) van Duin, A. C. T.; Dasgupta, S.; Lorant, F.; Goddard, W. A. Reaxff: A Reactive Force Field for Hydrocarbons. *J. Phys. Chem. A* **2001**, *105*, 9396−9409.
(251) Senftle, T. P.; Hong, S.; Islam, M. M.; Kylasa, S. B.; Zheng, Y.; Shin, Y. K.; Junkermeier, C.; Engel-Herbert, R.; Janik, M. J.; Aktulga, H. M.; et al. The Reaxff Reactive Force-Field: Development, Applications and Future Directions. *npj Computational Materials* **2016**, *2*, 1−14.
(252) Naserifar, S.; Chen, Y.; Kwon, S.; Xiao, H.; Goddard, W. A. Artificial Intelligence and Qm/Mm with a Polarizable Reactive Force Field for Next-Generation Electrocatalysts. *Matter* **2021**, *4*, 195−216.
(253) Harmon, K. J.; Letchworth-Weaver, K.; Gaiduk, A. P.; Giberti, F.; Gygi, F.; Chan, M. K. Y.; Fenter, P.; Galli, G. Validating First-Principles Molecular Dynamics Calculations of Oxide/Water Interfaces with X-Ray Reflectivity Data. *Phys. Rev. Mater.* **2020**, *4*, 113805.
(254) Zeng, Z. H.; Greeley, J. Characterization of Oxygenated Species at Water/Pt(111) Interfaces from Dft Energetics and Xps Simulations. *Nano Energy* **2016**, *29*, 369−377.
(255) Fried, S. D.; Bagchi, S.; Boxer, S. G. Extreme Electric Fields Power Catalysis in the Active Site of Ketosteroid Isomerase. *Science* **2014**, *346*, 1510−1514.
(256) Fried, S. D.; Boxer, S. G. Electric Fields and Enzyme Catalysis. *Annu. Rev. Biochem.* **2017**, *86*, 387−415.
(257) Patrow, J. G.; Sorenson, S. A.; Dawlaty, J. M. Direct Spectroscopic Measurement of Interfacial Electric Fields near an Electrode under Polarizing or Current-Carrying Conditions. *J. Phys. Chem. C* **2017**, *121*, 11585−11592.
(258) Sorenson, S. A.; Patrow, J. G.; Dawlaty, J. M. Solvation Reaction Field at the Interface Measured by Vibrational Sum Frequency Generation Spectroscopy. *J. Am. Chem. Soc.* **2017**, *139*, 2369−2378.
(259) Clark, M. L.; Ge, A.; Videla, P. E.; Rudshteyn, B.; Miller, C. J.; Song, J.; Batista, V. S.; Lian, T.; Kubiak, C. P. Co2 Reduction Catalysts on Gold Electrode Surfaces Influenced by Large Electric Fields. *J. Am. Chem. Soc.* **2018**, *140*, 17643−17655.
(260) Ge, A.; Videla, P. E.; Lee, G. L.; Rudshteyn, B.; Song, J.; Kubiak, C. P.; Batista, V. S.; Lian, T. Interfacial Structure and Electric Field Probed by in Situ Electrochemical Vibrational Stark Effect Spectroscopy and Computational Modeling. *J. Phys. Chem. C* **2017**, *121*, 18674−18682.
(261) Wesley, T. S.; Román-Leshkov, Y.; Surendranath, Y. Spontaneous Electric Fields Play a Key Role in Thermochemical Catalysis at Metal-Liquid Interfaces. *ACS Cent. Sci.* **2021**, *7*, 1045−1055.
(262) Goldsmith, Z. K.; Secor, M.; Hammes-Schiffer, S. Inhomogeneity of Interfacial Electric Fields at Vibrational Probes on Electrode Surfaces. *ACS Cent. Sci.* **2020**, *6*, 304−311.
(263) Marston, C. C.; Balint-Kurti, G. G. The Fourier Grid Hamiltonian Method for Bound State Eigenvalues and Eigenfunctions. *J. Chem. Phys.* **1989**, *91*, 3571−3576.
(264) Webb, S. P.; Hammes-Schiffer, S. Fourier Grid Hamiltonian Multiconfigurational Self-Consistent-Field: A Method to Calculate Multidimensional Hydrogen Vibrational Wavefunctions. *J. Chem. Phys.* **2000**, *113*, 5214−5227.
(265) Sarkar, S.; Maitra, A.; Lake, W. R.; Warburton, R. E.; Hammes-Schiffer, S.; Dawlaty, J. M. Mechanistic Insights About Electrochemical Proton-Coupled Electron Transfer Derived from a Vibrational Probe. *J. Am. Chem. Soc.* **2021**, *143*, 8381−8390.
(266) Borgis, D. C.; Lee, S.; Hynes, J. T. A Dynamical Theory of Nonadiabatic Proton and Hydrogen Atom Transfer Reaction Rates in Solution. *Chem. Phys. Lett.* **1989**, *162*, 19−26.
(267) Borgis, D.; Hynes, J. T. Dynamical Theory of Proton Tunneling Transfer Rates in Solution: General Formulation. *Chem. Phys.* **1993**, *170*, 315−346.
(268) Staib, A.; Borgis, D.; Hynes, J. T. Proton Transfer in Hydrogen-Bonded Acid-Base Complexes in Polar Solvents. *J. Chem. Phys.* **1995**, *102*, 2487.
(269) Borgis, D.; Hynes, J. T. Curve Crossing Formulation for Proton Transfer Reactions in Solution. *J. Phys. Chem.* **1996**, *100*, 1118−1128.
(270) Kiefer, P. M.; Hynes, J. T. Kinetic Isotope Effects for Adiabatic Proton Transfer Reactions in a Polar Environment. *J. Phys. Chem. A* **2003**, *107*, 9022−9039.
(271) Kiefer, P. M.; Hynes, J. T. Kinetic Isotope Effects for Nonadiabatic Proton Transfer Reactions in a Polar Environment. 1. Interpretation of Tunneling Kinetic Isotopic Effects. *J. Phys. Chem. A* **2004**, *108*, 11793−11808.
(272) Cukier, R. Mechanism for Proton-Coupled Electron-Transfer Reactions. *J. Phys. Chem.* **1994**, *98*, 2377−2381.
(273) Cukier, R.; Zhao, X. G. Molecular Dynamics and Quantum Chemistry Study of a Proton-Coupled Electron Transfer Reaction. *J. Phys. Chem.* **1995**, *99*, 945−954.
(274) Cukier, R. Proton-Coupled Electron Transfer Reactions: Evaluation of Rate Constants. *J. Phys. Chem.* **1996**, *100*, 15428−15443.
(275) Cukier, R. I.; Nocera, D. G. Proton-Coupled Electron Transfer. *Annu. Rev. Phys. Chem.* **1998**, *49*, 337−369.
(276) Basilevsky, M. V.; Chudinov, G. E.; Newton, M. D. The Multi-Configurational Adiabatic Electron Transfer Theory and Its Invariance under Transformations of Charge Density Basis Functions. *Chem. Phys.* **1994**, *179*, 263−278.
(277) Marcus, R. A. Electrostatic Free Energy and Other Properties of States Having Nonequilibrium Polarization. 1. *J. Chem. Phys.* **1956**, *24*, 979−989.
(278) Warshel, A. Dynamics of Reactions in Polar Solvents. Semiclassical Trajectory Studies of Electron-Transfer and Proton-Transfer Reactions. *J. Phys. Chem.* **1982**, *86*, 2218−2224.
(279) Basilevsky, M. V.; Soudackov, A. V.; Vener, M. V. Electron-Proton Free-Energy Surfaces for Proton Transfer Reaction in Polar Solvents: Test Calculations for Carbon-Carbon Reaction Centres. *Chem. Phys.* **1995**, *200*, 87−106.
(280) Basilevsky, M. V.; Vener, M. V.; Davidovich, G. V.; Soudackov, A. V. Dynamics of Proton Transfer Reactions in Polar Solvent in the Non-Adiabatic Two-State Approximation: Test Calculations for Carbon-Carbon Reaction Centre. *Chem. Phys.* **1996**, *208*, 267−282.
(281) Basilevsky, M. V.; Vener, M. V. Collective Medium Coordinates and Their Application in the Theory of Chemical Reactions. *J. Mol. Struct.* **1997**, *398*, 81−92.
(282) Kestner, N. R.; Logan, J.; Jortner, J. Thermal Electron Transfer Reactions in Polar Solvents. *J. Phys. Chem.* **1974**, *78*, 2148−2166.

https://doi.org/10.1021/acs.chemrev.1c00929
Chem. Rev. XXXX, XXX, XXX−XXX

(283) Sirjoosingh, A.; Hammes-Schiffer, S. Proton-Coupled Electron Transfer Versus Hydrogen Atom Transfer: Generation of Charge-Localized Diabatic States. *J. Phys. Chem. A* **2011**, *115*, 2367−2377.
(284) Sirjoosingh, A.; Hammes-Schiffer, S. Diabatization Schemes for Generating Charge-Localized Electron−Proton Vibronic States in Proton-Coupled Electron Transfer Systems. *J. Chem. Theory Comput.h* **2011**, *7*, 2831−2841.
(285) Soudackov, A. V.; Hammes-Schiffer, S. Probing Non-adiabaticity in the Proton-Coupled Electron Transfer Reaction Catalyzed by Soybean Lipoxygenase. *J. Phys. Chem. Lett.* **2014**, *5*, 3274−3278.
(286) Harshan, A. K.; Yu, T.; Soudackov, A. V.; Hammes-Schiffer, S. Dependence of Vibronic Coupling on Molecular Geometry and Environment: Bridging Hydrogen Atom Transfer and Electron−Proton Transfer. *J. Am. Chem. Soc.* **2015**, *137*, 13545−13555.
(287) Klein, J. E. M. N.; Knizia, G. Cpcet Versus Hat: A Direct Theoretical Method for Distinguishing X-H Bond-Activation Mechanisms. *Angew. Chem.* **2018**, *57*, 11913−11917.
(288) Hammes-Schiffer, S.; Hatcher, E.; Ishikita, H.; Skone, J. H.; Soudackov, A. V. Theoretical Studies of Proton-Coupled Electron Transfer: Models and Concepts Relevant to Bioenergetics. *Coord. Chem. Rev.* **2008**, *252*, 384−394.
(289) Navrotskaya, I.; Soudackov, A. V.; Hammes-Schiffer, S. Model System-Bath Hamiltonian and Nonadiabatic Rate Constants for Proton-Coupled Electron Transfer at Electrode-Solution Interfaces. *J. Chem. Phys.* **2008**, *128*, 244712.
(290) Navrotskaya, I.; Hammes-Schiffer, S. Electrochemical Proton-Coupled Electron Transfer: Beyond the Golden Rule. *J. Chem. Phys.* **2009**, *131*, 024112.
(291) Ludlow, M. K.; Soudackov, A. V.; Hammes-Schiffer, S. Electrochemical Proton-Coupled Electron Transfer of an Osmium Aquo Complex: Theoretical Analysis of Asymmetric Tafel Plots and Transfer Coefficients. *J. Am. Chem. Soc.* **2010**, *132*, 1234−1235.
(292) Levich, V. G. In *Physical Chemistry: An Advanced Treatise*; Eyring, H., Henderson, H., Jost, W., Eds.; Academic Press: London, 1970; Vol. *IXB*, pp 985−1074.
(293) Costentin, C.; Evans, D. H.; Robert, M.; Savéant, J.-M.; Singh, P. S. Electrochemical Approach to Concerted Proton and Electron Transfers. Reduction of the Water-Superoxide Ion Complex. *J. Am. Chem. Soc.* **2005**, *127*, 12490−12491.
(294) Costentin, C.; Robert, M.; Savéant, J.-M. Electrochemical Concerted Proton and Electron Transfers. Potential-Dependent Rate Constant, ... *J. Electroanal. Chem.* **2006**, *588*, 197−206.
(295) Costentin, C.; Robert, M.; Savéant, J.-M. Electrochemical and Homogeneous Proton-Coupled Electron Transfers: Concerted Pathways in the One-Electron Oxidation of a Phenol Coupled with an Intramolecular Amine-Driven Proton Transfer. *J. Am. Chem. Soc.* **2006**, *128*, 4552−4553.
(296) Costentin, C.; Robert, M.; Savéant, J.-M. Adiabatic and Non-Adiabatic Concerted Proton-Electron Transfers. Temperature Effects in the Oxidation of Intramolecularly Hydrogen-Bonded Phenols. *J. Am. Chem. Soc.* **2007**, *129*, 9953−9963.
(297) Brako, R.; Newns, D. M. Charge Exchange in Atom-Surface Scattering: Thermal Versus Quantum Mechanical Non-Adiabaticity. *Surf. Sci.* **1981**, *108*, 253−270.
(298) Wu, Q.; Van Voorhis, T. Direct Calculation of Electron Transfer Parameters through Constrained Density Functional Theory. *J. Phys. Chem. A* **2006**, *110*, 9212−9218.
(299) Wu, Q.; Cheng, C.-L.; Van Voorhis, T. Configuration Interaction Based on Constrained Density Functional Theory: A Multireference Method. *J. Chem. Phys.* **2007**, *127*, 164119.
(300) Kubas, A.; Hoffmann, F.; Heck, A.; Oberhofer, H.; Elstner, M.; Blumberger, J. Electronic Couplings for Molecular Charge Transfer: Benchmarking Cdft, Fodft, and Fodftb against High-Level Ab Initio Calculations. *J. Chem. Phys.* **2014**, *140*, 104105.
(301) Melander, M.; Jonsson, E. O.; Mortensen, J. J.; Vegge, T.; Garcia Lastra, J. M. Implementation of Constrained Dft for Computing Charge Transfer Rates within the Projector Augmented Wave Method. *J. Chem. Theory Comput.* **2016**, *12*, 5367−5378.
(302) Nordlander, P.; Tully, J. C. Energy Shifts and Broadening of Atomic Levels near Metal Surfaces. *Phys. Rev. B* **1990**, *42*, 5564−5578.
(303) Gosavi, S.; Marcus, R. A. Nonadiabatic Electron-Transfer at Metal Surfaces. *J. Phys. Chem. B* **2000**, *104*, 2067−2072.
(304) Gosavi, S.; Gao, Y. Q.; Marcus, R. A. Temperature Dependence of the Electronic Factor in the Nonadiabatic Electron Transfer at Metal and Semiconductor Electrodes. *J. Electroanal. Chem.* **2001**, *500*, 71−77.
(305) Maggio, E.; Martsinovich, N.; Troisi, A. Evaluating Charge Recombination Rate in Dye-Sensitized Solar Cells from Electronic Structure Calculations. *J. Phys. Chem. C* **2012**, *116*, 7638−7649.
(306) Kondov, I.; Thoss, M.; Wang, H. Theoretical Study of Ultrafast Heterogeneous Electron Transfer Reactions at Dye-Semiconductor Interfaces: Coumarin 343 at Titanium Oxide †. *J. Phys. Chem. A* **2006**, *110*, 1364−1374.
(307) Kondov, I.; Čížek, M.; Benesch, C.; Wang, H.; Thoss, M. Quantum Dynamics of Photoinduced Electron-Transfer Reactions in Dye-Semiconductor Systems: First-Principles Description and Application to Coumarin 343-Tio 2. *J. Phys. Chem. C* **2007**, *111*, 11970−11981.
(308) Li, J.; Kondov, I.; Wang, H.; Thoss, M. Theoretical Study of Photoinduced Electron-Transfer Processes in the Dye-Semiconductor System Alizarin-Tio2. *J. Phys. Chem. B* **2010**, *114*, 18481−18493.
(309) Prucker, V.; Rubio-Pons, O.; Bockstedte, M.; Wang, H.; Coto, P. B.; Thoss, M. Dynamical Simulation of Electron Transfer Processes in Alkanethiolate Self-Assembled Monolayers at the Au(111) Surface. *J. Phys. Chem. C* **2013**, *117*, 25334−25342.
(310) Li, J.; Kondov, I.; Wang, H.; Thoss, M. Quantum Dynamical Simulation of Photoinduced Electron Transfer Processes in Dye-Semiconductor Systems: Theory and Application to Coumarin 343 at Tio□. *J. Phys. (Paris)* **2015**, *27*, 134202.
(311) Ghosh, S.; Castillo-Lora, J.; Soudackov, A. V.; Mayer, J. M.; Hammes-Schiffer, S. Theoretical Insights into Proton-Coupled Electron Transfer from a Photoreduced Zno Nanocrystal to an Organic Radical. *Nano Lett.* **2017**, *17*, 5762−5767.
(312) Ghan, S.; Kunkel, C.; Reuter, K.; Oberhofer, H. Improved Projection-Operator Diabatization Schemes for the Calculation of Electronic Coupling Values. *J. Chem. Theory Comput.h* **2020**, *16*, 7431−7443.
(313) Odella, E.; Wadsworth, B. L.; Mora, S. J.; Goings, J. J.; Huynh, M. T.; Gust, D.; Moore, T. A.; Moore, G. F.; Hammes-Schiffer, S.; Moore, A. L. Proton-Coupled Electron Transfer Drives Long-Range Proton Translocation in Bioinspired Systems. *J. Am. Chem. Soc.* **2019**, *141*, 14057−14061.
(314) Edwards, S. J.; Soudackov, A. V.; Hammes-Schiffer, S. Analysis of Kinetic Isotope Effects for Proton-Coupled Electron Transfer Reactions. *J. Phys. Chem. A* **2009**, *113*, 2117−2126.
(315) Gray, H. B. Powering the Planet with Solar Fuel. *Nat. Chem.* **2009**, *1*, 7−7.
(316) Conway, B. E.; Tilak, B. V. Interfacial Processes Involving Electrocatalytic Evolution and Oxidation of H2, and the Role of Chemisorbed H. *Electrochim. Acta* **2002**, *47*, 3571−3594.
(317) Christov, S. G. Zur Temperaturabhängigkeit Der Geschwindigkeit Der Vorgänge Vom Standpunkt Der Quantenmechanik. *Z. Phys. Chem.* **1960**, *214O*, 40−62.
(318) Bockris, J. O. M.; Srinivasan, S.; Matthews, D. B. Proton Transfer across Double Layers. Mechanism Evaluation from Isotopic Effects. *Discuss. Faraday Soc.* **1965**, *39*, 239−252.
(319) Bockris, J. O. M.; Matthews, D. B. The Mechanism of Charge Transfer at Electrodes. *Proc. R. Soc. London, Ser. A* **1966**, *292*, 479−488.
(320) Horiuti, J.; Polanyi, M. Outlines of a Theory of Proton Transfer. *J. Mol. Catal. A: Chem.* **2003**, *199*, 185−197.
(321) Dogonadze, R. R.; Kuznetsov, A. M.; Levich, V. G. Quantum Theory of the Hydrogen Overvoltage. *Russ. J. Electrochem.* **1967**, *3*, 648−650.
(322) Kuznetsov, A. M. *Charge Transfer in Physics, Chemistry and Biology: Physical Mechanisms of Elementary Processes and an Introduction to the Theory*, 1st ed.; CRC Press, 1995.

https://doi.org/10.1021/acs.chemrev.1c00929
Chem. Rev. XXXX, XXX, XXX−XXX

(323) Dogonadze, R. R.; Kuznetsov, A. M.; Chernenko, A. A. Theory of Homogeneous and Heterogeneous Electronic Processes in Liquids. *Russ. Chem. Rev.* **1965**, *34*, 759−775.
(324) Dogonadze, R. R.; Kuznetsov, A. M.; Vorotyntsev, M. A. On the Theory of Adiabatic and Non-Adiabatic Electrochemical Reactions. *J. Electroanal. Chem. Interfacial Electrochem.* **1970**, *25*, A17−A19.
(325) Benderskii, V. A.; Dakhnovskii, Y. I.; Ovchinnikov, A. A. Theory of Electrochemical Hydrogen Evolution Reactions. Part Ii. Model of Harmonic Proton Terms of Different Frequencies. *J. Electroanal. Chem.* **1983**, *148*, 161−181.
(326) Kuznetsov, A. M. Variation of the Charge of the Adsorbed Hydrogen Atom in the Process of the Activation in the Elementary Act of Hydrogen Ion Discharge. *J. Electroanal. Chem. Interfacial Electrochem.* **1983**, *159*, 241−255.
(327) Kuznetsov, A. M. A Theory of Chemical and Electrochemical Reactions at Weak Coupling with the Medium. *J. Electroanal. Chem. Interfacial Electrochem.* **1983**, *151*, 227−249.
(328) Sebastian, K. L. Electronic Friction in Proton Tunneling at the Electrochemical Interface. *J. Chem. Phys.* **1998**, *109*, 1111−1119.
(329) Benderskii, V. A.; Grebenshchikov, S. Y. Reorganization of the Medium and Local Vibrations in Electrode Reactions of Electron-Proton Transfer. *J. Electroanal. Chem.* **1994**, *375*, 29−44.
(330) Krishtalik, L. I. Proton Transfer in Electrode Reactions. Experimental Test of Two Theoretical Models. *Faraday Discuss. Chem. Soc.* **1982**, *74*, 205−213.
(331) Conway, B. E.; Tessier, D. F.; Wilkinson, D. P. Kinetic Behaviour of Electrochemical Proton Discharge in Relation to the Proton Source and Its Environment. *J. Electroanal. Chem. Interfacial Electrochem.* **1986**, *204*, 111−130.
(332) Haghighat, S.; Dawlaty, J. M. Ph Dependence of the Electron-Transfer Coefficient: Comparing a Model to Experiment for Hydrogen Evolution Reaction. *J. Phys. Chem. C* **2016**, *120*, 28489−28496.
(333) Kahyarian, A.; Brown, B.; Nesic, S. Mechanism of the Hydrogen Evolution Reaction in Mildly Acidic Environments on Gold. *J. Electrochem. Soc.* **2017**, *164*, H365−H374.
(334) Jackson, M. N.; Surendranath, Y. Donor-Dependent Kinetics of Interfacial Proton-Coupled Electron Transfer. *J. Am. Chem. Soc.* **2016**, *138*, 3228−3234.
(335) Jackson, M. N.; Jung, O.; Lamotte, H. C.; Surendranath, Y. Donor-Dependent Promotion of Interfacial Proton-Coupled Electron Transfer in Aqueous Electrocatalysis. *ACS Catal.* **2019**, *9*, 3737−3743.
(336) Velikonja, A.; Gongadze, E.; Kralj-Iglic, V.; Iglic, A., Charge Dependent Capacitance of Stern Layer and Capacitance of Electrode/Electrolyte Interface. *Int. J. Electrochem. Sci.* **2014**, *9*, 10.
(337) Limaye, A. M.; Willard, A. P. Modeling Interfacial Electron Transfer in the Double Layer: The Interplay between Electrode Coupling and Electrostatic Driving. *J. Phys. Chem. C* **2020**, *124*, 1352−1361.
(338) Koper, M. T. M. Volcano Activity Relationships for Proton-Coupled Electron Transfer Reactions in Electrocatalysis. *Top. Catal.* **2015**, *58*, 1153−1158.
(339) Grimley, T. B.; Pisani, C. Chemisorption Theory in the Hartree-Fock Approximation. *J. Phys. C* **1974**, *7*, 2831−2848.
(340) Grimley, T. B. Chemisorption Theory. *Crit. Rev. Solid State Mater. Sci.* **1976**, *6*, 239−252.
(341) Muscat, J. P.; Newns, D. M. Chemisorption on Metals. *Prog. Surf. Sci.* **1978**, *9*, 1−43.
(342) Muscat, J. P.; Newns, D. M. Theoretical Model of Chemisorption on Metals. *Surf. Sci.* **1979**, *87*, 643−655.
(343) Schmickler, W. A Theory of Adiabatic Electron-Transfer Reactions. *J. Electroanal. Chem.* **1986**, *204*, 31−43.
(344) Koper, M. T. M.; Schmickler, W. A Kramers Reaction Rate Theory for Electrochemical Ion Transfer Reactions. *Chem. Phys.* **1996**, *211*, 123−133.
(345) Koper, M. T. M.; Mohr, J.; Schmickler, W. Quantum Effects in Adiabatic Electrochemical Electron-Transfer Reactions. *Chem. Phys.* **1997**, *220*, 95−114.
(346) Boroda, Y. G.; Voth, G. A. A Theory for Adiabatic Electron Transfer Processes across the Semiconductor/Electrolyte Interface. *J. Chem. Phys.* **1996**, *104*, 6168−6183.
(347) Boroda, Y. G. Further Developments on the Theory of Electron Transfer Across the Electrode/Electrolyte Interface. PhD Thesis, University of Pennsylvania, Philadelphia, 1997.
(348) Boroda, Y. G.; Calhoun, A.; Voth, G. A. A Theory for Electron Transfer across the Electrode/Electrolyte Interface Involving More Than One Redox Ion. *J. Chem. Phys.* **1997**, *107*, 8940−8954.
(349) Boroda, Y. G.; Voth, G. A. A Theory for Electron Transfer between an Electrode and a Multilevel Acceptor/Donor Species in an···. *J. Electroanal. Chem.* **1998**, *450*, 95−107.
(350) Schmickler, W.; Mohr, J. The Rate of Electrochemical Electron-Transfer Reactions. *J. Chem. Phys.* **2002**, *117*, 2867−2872.
(351) Schmickler, W. A Theory for Nonadiabatic Electrochemical Electron-Transfer Reactions Involving the Breaking of a Bond. *Chem. Phys. Lett.* **2000**, *317*, 458−463.
(352) Santos, E.; Koper, M. T. M.; Schmickler, W. A Model for Bond-Breaking Electron Transfer at Metal Electrodes. *Chem. Phys. Lett.* **2006**, *419*, 421−425.
(353) Santos, E.; Koper, M. T. M.; Schmickler, W. Bond-Breaking Electron Transfer of Diatomic Reactants at Metal Electrodes. *Chem. Phys.* **2008**, *344*, 195−201.
(354) Santos, E.; Schmickler, W. D-Band Catalysis in Electrochemistry. *ChemPhysChem* **2006**, *7*, 2282−2285.
(355) Santos, E.; Schmickler, W. Fundamental Aspects of Electrocatalysis. *Chem. Phys.* **2007**, *332*, 39−47.
(356) Santos, E.; Lundin, A.; Pötting, K.; Quaino, P.; Schmickler, W. Hydrogen Evolution and Oxidation—a Prototype for an Electrocatalytic Reaction. *J. Solid State Electrochem.* **2009**, *13*, 1101−1109.
(357) Santos, E.; Quaino, P.; Schmickler, W. Theory of Electrocatalysis: Hydrogen Evolution and More. *Phys. Chem. Chem. Phys.* **2012**, *14*, 11224−11233.
(358) Wilhelm, F.; Schmickler, W.; Nazmutdinov, R. R.; Spohr, E. Modeling Proton Transfer to Charged Silver Electrodes. *Electrochim. Acta* **2011**, *56*, 10632−10644.
(359) Warshel, A.; Weiss, R. M. An Empirical Valence Bond Approach for Comparing Reactions in Solutions and in Enzymes. *J. Am. Chem. Soc.* **1980**, *102*, 6218−6226.
(360) Schmitt, U. W.; Voth, G. A. The Computer Simulation of Proton Transport in Water. *J. Chem. Phys.* **1999**, *111*, 9361−9381.
(361) Day, T. J. F.; Soudackov, A. V.; Čuma, M.; Schmitt, U. W.; Voth, G. A. A Second Generation Multistate Empirical Valence Bond Model for Proton Transport in Aqueous Systems. *J. Chem. Phys.* **2002**, *117*, 5839−5849.
(362) Kamerlin, S. C. L.; Warshel, A. The Empirical Valence Bond Model: Theory and Applications. *Wiley Interdisciplinary Reviews: Computational Molecular Science* **2011**, *1*, 30−45.
(363) Huang, J.; Chen, S. Interplay between Covalent and Noncovalent Interactions in Electrocatalysis. *J. Phys. Chem. C* **2018**, *122*, 26910−26921.
(364) Huang, J.; Li, P.; Chen, S. Quantitative Understanding of the Sluggish Kinetics of Hydrogen Reactions in Alkaline Media Based on a Microscopic Hamiltonian Model for the Volmer Step. *J. Phys. Chem. C* **2019**, *123*, 17325−17334.
(365) Lam, Y.-C.; Soudackov, A. V.; Goldsmith, Z. K.; Hammes-Schiffer, S. Theory of Proton Discharge on Metal Electrodes: Electronically Adiabatic Model. *J. Phys. Chem. C* **2019**, *123*, 12335−12345.
(366) Fano, U. Effects of Configuration Interaction on Intensities and Phase Shifts. *Phys. Rev.* **1961**, *124*, 1866−1878.
(367) Northrup, S. H.; Hynes, J. T. The Stable States Picture of Chemical Reactions. I. Formulation for Rate Constants and Initial Condition Effects. *J. Chem. Phys.* **1980**, *73*, 2700−2714.
(368) Zusman, L. D. Outer-Sphere Electron Transfer in Polar Solvents. *Chem. Phys.* **1980**, *49*, 295−304.
(369) Sumi, H. Nonradiative Multiphonon Capture of Free Carriers by Deep-Level Defects in Semiconductors: Adiabatic and Nonadiabatic Limits. *Phys. Rev. B* **1983**, *27*, 2374−2386.

https://doi.org/10.1021/acs.chemrev.1c00929
Chem. Rev. XXXX, XXX, XXX−XXX

(370) Hynes, J. T. Outer-Sphere Electron-Transfer Reactions and Frequency-Dependent Friction. *J. Phys. Chem.* **1986**, *90*, 3701−3706.
(371) Rips, I.; Jortner, J. Dynamic Solvent Effects on Outer-Sphere Electron Transfer. *J. Chem. Phys.* **1987**, *87*, 2090−2104.
(372) Straub, J. E.; Berne, B. J. A Statistical Theory for the Effect of Nonadiabatic Transitions on Activated Processes. *J. Chem. Phys.* **1987**, *87*, 6111−6116.
(373) Sparpaglione, M.; Mukamel, S. Dielectric Friction and the Transition from Adiabatic to Nonadiabatic Electron Transfer. 1. Solvation Dynamics in Liouville Space. *J. Chem. Phys.* **1988**, *88*, 3263−3280.
(374) Smith, B. B.; Hynes, J. T. Electronic Friction and Electron Transfer Rates at Metallic Electrodes. *J. Chem. Phys.* **1993**, *99*, 6517−6530.
(375) Makarov, D. E.; Topaler, M. On the Transition from Electronically Nonadiabatic to Solvent-Controlled Electron Transfer. *Chem. Phys. Lett.* **1995**, *245*, 343−350.
(376) Gladkikh, V.; Burshtein, A. I.; Rips, I. Variation of the Resonant Transfer Rate When Passing from Nonadiabatic to Adiabatic Electron Transfer. *J. Phys. Chem. A* **2005**, *109*, 4983−4988.
(377) Saito, K.; Sumi, H. Unified Expression for the Rate Constant of the Bridged Electron Transfer Derived by Renormalization. *J. Chem. Phys.* **2009**, *131*, 134101.
(378) Mishra, A. K.; Waldeck, D. H. Comparison of the Density of States (Dos) and Potential Energy Curve (Pec) Models for the Electrochemical Rate Constant. *J. Phys. Chem. C* **2011**, *115*, 20662−20673.
(379) Landau, L. D. Zur Theorie Der Energieubertragung. *Phys. Z. Sowjetunion* **1932**, *2*, 46−51.
(380) Zener, C. Non-Adiabatic Crossing of Energy Levels. *Proc. R. Soc. London, Ser. A* **1997**, *137*, 696−702.
(381) Grote, R. F.; Hynes, J. T. The Stable States Picture of Chemical Reactions. Ii. Rate Constants for Condensed and Gas Phase Reaction Models. *J. Chem. Phys.* **1980**, *73*, 2715−2732.
(382) Zusman, L. D. Towards a Theory of Electrochemical Processes. *Sov. Electrochem.* **1985**, *21*, 567−571.
(383) Zusman, L. D. Outer-Sphere Electron Transfer Reactions at an Electrode. *Chem. Phys.* **1987**, *112*, 53−59.
(384) Hamelin, A.; Weaver, M. J. Dependence of the Kinetics of Proton Reduction at Gold Electrodes on the Surface Crystallographic Orientation. *J. Electroanal. Chem. Interfacial Electrochem.* **1987**, *223*, 171−184.
(385) Sakaushi, K. Observation of Kinetic Isotope Effect in Electrocatalysis with Fully Deuterated Ultrapure Electrolytes. *J. Electroanal. Chem.* **2019**, *849*, 113372.
(386) Sakaushi, K. Quantum Proton Tunneling in Multi-Electron/-Proton Transfer Electrode Processes. *Faraday Discuss.* **2020**, *221*, 428−448.
(387) Kuznetsov, A. M.; Nazmutdinov, R. R.; Schmickler, W. Monte Carlo Simulation of Electrochemical Electron Transfer Processes. *J. Electroanal. Chem.* **2002**, *532*, 171−180.
(388) Dogonadze, R. R.; Kuznetsov, A. M.; Vorotyntsev, M. A. The Kinetics of the Adiabatic and Nonadiabatic Reactions at the Metal and Semiconductor Electrodes. *Croat. Chem. Acta* **1972**, *44*, 257−273.
(389) Sakata, T.; Hashimoto, K.; Hiramoto, M. New Aspects of Electron Transfer on Semiconductor Surface: Dye-Sensitization System. *J. Phys. Chem.* **1990**, *94*, 3040−3045.
(390) Goodpaster, J. D.; Bell, A. T.; Head-Gordon, M. Identification of Possible Pathways for C-C Bond Formation During Electrochemical Reduction of Co2: New Theoretical Insights from an Improved Electrochemical Model. *J. Phys. Chem. Lett.* **2016**, *7*, 1471−1477.
(391) Sakaushi, K.; Kumeda, T.; Hammes-Schiffer, S.; Melander, M. M.; Sugino, O. Advances and Challenges for Experiment and Theory for Multi-Electron Multi-Proton Transfer at Electrified Solid−Liquid Interfaces. *Phys. Chem. Chem. Phys.* **2020**, *22*, 19401.
(392) Boudart, M. Kinetics on Ideal and Real Surfaces. *AlChE J.* **1956**, *2*, 62−64.
(393) Gokhale, A. A.; Kandoi, S.; Greeley, J. P.; Mavrikakis, M.; Dumesic, J. A. Molecular-Level Descriptions of Surface Chemistry in Kinetic Models Using Density Functional Theory. *Chem. Eng. Sci.* **2004**, *59*, 4679−4691.
(394) Motagamwala, A. H.; Dumesic, J. A. Microkinetic Modeling: A Tool for Rational Catalyst Design. *Chem. Rev.* **2021**, *121*, 1049−1076.
(395) Baz, A.; Dix, S. T.; Holewinski, A.; Linic, S. Microkinetic Modeling in Electrocatalysis: Applications, Limitations, and Recommendations for Reliable Mechanistic Insights. *J. Catal.* **2021**, *404*, 864−872.
(396) Dumesic, J. A. Analyses of Reaction Schemes Using De Donder Relations. *J. Catal.* **1999**, *185*, 496−505.
(397) Campbell, C. T. Future Directions and Industrial Perspectives Micro- and Macro-Kinetics: Their Relationship in Heterogeneous Catalysis. *Top. Catal.* **1994**, *1*, 353−366.
(398) Foley, B. L.; Bhan, A. Degree of Rate Control and De Donder Relations − an Interpretation Based on Transition State Theory. *J. Catal.* **2020**, *384*, 231−251.
(399) Ho, M.-H.; Rousseau, R.; Roberts, J. A. S.; Wiedner, E. S.; Dupuis, M.; DuBois, D. L.; Bullock, R. M.; Raugei, S. Ab Initio-Based Kinetic Modeling for the Design of Molecular Catalysts: The Case of H 2production Electrocatalysts. *ACS Catal.* **2015**, *5*, 5436−5452.
(400) Tang, M. T.; Liu, X.; Ji, Y.; Norskov, J. K.; Chan, K. Modeling Hydrogen Evolution Reaction Kinetics through Explicit Water−Metal Interfaces. *J. Phys. Chem. C* **2020**, *124*, 28083−28092.
(401) Holewinski, A.; Linic, S. Elementary Mechanisms in Electrocatalysis: Revisiting the Orr Tafel Slope. *J. Electrochem. Soc.* **2012**, *159*, H864−H870.
(402) Kelly, S. R.; Kirk, C.; Chan, K.; Nørskov, J. K. Electric Field Effects in Oxygen Reduction Kinetics: Rationalizing Ph Dependence at the Pt(111), Au(111), and Au(100) Electrodes. *J. Phys. Chem. C* **2020**, *124*, 14581−14591.
(403) Rajan, A. G.; Carter, E. A. Microkinetic Model for Ph- and Potential-Dependent Oxygen Evolution During Water Splitting on Fe-Doped B-Niooh. *Energy Environ. Sci.* **2020**, *13*, 4962−4976.
(404) Rajan, A. G.; Martirez, J. M. P.; Carter, E. A. Coupled Effects of Temperature, Pressure, and Ph on Water Oxidation Thermodynamics and Kinetics. *ACS Catal.* **2021**, *11*, 11305−11319.
(405) Rosca, V.; Koper, M. T. M. Mechanism of Electrocatalytic Reduction of Nitric Oxide on Pt(100). *J. Phys. Chem. B* **2005**, *109*, 16750−16759.
(406) Sakaushi, K.; Lyalin, A.; Taketsugu, T.; Uosaki, K. Quantum-to-Classical Transition of Proton Transfer in Potential-Induced Dioxygen Reduction. *Phys. Rev. Lett.* **2018**, *121*, 236001.
(407) Sakaushi, K.; Lyalin, A.; Taketsugu, T. Observations and Theories of Quantum Effects in Proton Transfer Electrode Processes. *Curr. Opin Electrochem* **2020**, *19*, 96−105.
(408) Rebollar, L.; Intikhab, S.; Snyder, J. D.; Tang, M. H. Kinetic Isotope Effects Quantify Ph-Sensitive Water Dynamics at the Pt Electrode Interface. *J. Phys. Chem. Lett.* **2020**, *11*, 2308−2313.
(409) Viswanathan, V.; Hansen, H. A.; Rossmeisl, J.; Jaramillo, T. F.; Pitsch, H.; Nørskov, J. K. Simulating Linear Sweep Voltammetry from First-Principles: Application to Electrochemical Oxidation of Water on Pt(111) and Pt3ni(111). *J. Phys. Chem. C* **2012**, *116*, 4698−4704.
(410) Yeh, K.-Y.; Restaino, N. A.; Esopi, M. R.; Maranas, J. K.; Janik, M. J. The Adsorption of Bisulfate and Sulfate Anions over a Pt(111) Electrode: A First Principle Study of Adsorption Configurations, Vibrational Frequencies and Linear Sweep Voltammogram Simulations. *Catal. Today* **2013**, *202*, 20−35.
(411) McCrum, I. T.; Janik, M. J. Ph and Alkali Cation Effects on the Pt Cyclic Voltammogram Explained Using Density Functional Theory. *J. Phys. Chem. C* **2016**, *120*, 457−471.
(412) Marken, F.; Neudeck, A.; Bond, A. M. In *Electroanalytical Methods: Guide to Experiments and Applications*; Scholz, F., Bond, A. M., Compton, R. G., Fiedler, D. A., Inzelt, G., Kahlert, H., Komorsky-Lovrić, Š., Lohse, H., Lovrić, M., Marken, F. et al., Eds.; Springer: Berlin, Heidelberg, 2010; pp 57−106.
(413) Coffman, A. J.; Dou, W.; Hammes-Schiffer, S.; Subotnik, J. E. Modeling Voltammetry Curves for Proton Coupled Electron Transfer: The Importance of Nuclear Quantum Effects. *J. Chem. Phys.* **2020**, *152*, 234108.

https://doi.org/10.1021/acs.chemrev.1c00929
Chem. Rev. XXXX, XXX, XXX−XXX

(414) Pavošević, F.; Culpitt, T.; Hammes-Schiffer, S. Multicomponent Quantum Chemistry: Integrating Electronic and Nuclear Quantum Effects Via the Nuclear−Electronic Orbital Method. *Chem. Rev.* **2020**, *120*, 4222−4253.
(415) Hammes-Schiffer, S. Nuclear−Electronic Orbital Methods: Foundations and Prospects. *J. Chem. Phys.* **2021**, *155*, 030901.
(416) Habershon, S.; Manolopoulos, D. E.; Markland, T. E.; Miller, T. F. Ring-Polymer Molecular Dynamics: Quantum Effects in Chemical Dynamics from Classical Trajectories in an Extended Phase Space. *Annu. Rev. Phys. Chem.* **2013**, *64*, 387−413.
(417) Greeley, J.; Markovic, N. M. The Road from Animal Electricity to Green Energy: Combining Experiment and Theory in Electrocatalysis. *Energ Environ. Sci.* **2012**, *5*, 9246−9256.
(418) Li, X.; Tully, J. C.; Schlegel, H. B.; Frisch, M. J. Ab Initio Ehrenfest Dynamics. *J. Chem. Phys.* **2005**, *123*, 084106.
(419) Tully, J. C. Molecular Dynamics with Electronic Transitions. *J. Chem. Phys.* **1990**, *93*, 1061−1071.
(420) Kitchin, J. R. Machine Learning in Catalysis. *Nat. Catal* **2018**, *1*, 230−232.
(421) Lamoureux, P. S.; Winther, K. T.; Torres, J. A. G.; Streibel, V.; Zhao, M.; Bajdich, M.; Abild-Pedersen, F.; Bligaard, T. Machine Learning for Computational Heterogeneous Catalysis. *ChemCatChem* **2019**, *11*, 3581−3601.
(422) Keith, J. A.; Vassilev-Galindo, V.; Cheng, B.; Chmiela, S.; Gastegger, M.; Müller, K.-R.; Tkatchenko, A. Combining Machine Learning and Computational Chemistry for Predictive Insights into Chemical Systems. *Chem. Rev.* **2021**, *121*, 9816−9872.
(423) Flores, R. A.; Paolucci, C.; Winther, K. T.; Jain, A.; Torres, J. A. G.; Aykol, M.; Montoya, J.; Nørskov, J. K.; Bajdich, M.; Bligaard, T. Active Learning Accelerated Discovery of Stable Iridium Oxide Polymorphs for the Oxygen Evolution Reaction. *Chem. Mater.* **2020**, *32*, 5854−5863.
(424) Peterson, A. A. Acceleration of Saddle-Point Searches with Machine Learning. *J. Chem. Phys.* **2016**, *145*, 074106.
(425) Torres, J. A. G.; Jennings, P. C.; Hansen, M. H.; Boes, J. R.; Bligaard, T. Low-Scaling Algorithm for Nudged Elastic Band Calculations Using a Surrogate Machine Learning Model. *Phys. Rev. Lett.* **2019**, *122*, 156001.
(426) Secor, M.; Soudackov, A. V.; Hammes-Schiffer, S. Artificial Neural Networks as Mappings between Proton Potentials, Wave Functions, Densities, and Energy Levels. *J. Phys. Chem. Lett.* **2021**, *12*, 2206−2212.
(427) Secor, M.; Soudackov, A. V.; Hammes-Schiffer, S. Artificial Neural Networks as Propagators in Quantum Dynamics. *J. Phys. Chem. Lett.* **2021**, *12*, 10654−10662.

https://doi.org/10.1021/acs.chemrev.1c00929
Chem. Rev. XXXX, XXX, XXX−XXX